Improved Doppler Centroid Estimation Algorithms for Satellite SAR Data

by

SHU LI

B. Eng., Civil Aviation University of China, 2000

M. Sc., Beijing Institute of Technology, 2003

A THESIS SUBMITTED IN PARTIAL FULFILLMENT OF
THE REQUIREMENTS FOR THE DEGREE OF

MASTER OF APPLIED SCIENCE

in

THE FACULTY OF GRADUATE STUDIES

(Electrical and Computer Engineering)

THE UNIVERSITY OF BRITISH COLUMBIA

December 2005

Abstract

In high-quality SAR data processing, accurate estimation of the Doppler centroid frequency is essential for obtaining good image focus. However, existing Doppler centroid estimation algorithms cannot obtain reliable Doppler ambiguity estimates, especially in areas with low SNR and low contrast. This thesis presents several techniques for improving existing Doppler ambiguity estimators, thereby achieving more accurate absolute Doppler centroid estimates for high-quality SAR data processing.

Following an introduction of the existing Doppler centroid estimation algorithms for baseband Doppler centroid and Doppler ambiguity estimation, we present two methods for improving the sensitivity of the Multi-Look Beat frequency (MLBF) Doppler ambiguity estimator. One method uses range cell migration correction (RCMC) to straighten the target trajectories before applying the beat frequency estimator. The other applies more accurate frequency estimators to the beat signal. We then discuss possible improvements to slope-based Doppler ambiguity resolvers. The method using the Radon transform to estimate the slope of target trajectories has been well explained and examined on real satellite SAR data. We propose a simpler method that uses Azimuth integration with RCMC to find the correct ambiguity number. Our experimental results show that it has a similar or better performance than the Radon Transform method.

We have tested all of the improved Doppler ambiguity estimators using real satellite SAR data, RADARSAT-1 Vancouver scene. Our results show that the proposed methods significantly improve the performance of the existing Doppler Ambiguity estimators, and can achieve accurate Doppler centroid estimates in most areas, even with medium to low contrast scenes.

Table of Contents

List of Tables

List of Figures

Acknowledgements

The author would like to thank MacDonald Dettwiler and Associates for providing RADARSAT-1 data and NSERC for research funding.

Many sincere thanks and special appreciation go to my supervisor Prof. Ian Cumming for his guidance, inspiration, and encouragement. Without his help and support, this work would not have been possible. I am also grateful to Dr. Frank Wong for providing further explanation of the Multi-Look concept.

Thanks to the members in UBC Radar Remote Sensing Group, who I was pleasant to work with. Thanks to my lab mates – Millie Sikdar, Kaan Ersahin, Yewlam Neo, Flavio Wasniewski, and Bernd Scheuchl.

At last but not least, I'd like to thank my parents and my husband, Xiushan Feng, for their endless love and support.

SHU LI

The University of British Columbia
December 2005

Chapter 1
Introduction

Synthetic aperture radar (SAR) is a coherent remote sensing system that can provide two-dimensional, high-resolution images of the earth surface. It has advantages over conventional optical imaging systems in that it illuminates the scene with microwave and can thus work under all-weather and all-day conditions. High-quality images of the earth produced by SAR systems are used as important sources of information for a large variety of applications, such as agriculture, ecology, geology, oceanography, hydrology, military, etc. As quality requirements for SAR imaging increase with the growth in applications, more advanced techniques are being explored to improve SAR processing.

1.1 Background

The concept of Synthetic Aperture was first proposed by Carl Wiley of Goodyear Aerospace in 1951, and later provided the theoretical basis of two-dimensional imaging of the earth's surface using radar. SAR systems are carried on a variety of airborne and space-borne platforms and take advantage of the Doppler effect of radar echoes generated by the motion of the platforms.

In a standard implementation, large-bandwidth pulses, typically linear frequency-modulated chirp pulses, are transmitted and processed to obtain a high resolution in the range direction (distance). This technique is known as "pulse compression". In the azimuth direction (along track), the high resolution is achieved by forming a "synthetic aperture" [1]. The synthetic aperture is created by coherently summing the radar echoes along the flight path to artificially synthesize a very long antenna. Theoretically, this long antenna makes fine resolution possible.

Due to the characteristics of the SAR signal, signal processing plays a very important role in achieving high-quality SAR images and has resulted in many advances. There are several SAR signal-processing algorithms that have been successfully implemented to obtain focused images. The main SAR signal-processing algorithms include Range and Doppler (R-D) algorithm [2] [3], Chirp-Scaling (C-S) algorithm [4], SPECAN algorithm [5], and Omega-K algorithm [6]. These algorithms use reconstruction of the two-dimensional signal based on the known system parameters to compress targets in the image.

As SAR systems take advantage of the Doppler effect to achieve high resolution in the azimuth direction, the Doppler centroid is an essential parameter for almost all SAR processing procedures. A Doppler centroid error can lead to defocusing, low signal to noise ratio (SNR), misregistration, and ambiguities in the image. Although several algorithms have been developed for Doppler centroid estimation, a number of satellite SAR systems tend to suffer from Doppler centroid estimation errors in a number of processed scenes. Hence, more reliable Doppler centroid estimation algorithms are required by satellite SAR systems to achieve high- quality imagery.

1.2 State of the Art

I n past years, numerous algorithms for Doppler centroid estimation have been developed through research investment. Since the azimuth data are sampled by the pulse repetition frequency (PRF), the Doppler centroid usually consists of two parts: baseband Doppler frequency and Doppler Ambiguity number. The algorithms for baseband Doppler estimation include the Energy balancing (ΔE) algorithm [7], Average Cross Correlation Coefficient (ACCC) algorithm [8] and "spectral fit" algorithm [9]. The algorithms used to resolve the Doppler ambiguity number include the Look misregistration Algorithm [10], Multiple PRF algorithms [11], Wavelength Diversity Algorithm (WDA) [12], Multi-look Cross Correlation (MLCC) algorithm and Multi-look Beat frequency (MLBF) algorithm [13].

Among the baseband Doppler estimators, the ACCC algorithm and the "spectral fit" algorithm are the two most reliable methods and can obtain good baseband Doppler centroid estimates in most cases. Among the Doppler ambiguity resolvers, the phase-based algorithms, such as the WDA, MLCC and MLBF algorithms, are more accurate than the magnitude-based algorithms, such as the Look misregistration algorithm. However, all the existing Doppler ambiguity resolvers would be easily affected by undesired factors in the real SAR data, such as low SNR, low scene contents, partially exposed strong targets, etc. They cannot provide reliable Doppler ambiguity numbers under such circumstances. Therefore, more accurate and robust Doppler ambiguity estimators are required to meet the quality demands of modern SAR systems.

1.3 Research Scope and Objectives

This thesis focuses on improving existing Doppler ambiguity estimators for satellite SAR systems. Its main purpose is to resolve the Doppler ambiguity number in a more robust and accurate way. RADARSAT-1 fine-mode real data is used to test all proposed algorithms.

The objectives of the research include the following:

- To study the principle of the existing MLBF algorithm in more detail, and investigate the improvements to this algorithm by applying RCMC before the beat frequency estimation.
- To improve the existing MLBF algorithm by using a more accurate frequency estimator in the beat frequency estimation.
- To apply the Radon Transform method to the slope estimation algorithm and examine its performance in the Doppler ambiguity resolution for satellite SAR.
- To investigate a simple yet accurate method to find the correct Doppler ambiguity number by measuring the slope of trajectories.

- To develop specific quality measurements to select best estimators and reject more blocks with bad estimates.
- To compare the performance of the existing and proposed algorithms using RADARSAT-1 real data.

1.4 Thesis Outline

In Chapter 2, the Doppler centroid frequency is introduced from a discussion of the SAR geometry model. The chapter delves further into Doppler centroid variation and the accuracy requirements of Doppler centroid estimation. Chapter 3 presents a critical review of existing Doppler centroid estimation algorithms. Two baseband Doppler centroid estimators and three phase-based Doppler ambiguity resolvers are discussed and their performance evaluated in order to provide an overview of current reliable Doppler centroid estimators.

Since the MLBF algorithm is recognized as one of the most reliable Doppler ambiguity resolvers, we examine the principle of this algorithm in more detail in Chapter 4 and provide a more thorough, frequency-domain explanation of it. We then discuss the benefits of Range Cell Migration Correction (RCMC) and propose the method of iteratively applying RCMC before look extraction. This method can provide a clear beat spectrum and improve the performance of the existing MLBF algorithm. Another method for improving the MLBF algorithm, which uses more accurate frequency estimators on the beat signal, is presented in Chapter 5. It can avoid the FFT limitations of resolution and quantization, especially when the signal is discontinuous in one range cell due to range cell migration or burst mode operation.

In Chapter 6, we discuss the Doppler ambiguity resolvers based on measurement of the slope of target trajectories. We explained the method of using the Radon transform and examined it with satellite data. We then develop an alternate method combining the RCMC and Azimuth integration, and demonstrate it to be a computationally simpler and

more accurate algorithm. Both methods are tested by experiments on RADARSAT-1 real data and show significant improvements over the Doppler ambiguity estimation.

Chapter 7 provides conclusions drawn from the results and comparative analyzes done in the previous chapters. Based on this work, several possible directions for future investigations are also put forth.

Chapter 2

The Doppler Centroid Frequency

In SAR systems, the received signal experiences a Doppler shift because of the relative motion between sensor and targets. The average of this Doppler shift is called the Doppler centroid frequency. The Doppler centroid frequency is a fundamental parameter for reconstructing the signal response in azimuth signal processing and thereby obtaining good image focus.

2.1 Fundamentals of SAR Systems

A SAR system is always carried by a platform (usually a satellite or an aircraft) that moves along orbit or flight track. Figure 2-1 shows a simple geometry model of SAR system [14]. In a SAR system, the antenna points a radar beam approximately perpendicular to the sensor's motion vector, and illuminates microwave signal to interested areas. The footprint of the antenna beam generates a swath on the earth's surface, which is the area to be imaged.

The SAR antenna transmits phase-encoded pulses with a certain frequency, which is called the pulse repetition frequency (PRF), and records the echoes as they reflect off the Earth's surface. The properties of the received signals are determined by the system parameters and the characteristics of the scatters.

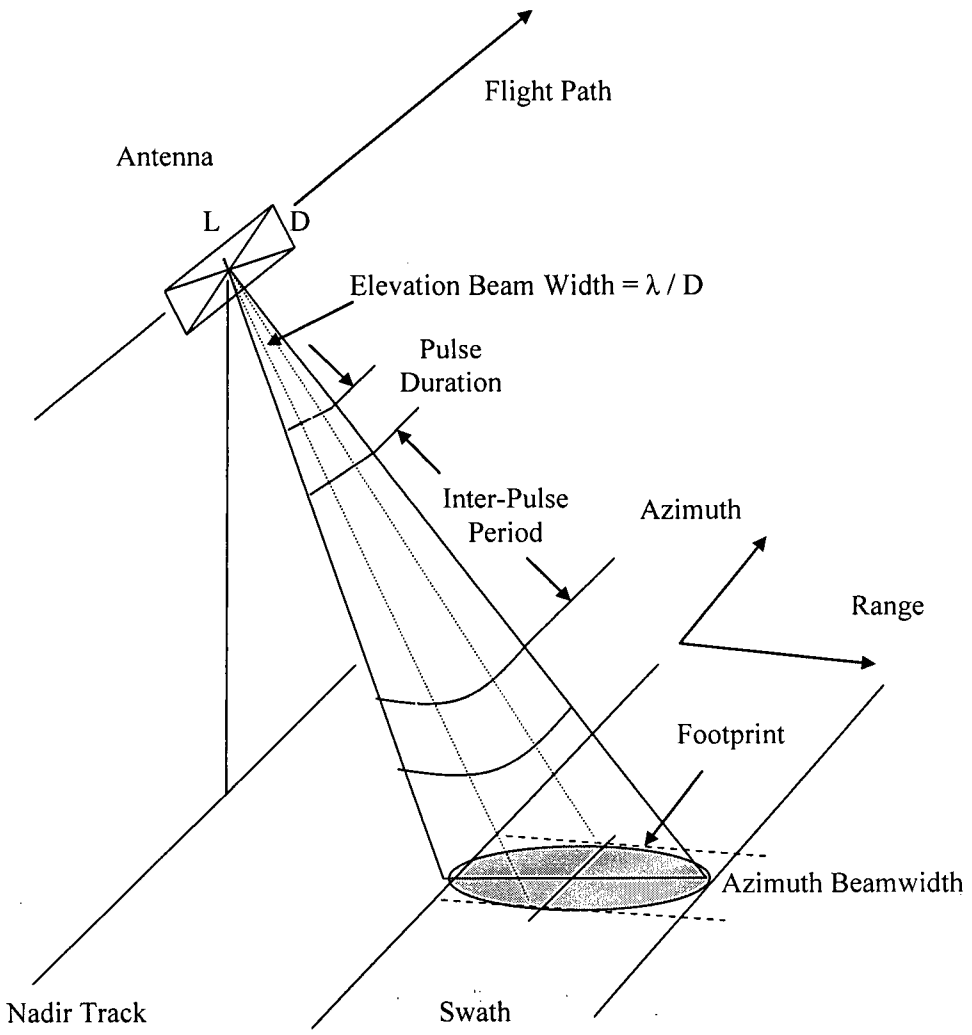

Figure 2-1 Geometry model of SAR system

Then, the received signal is processed in two orthogonal directions in order to generate an SAR image. As denoted in Figure 2-1, one dimension is parallel to the radar beam, which is usually known as the range direction. As in other radar systems, the time delay of received echo in this dimension is proportional to the distance between the antenna and the illuminated target. Therefore, the image in the range direction can be formed by measuring this time delay and placing the echo at the correct distance. In

practice, the beam is not exactly perpendicular to the sensor motion track, and the geometric distortion needs to be corrected.

The other dimension of the image is along the sensor traveling track, which is called the azimuth direction. The image in this direction is formed according to the time of the echoes received and the sensors' current position. The slight variation of the slant range between the sensor and the reflecting target during the sensor traveling generates a different Doppler shift in the azimuth signal. This Doppler shift makes good resolution in the azimuth direction possible. Hence, in azimuth processing the knowledge of the Doppler history is required. Generally, there are two important Doppler parameters for reconstructing the Doppler history: the Doppler centroid and the Doppler FM rate [15].

2.2 The Signal Model for a Point Target

To investigate the principle of SAR imaging, a signal model is established first for a point target. In SAR system, a frequency modulated (FM) signal is transmitted and pulse compression technique is applied in processing. Hence, a high resolution in range direction is obtained.

In most cases, the transmitted signal has a linear FM characteristic and is given by:

$$s_{pul}(\tau) = w_r(\tau) \exp\{ j (2\pi f_0 \tau + \pi K_r \tau^2)\} \qquad (2.1)$$

where K_r is the FM rate of the transmitted pulse, f_0 is the signal transmitting frequency, and τ is referenced to the center of the pulse for convenience.

Consider a point target at a distance, R_a, away from the radar, with a magnitude, A'_0, which models the backscatter coefficient, σ_0. The signal reflected by this target will be received by the antenna after a time delay R_a / c, and can be expressed as:

$$s_r(\tau) = A'_0\, w_r(\tau - 2R_a/c) \exp\left\{ j\,(2\pi f_0 (\tau - 2R_a/c) + \pi K_r (\tau - 2R_a/c)^2 + \varphi) \right\} \tag{2.2}$$

where c is the velocity of the transmitted signal. The scattering process may cause a phase change in the radar signal upon reflection from the surface, which is accounted for by the phase φ in the equation [15].

Expressing the slant range as a function of azimuth time, Equation (2.2) can be rewritten as:

$$s_r(\tau,\eta) = A_0\; w_r(\tau - 2\,R(\eta)/c)\; w_a(\eta - \eta_a) \exp\left\{ j\,(2\pi\; f_0 (\tau - 2\,R(\eta)/c) + \pi\; K_r(\tau - 2\,R(\eta)/c)^2 + \varphi) \right\} \tag{2.3}$$

In (2.3), the range time, τ, is "fast changing time", while azimuth time, η, is "slow changing time". In low squint angle cases, these two times are only slightly coupled and can be processed separately [16]. The separated range and azimuth signal can be expressed as:

Range:

$$s_{range}(\tau) = A_r'\, w_r(\tau - 2\,R_0/c) \exp\left\{ j\,2\pi\; f_0\,\tau + j\pi\; K_r(\tau - 2\,R_0/c)^2 + \varphi) \right\} \tag{2.4}$$

And azimuth:

$$s_{azimuth}(\eta) = A'\, w_a(\eta - \eta_a)\;\; \exp\left\{ - j\,4\pi\; \frac{R(\eta) f_0}{c} \right\} \tag{2.5}$$

2.3 The Doppler Parameters

The Doppler effect within one pulse is quite small and can be negligible. Over many subsequent pulses, the Doppler effect is the main factor that shapes the phase of the received signal in the azimuth direction.

The slant range is a function of azimuth time, and can be expressed as:

$$R(\eta) = \sqrt{R_0^{\,2} + V_r^{\,2}\eta^2} \approx R_0 + \frac{V_r^{\,2}}{2R_0}\eta^2 \tag{2.6}$$

where R_0 is the range when the point target is closest to the antenna, and V_r is the nominal aircraft speed, and also equals the speed of the beam footprint along the surface. Here, the approximate expression is obtained by ignoring the high order components of the Taylor expansion.

Using the approximate slant range equation, the azimuth signal (2.5) can be rewritten as:

$$s_{azimuth}(\eta) = A'\, w_a(\eta - \eta_a) \exp\left\{-j\,4\pi\frac{R_0 f_0}{c}\right\} \exp\left\{-j\,2\pi\frac{V_r^{\,2} f_0}{c R_0}\eta^2\right\} \tag{2.7}$$

The phase of the azimuth signal is therefore given by:

$$\phi(\eta) = -\,4\pi\frac{R_0 f_0}{c} - 2\pi\frac{V_r^{\,2} f_0}{c R_0}\eta^2 \tag{2.8}$$

Thus, the Doppler history can be expressed as:

$$f_a(\eta) = \frac{1}{2\pi}\frac{d\phi(\eta)}{d\eta} = -\,\frac{2V_r^{\,2} f_0}{c R_0}\eta \tag{2.9}$$

Equation (2.9) shows that the azimuth signal of SAR is also a chirp signal. This chirp signal has two important parameters. One is its FM rate, which is called the Doppler rate. The Doppler rate can be derived from (2.9) as:

$$K_a = \frac{d f_a(\eta)}{d\eta} = -\frac{2V_r^{\,2} f_0}{c R_0} \tag{2.10}$$

The other important parameter is the Doppler centroid, which is defined as the Doppler frequency received from a given point target on the ground when the target is centered in the azimuth antenna beam pattern. It represents the central azimuth frequency, and can be expressed as:

$$f_{\eta c} = f_a(\eta_c) = -\frac{2V_r^{\,2} f_0}{c R_0}\eta_c \tag{2.11}$$

where η_c is the beam center crossing time relative to the time of closest approach.

2.4 Doppler Centroid Estimation

As the Doppler centroid is an essential parameter in azimuth processing, accurate Doppler centroid frequency is required for most SAR processing. Doppler centroid errors may affect registration and focusing, and raise the noise and ambiguity levels in the processed image, sometimes to the point of seriously affecting image quality [15] [17].

2.4.1 Overview

In ideal circumstances, the Doppler centroid can be calculated from geometry model with the knowledge of system parameters. But in practice the satellite system does not have sufficiently accurate attitude measurements or beam pointing knowledge to calculate the centroid from geometry alone [18] [19].

To achieve relative accurate results, the Doppler centroid is usually estimated from the received data. Because the azimuth signal is observed in a sampled fashion, it is useful to consider the Doppler frequency as having two components. The sampling rate is the PRF, which limited the highest observable Doppler frequency between - ½ PRF to + ½ PRF. Frequencies outside this range are wrapped around, but still are important for SAR processing. Therefore, the Doppler centroid frequency is normally considered as having two components: the baseband Doppler centroid and the Doppler ambiguity number [19]. Then, the absolute Doppler centroid can be expressed as [15] [19]:

$$f_{\eta c} = f'_{\eta c} + M_{amb}\, PRF \tag{2.12}$$

where $f'_{\eta c}$ is the fractional PRF part, and M_{amb} is the ambiguity number.

Despite many advances in SAR processing, a number of satellite SAR systems still tend to suffer from unreliable Doppler centroid estimates in some kinds of scenes. Since the Doppler estimation result has a considerable dependence on the scene content, it is difficult to estimate the Doppler centroid accurately [19].

2.4.2 Variations of the Doppler centroid

This section explains the original of the Doppler centroid variation with range and azimuth, and how it is affected by antenna's yaw and pitch. As the Doppler centroid is a function of slant range, it varies along the range cells. In the same azimuth cell, the Doppler centroid in near range cells is larger than that in far range cells. In satellite SAR systems, the relative range between the satellite and intersected earth surface is changing along the satellite orbit [15]. These changes make the Doppler centroid vary in azimuth time.

In addition, the satellite attitude also changes from time to time, which makes the beam pointing direction biased. Figure 2-2 shows the definitions of the three basic attitude angles of a platform. Yaw angle is defined as the angle between the platform's longitudinal axis and its line of travel, and pitch angle is defined as the angle between the direction of magnetic field and a platform's spiral trajectory [20]. Yaw and pitch angles would make the antenna beam bias a bit and thus affect the value of the Doppler centroid [15] [19]. In other words, the changes in yaw and pitch angles also makes the Doppler centroid vary in azimuth time. In the satellite SAR systems that use yaw-steered antenna, such as ERS-1 and EnviSAT, the variation is typically reduced to within one PRF. However, in the satellite SAR system without yaw-steered antenna, such as RADARSAT-1, the variation may be over a significant extent in frequency.

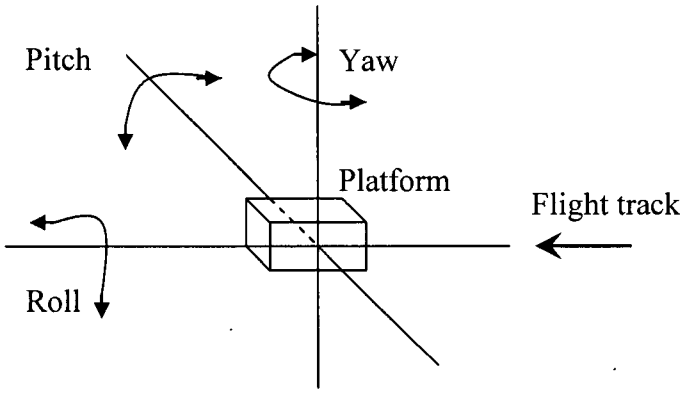

Figure 2-2 Attitude angles of the platform

In practice, the Doppler centroid should be estimated for different range blocks and updated in successive azimuth blocks due to its variation in range and azimuth. Usually, a two-dimensional global model (polynomial model or geometry model) is applied to provide a reliable overall estimate (See Section 3.3.3).

2.4.3 Doppler centroid accuracy requirements

Some functions in the signal processing chain (e.g., basic azimuth compression) require that only the baseband Doppler centroid be known. Other functions (e.g., RCMC and Second Range Compression) require that the whole absolute Doppler centroid be known.

As the baseband Doppler Centroid is usually used to generate the matched filter for azimuth compression, it is very important for image quality. If the baseband Doppler centroid estimate has error, the center frequency of the azimuth matched filter moves away from the peak of the signal spectral energy. As a result, the signal to ambiguity ratio and the signal to noise ratio are reduced.

So, the accuracy requirements for baseband Doppler centroid estimation can be specified by placing a limit on the allowed drop in either signal-to-ambiguity ratio or

SNR. A typical specification quoted for the Doppler centroid is that it should be accurate to ±5% of the PRF for regular beam processing. In this case, with an oversampling of 1.3, the signal-to-ambiguity ratio is lowered by 1.4 dB, and the SNR degradation is less than 0.1 dB [15].

The Doppler ambiguity is expressed as an integer number and is the main part of the obsolete Doppler centroid. If the ambiguity number has error, it would lead to the error of the obsolete Doppler centroid as large as an integer times of the PRF. This error causes a focusing error in both range and azimuth, and a registration error in azimuth. Because the ambiguity number has a large effect on azimuth registration, it is generally accepted that there should be no error in this parameter [15].

2.5 Summary

Because of the Doppler effect, the SAR azimuth signal is also a chirp. This chirp signal can be reconstructed by two Doppler parameters: the Doppler rate and the Doppler centroid frequency. So, the Doppler centroid frequency becomes an essential parameter for accurate SAR processing, especially for azimuth processing. The Doppler centroid errors raise the noise and ambiguity levels in the processed image, and sometimes even blur the image.

Although the Doppler centroid can be derived from a SAR geometry model, this calculation is usually not accurate enough due to the inaccurate satellite attitude measurements. The Doppler centroid estimation from the received data is required in most high quality SAR systems. The following sections will discuss a number of different algorithms used to estimate both the baseband Doppler and the Doppler ambiguity number.

Chapter 3
Existing Doppler Centroid Estimation Algorithms

As described in Chapter 2, the Doppler centroid can be obtained geometrically from attitude measurements. But as these measurements are usually not accurate enough, a number of estimation algorithms based on received data are available to obtain reliable Doppler centroid. In this chapter, we introduce several existing Doppler centroid estimation algorithms that have relatively good performances. The "spectral fit" algorithm and the Average Cross Correlation Coefficients (ACCC) algorithm are introduced for the baseband Doppler centroid estimation. For the Doppler ambiguity resolution, three phase-based algorithms are the widely used. They are the Wavelength Diversity Algorithm (WDA) algorithm, the Multi-Look Cross Correlation (MLCC) algorithm, and the Multi-Look Beat Frequency (MLBF) algorithm.

3.1 Baseband Doppler Centroid Estimation

The baseband Doppler centroid corresponds to the fractional PRF part of the absolute Doppler centroid value. It can be considered as the wraparound result as the azimuth signal is sampled by the PRF. Since it is the "visible" part of the Doppler centroid in the azimuth spectrum, the baseband Doppler frequency is easier to estimate than the "invisible" part, the Doppler ambiguity number.

3.1.1 The "spectral fit" algorithm

The "spectral fit" algorithm is a magnitude based estimation approach. Similar to the energy balancing method, this algorithm takes advantage of the Doppler power spectrum. In order to find the centre of the spectrum accurately, a certain model is established and used to fit the shape of the power spectrum of the azimuth signal. Then the estimate of the baseband Doppler centroid can be obtained directly from the parameters of the fit model.

It is shown in [15] [19] that due to the effect of antenna pattern, ground reflectivity and system transfer function, the noisy power spectrum can be modeled as a sine wave on a pedestal. Hence, in this algorithm the sine wave model is chosen to fit the azimuth power spectrum. The spectral center can be obtained from the phase angle of the fitting sine wave. In implementation, this phase angle can be derived from the first harmonic component of the spectrum, which corresponds to the second FFT coefficient of the power spectrum.

The Doppler centroid can be obtained from the estimated phase angle of the fit sine wave by:

$$f_{\eta c} = \frac{PRF}{2\pi}\Phi_{\sin} \tag{3.1}$$

where $\Phi_{\sin}$ is the phase angle of the fitting sine wave.

In the phase angle calculation, the angle, $\Phi_{\sin}$, is wrapped around within the range of $(-\pi, \pi]$. Correspondingly, the Doppler estimate obtained from (3.1) only contains the baseband component of the Doppler centroid lying in the frequency range of $(-PRF/2, PRF/2)$. So, the "spectral fit" algorithm is only suitable to the baseband Doppler estimation.

3.1.2 The ACCC algorithm

Another baseband Doppler centroid estimation algorithm based on phase information was proposed by Madsen in 1989 [8]. In this method, the phase of the received signal is used to estimate the baseband Doppler centroid. Since the phase increment calculation can be instituted by correlation calculation, this method is also called as the Average Cross Correlation Coefficient (ACCC) algorithm.

The principle of the ACCC algorithm can best be understood by deriving the SAR signal of a single point target after range compression. Ignoring the scattering magnitude and the range envelope, the azimuth signal can be represented by:

$$s_{azimuth}(\eta) = w_a(\eta - \eta_c)\exp\left\{-j\frac{4\pi f_0 R(\eta)}{c}\right\} \tag{3.2}$$

where $R(\eta)$ is the slant range function, c is the velocity of the transmitted signal, f_0 is the center frequency of the transmitted signal, η_c is the time when the target is illustrated by the beam centre, and $w_a(\eta)$ is the antenna pattern function.

To examine the time dependency of the beat signal in detail, we expand the slant range function, $R(\eta)$. To make the calculation simpler, the higher order components are ignored. Then, the slant range can be approximated by:

$$R(\eta) = \sqrt{R_0^{\,2} + V_r^{\,2}\eta^2} \approx R_0 + \frac{1}{2}\frac{V_r^{\,2}}{R_0}\eta^2 \tag{3.3}$$

Using (3.3), we can rewrite the signal of (3.2) as:

$$\begin{aligned} s(\eta) &= w_a(\eta - \eta_c)\exp\left\{-j4\pi\left(\frac{f_0 R_0}{c} + \frac{f_0 V_r^{\,2}}{2R_0 c}\eta^2\right)\right\} \\ &= A\,w_a(\eta - \eta_c)\exp\left\{-j\pi K_{a.dop}\,\eta^2\right\} \end{aligned} \tag{3.4}$$

where A is a constant equal to $\exp\left\{-j\frac{4\pi f_0 R_0}{c}\right\}$, and $K_{a,dop} = \frac{2V_r^{\,2}}{cR_0} f_0$ is the azimuth Doppler FM rate of the signal.

The Average Cross Correlation Coefficient (ACCC) is defined as the average of the correlation between two successive azimuth samples. By summing over azimuth time, the ACCC of the azimuth signal is given by [15]:

$$\begin{aligned}\overline{C(\eta)} &= \sum_{\eta} s^{*}(\eta)s(\eta+\Delta\eta) \\ &= \sum_{\eta} |A|^2 w_a(\eta-\eta_c)w_a^{*}(\eta-\eta_c+\Delta\eta) \\ &\quad \exp\{j\pi K_{a,dop}\eta^2\}\exp\{-j\pi K_{a,dop}(\eta+\Delta\eta)^2\} \\ &\approx \sum_{\eta} |A|^2 \left|w_a(\eta-\eta_c)\right|^2 \exp\{-j\,2\pi\,K_{a,dop}\eta\,\Delta\eta\}\end{aligned} \tag{3.5}$$

where $\Delta\eta = 1/PRF$ is the time increment between two successive azimuth samples.

Then, the ACCC angle can be expressed as:

$$\Phi_{ACCC} = \arg\left[\overline{C(\eta)}\right] = \tan^{-1}\left[\frac{\sum_{\eta}\sin(-2\pi\,K_{a,dop}\,\eta\,\Delta\eta)}{\sum_{\eta}\cos(-2\pi\,K_{a,dop}\,\eta\,\Delta\eta)}\right] \tag{3.6}$$

Because η is centered at η_c and the calculation is symmetric, (3.6) can be simplified as:

$$\begin{aligned}\Phi_{ACCC} &= \arg\left[\overline{C(\eta)}\right] = \tan^{-1}\left[\frac{\sin(2\pi\,K_{a,dop}\,\eta_c\,\Delta\eta)}{\cos(2\pi\,K_{a,dop}\,\eta_c\,\Delta\eta)}\right] \\ &= 2\pi\,K_{a,dop}\,\eta_c\,\Delta\eta = -\frac{2\pi}{PRF}K_{a,dop}\,\eta_c\end{aligned} \tag{3.7}$$

According to the relationship between the Doppler centroid and the central time, η_c, the estimate of the Doppler Centroid can be expressed as:

$$f_{\eta c} = -K_{a,dop}\,\eta_c = \frac{PRF}{2\pi}\Phi_{ACCC} \tag{3.8}$$

Like in the "spectral fit" algorithm, the angle Φ_{ACCC} is wrapped around within the range of $(-\pi, \pi]$. So, the ACCC algorithm also can only be used to estimate the *baseband* Doppler centroid.

3.2 The Phase Based Doppler Ambiguity Resolvers

As the baseband Doppler centroid is wrapped around by the PRF, the integer PRF part, which is known as the Doppler Ambiguity number, is needed to complete the absolute Doppler centroid frequency. There are a number of techniques developed for the Doppler ambiguity resolution.

In this section, we only discuss three Doppler ambiguity resolvers (DAR) that are based upon the phase information of the azimuth signal. The basic principle of phase-based DAR is that the absolute Doppler centroid is a linear function of the radar carrier frequency, f_0 [12]. This linear coefficient is generally not wrapped, as the pulse bandwidth is very small compared to the carrier frequency [15]. So, the absolute Doppler centroid can be obtained and the Doppler ambiguity number can be resolved.

3.2.1 The WDA algorithm

The German Aerospace Establishment (DLR) developed the Wavelength Diversity algorithm (WDA) to resolve the Doppler ambiguity in 1991 [12]. This algorithm takes advantage of the fact that the Doppler properties of the received signal can be considered as a function of range wavelength.

In the WDA, the range compressed data is transformed into the range frequency domain by a range FFT, and the ACCC angle is calculated for each range frequency cell. The slope of the ACCC angle versus range frequency is measured by using a linear fit. Then the absolute Doppler centroid can be derived from the measured slope.

Like in the ACCC algorithm, the ACCC angle (3.7) can be calculated as:

$$\Phi_{ACCC} = -\frac{2\pi}{PRF} K_{a,dop}\, \eta_c = -\frac{2\pi}{PRF} \frac{2V_r^2 f_0}{c R_0} \eta_c \qquad (3.9)$$

where f_0 is the nominal or average radar frequency. For a chirped radar, f_0 should be replaced by the instantaneous range frequency, $f_0 + f_\tau$, where f_τ is the baseband pulse frequency. Substituting the instantaneous range frequency for f_0 in (3.9), the range frequency dependence of the ACCC angle is given by:

$$\Phi_{ACCC}(f_\tau) = -\frac{2\pi}{PRF}\frac{2V_r^2(f_0+f_\tau)}{c\,R_0}\eta_c \tag{3.10}$$

and the slope of Φ_{ACCC} versus f_τ can be thereby expressed as:

$$k = \frac{d\,\Phi_{ACCC}(f_\tau)}{df_\tau} = -\frac{2\pi}{PRF}\frac{2V_r^2}{c\,R_0}\eta_c \tag{3.11}$$

From the relationship between the Doppler Centroid and the central time, we have:

$$f_{\eta c} = -K_{a,dop}\eta_c = -\frac{2V_r^2 f_0}{c\,R_0}\eta_c \tag{3.12}$$

Comparing (3.11) and (3.12), the Doppler Centroid can be estimated using the measured slope, k, as:

$$f_{\eta c} = \frac{PRF}{2\pi} f_0\, k \tag{3.13}$$

Since the value of k is usually very small, it avoids the wraparound and then can provide the estimate of the absolute Doppler centroid frequency.

3.2.2 The MLCC algorithm

The Multi-Look Correlation Coefficient (MLCC) algorithm [13] [15] takes advantage of the frequency difference between two range looks to measure the slope k in the WDA algorithm. The two range looks can be generated by separating the range compressed image from the range spectrum. These two range looks are used to emulate

two SAR systems imaging the same area, but working at different center frequencies. The two center frequencies have slight difference and are given by:

$$f_1 = f_0 - \frac{\Delta f_r}{2}, \quad \text{and} \quad f_2 = f_0 + \frac{\Delta f_r}{2}, \tag{3.14}$$

where Δf_r is the look separation in the range frequency domain.

To illustrate this algorithm clearly, we also check the point target model of (2.5) in Chapter 2. The two looks signal of the range-compressed image can be expressed as follows,

Look 1:

$$s_1(\eta) = w_a(\eta - \eta_c)\exp\left\{-j\frac{4\pi}{c} f_1 \; R(\eta)\right\} \tag{3.15}$$

And Look 2:

$$s_2(\eta) = w_a(\eta - \eta_c)\exp\left\{-j\frac{4\pi}{c} f_2 \; R(\eta)\right\} \tag{3.16}$$

The phase arguments in (3.15) and (3.16) give the azimuth phase history of the target, which are different between the two looks because of the frequency difference, Δf_r. Therefore, the equations (3.15) and (3.16) can be approximated by a simpler form as in equation (3.12), which can be expressed as follows,

Look 1:

$$s_1(\eta) = w_a(\eta - \eta_c)\exp\left\{-j\pi \; K_{a1,dop} \; \eta^2\right\} \tag{3.17}$$

And Look 2:

$$s_2(\eta) = w_a(\eta - \eta_c)\exp\left\{-j\pi \; K_{a2,dop} \; \eta^2\right\} \tag{3.18}$$

where $K_{a1,dop}$ and $K_{a2,dop}$ are the azimuth Doppler FM rate of the two looks.

The azimuth Doppler FM rate of the two looks are given by

Look 1:

$$K_{a1,dop} = \frac{2f_1}{c} \; \frac{d^2R(\eta)}{d\eta^2} = \frac{2V_r^{\,2}}{cR_0} f_1 \tag{3.19}$$

And Look 2:

$$K_{a2,dop} = \frac{2f_2}{c} \frac{d^2R(\eta)}{d\eta^2} = \frac{2V_r^2}{cR_0} f_2 \tag{3.20}$$

Applying the same concept in the WDA algorithm, the difference between the ACCC angles of the two range looks, divided by the frequency difference, Δf_r, gives the estimate of the same slope as in the WDA algorithm. Therefore, in the MLCC algorithm, we calculate the ACCC angles of the two looks separately.

The ACCC function of Look 1 can be expressed as:

$$\overline{C_1(\eta)} = \sum_{\eta} s_1(\eta) s_1^*(\eta + \Delta\eta) \tag{3.21}$$

And the ACCC angle is given by:

$$\Phi_{L1} = \arg\left[\overline{C_1(\eta)}\right] = \frac{2\pi}{PRF} K_{a1,dop}\, \eta_c \tag{3.22}$$

Similarly, the ACCC angle for Look2 can be calculated as:

$$\overline{C_2(\eta)} = \sum_{\eta} s_2(\eta) s_2^*(\eta + \Delta\eta) \tag{3.23}$$

$$\Phi_{L2} = \arg\left[\overline{C_2(\eta)}\right] = \frac{2\pi}{PRF} K_{a2,dop}\, \eta_c \tag{3.24}$$

Then, the difference between the ACCC angles of the two range looks is given by:

$$\Delta\Phi = \Phi_{L2} - \Phi_{L1} = \frac{2\pi}{PRF}\left(K_{a2,dop} - K_{a1,dop}\right)\eta_c \tag{3.25}$$

From (3.19) and (3.20), the difference between the Doppler FM rates of the two looks can be expressed as:

$$\begin{aligned} \Delta K_{a,dop} &= K_{a2,dop} - K_{a1,dop} = \frac{2V_r^2}{cR_0}(f_2 - f_1) \\ &= \frac{2V_r^2}{cR_0}\Delta f_r = K_{a,dop}\frac{\Delta f_r}{f_0} \end{aligned} \tag{3.26}$$

Using (3.26), (3.25) can be rewritten as:

$$\Delta\Phi = -\frac{2\pi}{PRF}\frac{\Delta f_r}{f_0} K_{a,dop}\ \eta_c = \frac{2\pi}{PRF}\frac{\Delta f_r}{f_0} f_{\eta c} \tag{3.27}$$

So, the absolute Doppler Centroid frequency is given by:

$$f_{\eta c} = \frac{PRF}{2\pi}\frac{f_0}{\Delta f_r}\Delta\Phi \tag{3.28}$$

As $\Delta\Phi$ is usually small enough to avoid wraparound, the MLCC algorithm can provide the estimate of the absolute Doppler centroid frequency, and thereby resolve the Doppler ambiguity number.

3.2.3 The MLBF algorithm

The other multilook Doppler ambiguity resolver is called Multilook Beat Frequency (MLBF) algorithm [13] [15]. Like in the MLCC algorithm, two range looks are first generated by separating the range compressed image in range spectrum. After that, a beat signal is obtained by multiplying one range look with the conjugate of the other look. The beat signal contains information concerning the phase difference between the two range looks. Its average frequency is called the "beat frequency". The beat frequency is proportional to the absolute Doppler centroid frequency, and is small enough to avoid the wraparound problem.

From the equations of two range looks, (3.17) and (3.18), the beat signal $s_b(\eta)$ for a point target can be expressed as [13]:

$$\begin{aligned} s_b(\eta) &= s_1(\eta)\, s_2^{*}(\eta) \\ &= \left|w_a(\eta-\eta_c)\right|^2 \exp\left\{-j\pi(K_{a2,dop} - K_{a1,dop})\,\eta^2\right\} \end{aligned} \tag{3.29}$$

And the central frequency can be calculated from the phase component as:

$$f_{beat} = \frac{1}{2}\frac{d\left[(K_{a2,dop} - K_{a1,dop})\,\eta^2\right]}{d\eta}\bigg|_{\eta=\eta_c}$$
$$= -(K_{a2,dop} - K_{a1,dop})\,\eta_c = \quad K_{a,dop}\frac{\Delta f_r}{f_0}\eta_c = \quad -\frac{\Delta f_r}{f_0} f_{\eta c} \tag{3.31}$$

The central frequency of the beat signal is called the beat frequency, which can be estimated by using a FFT operation. The estimate of the beat frequency, $\hat{f}_{beat}$, can be obtained by finding the frequency, at which the beat spectrum has its maximum value. A FFT operation is usually used in the beat frequency estimation.

Then the absolute Doppler frequency is estimated by:

$$\hat{f}_{\eta c} = \quad -\frac{f_0}{\Delta f_r}\hat{f}_{beat} \tag{3.32}$$

In this algorithm, $\hat{f}_{beat}$ is usually small enough to avoid the wraparound. Therefore, the MLBF algorithm could be used to resolve the Doppler ambiguity number.

3.2.4 Resolving the ambiguity number

The Doppler estimators discussed above can provide the estimates of the absolute Doppler centroid. However, these estimates are usually not accurate enough in the baseband part due the presence of noise. Since there are quite a few algorithms that have reliable performances in baseband Doppler estimation, the algorithms discussed in this section are only used to provide the estimate of the Doppler ambiguity number.

To resolve the Doppler ambiguity number, first the baseband Doppler centroid is measured by the "spectral fit" or ACCC algorithm, which are discussed in Section 3.1. After that, in order to obtain the estimate of an integer, the baseband Doppler centroid is subtracted from the estimated absolute Doppler frequency and the result is divided by the PRF. Then the ambiguity estimate is obtained by a rounding operation. The whole calculation can be expressed as [15] [19]:

$$M_{amb} = round\left(\frac{f_{\eta c} - f_{\eta c}'}{PRF}\right) \tag{3.33}$$

where $f_{\eta c}$ is the absolute Doppler frequency, and $f_{\eta c}'$ is the baseband Doppler centroid.

3.3 Discussion

The "spectral fit" algorithm and the ACCC algorithm work quite well in most cases, but they can be biased by partially exposed targets and low values of SNR. However, the estimate errors can be successfully fixed using the "global fit process", which will be introduced in Section 3.3.3.

Compared to the baseband Doppler estimation, the Doppler ambiguity estimation is more challenging, since one number error will lead to one PRF estimate error. The three phase-based Doppler ambiguity resolvers are derived from the same principle, and share some common calculation steps, such as ACCC calculation, look extraction, etc. For all algorithms, averaging over several range cells is usually required in the implementation in order to improve the performance.

3.3.1 The offset frequency

It is worth noting that in SAR satellite systems, the azimuth boresight angle of the radar beam can vary as the chirp sweeps through its frequencies [15]. This means that η_c in (3.17) and (3.18), may have a small dependence on the radar transmission frequency, $f_0 + f_\tau$. This leads to a shift in the azimuth envelope, $w_a(\eta - \eta_c)$. This shift in envelope gives rise to an offset frequency, which is not negligible in the WDA and MLCC algorithms. Figure 3-1 shows the relationship of the offset frequency and the Doppler frequency slope [15]. As a result, in the WDA and MLCC algorithms, the estimate of the offset frequency is inevitable, and the unbiased Doppler centroid estimate is given by:

$$\hat{f}_{\eta c} = \hat{f}_{\eta c}^{(*)} + f_{os} \tag{3.34}$$

where $\hat{f}_{\eta c}$ is the unbiased Doppler centroid estimate, $\hat{f}_{\eta c}^{(*)}$ is the Doppler centroid estimate biased by the offset frequency, and f_{os} is the offset frequency.

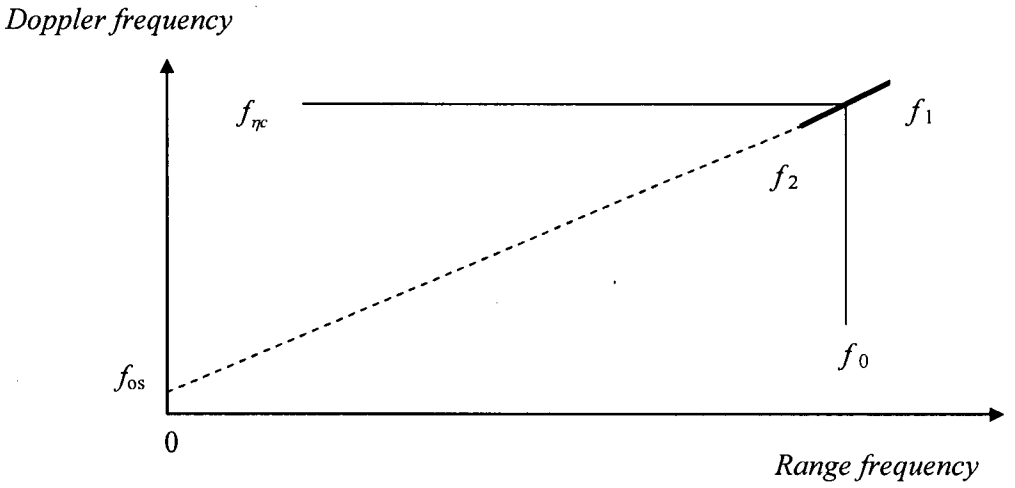

Figure 3-1 An offset frequency in the WDA and MLCC algorithms

The compensation for this offset frequency is important in the estimation. Unfortunately, it appears to be difficult to obtain a consistent value of f_{os} for the current satellite radar systems [15]. Unlike the MLCC algorithm, the MLBF algorithm does not suffer from the offset frequency, as described in Appendix 12B of [15]. Therefore, when the MLCC and MLBF algorithms are used together, the difference in their estimates can be used to find the offset frequency.

3.3.2 The effect of scene content

In Section 3.2, we only use the example of single isolated target to illustrate the principle of the three phase-based Doppler ambiguity resolvers. In practice, the content of the scene has considerable effect on the estimate results. A scene can have a few isolated bright targets, which is referred to a high contrast scene, or can have fairly uniform radiometry, which is referred to a low contrast scene. Because the MLBF algorithm uses

the measurement of the beat frequency to estimate the Doppler centroid, which is different to the WDA and MLCC algorithms, the scene contrast shows different effects on the estimate results of the three estimators [21].

As described in Section 3.2, the measurements of ACCC angles are used in the WDA and MLCC algorithms. Since the ACCC angles are quite different between the beginning part and the end part of a target, the WDA and MLCC algorithms suffer from partially exposed bright targets. Therefore, these two algorithms have good performance in low contrast scenes, which have fairly uniform radiometry [15].

On the other hand, the MLBF algorithm benefits from the presence of bright discrete targets. As shown in the analysis of the point target from (3.28) to (3.30), the MLBF algorithm works best when there is only a single dominant target. When multiple targets are present in the same range cell, cross beating between the targets will destroy the purity of the beat frequency and lower the SNR of the beat signal. This will be described in more detail in Section 4.3.1. In addition, the partially exposed targets have little effect on the beat frequency measurement, and thus the MLBF algorithm can work well with the scenes of partial exposures [16]. So, the MLBF algorithm has a good performance in the scenes with bright isolated targets, in which the MLCC algorithm might fail.

3.3.3 The global estimation procedure

As the Doppler centroid estimates are always affected by the undesired properties of the received data, such as low SNR, strong partial exposure, and radiometric discontinuities. A global estimation procedure is required to provide reliable overall estimates.

To obtain a reliable overall estimate, the concept of "spatial diversity" in Doppler centroid estimation was proposed in 2004 [19]. It refers to the use of data from representative parts of the radar scene in the estimation process. In this approach, the

whole scene is divided up into several blocks, the Doppler centroid estimators are applied to each block separately. The global Doppler centroid estimation procedure only includes the blocks which provide good Doppler estimates, and excludes other blocks that provide the noisy or biased estimates.

To recognize the blocks with good estimates from the other "bad" blocks, estimator quality criteria measures are introduced. Commonly-used quality criteria measures include SNR, spectral distortion, azimuth gradient, and contrast [15] [19]. After rejecting the "bad" blocks by applying these quality criteria measures, the remaining good estimates are used to fit a global model. A simple global model is the polynomial model [22] [23], which assumes the Doppler centroid can be approximated by a polynomial function of range and azimuth time. A more complicated model is the geometry model, which uses the satellite's state vectors, the Earth's movement, the antenna attitude, and some other system parameters to derive the Doppler centroid. Then, the Doppler centroid in the rejected blocks can be calculated from fitting model based on the good estimates. In the end, the global Doppler centroid estimates are obtained and improved.

3.4 Summary

The absolute Doppler centroid frequency is composed by the baseband Doppler centroid and the Doppler ambiguity number. The "spectral fit" and ACCC algorithms can provide reliable baseband Doppler estimates in most cases. The phase-based Doppler ambiguity resolvers prove to have generally good performances in resolving the Doppler ambiguity number of the satellite SAR systems. Because the MLCC algorithm works well in low contrast scene while the MLBF algorithm works well in high contrast scene, the two algorithms can be combined with each other to improve the performance. Finally, the reliable global good estimate can be achieved by applying the "spatially selective approach".

Chapter 4

RCMC in the MLBF algorithm

The slant range, $R(\eta)$, is expressed as a hyperbolic function of azimuth time, η. This function shows that the target trajectory migrates through range cells during the target exposure time, which is called "range cell migration" (RCM) [15]. The existence of the RCM complicates the processing, and also has some noticeable effects on the beat spectrum in the MLBF algorithm. In this chapter, we will consider applying RCM Correction (RCMC) in the MLBF algorithm for improvements.

4.1 Theoretical Background

In Chapter 3, we take it for granted that the two range looks can simulate two radars that work at different central frequencies and then the Doppler centroid can be estimated from the differences in azimuth phase history between two range looks. In this section, the theory of the MLBF algorithm is explained in more detail. In order to explain it in a simple way, we use the signal model for a single point target for illustration.

4.1.1 Range compressed signal

Assuming a unit scattering magnitude, the received signal after demodulation in the range frequency domain can be expressed as [15]:

$$S_0(f_\tau,\eta) = W_r(f_\tau)\ w_a(\eta-\eta_c) \exp\left\{-j\frac{4\pi(f_0+f_\tau)R(\eta)}{c}\right\} \exp\left\{-j\frac{\pi f_\tau^2}{K_r}\right\} \tag{4.1}$$

where f_0 is the radar transmitting centre frequency, $R(\eta)$ is the slant range function, c is the velocity of the transmitted signal, $W_r(f_\tau)$ is the envelope of the range frequency spectrum, and $w_a(\eta-\eta_c)$ is the azimuth envelope with respect to the beam centre crossing time, η_c. It is worth noting that even though the signal has been demodulated to baseband, the signal retains a phase term due to $(f_0 + f_\tau)$, the actual transmitted frequency.

After multiplying the range matched filter, $G(f_\tau)$, the range compressed signal in the range frequency domain is given by:

$$\begin{aligned} S_{RC}(f_\tau,\eta) &= S_0(f_\tau,\eta)\cdot G(f_\tau) \\ &= W_r'(f_\tau)\, w_a(\eta-\eta_c)\, \exp\left\{-j\frac{4\pi(f_0+f_\tau)R(\eta)}{c}\right\} \end{aligned} \tag{4.2}$$

where $W_r'(f_\tau)$ is the envelope of the range frequency spectrum multiplied by the weighting function used in the range matched filter.

As shown in (4.2), the phase of range-compressed signal constitutes of a constant term $-4\pi f_0 R(\eta)/c$ and a term $-4\pi f_\tau R(\eta)/c$, that is linear in the range frequency domain. Moreover, the slope of the phase ramp, $-4\pi R(\eta)/c$, is proportional to the slant range, $R(\eta)$. Since $R(\eta)$ varies in azimuth due to the range migration, the slope of the phase ramp changes with time (along the azimuth direction). Figure 4-1 shows the magnitude and phase response of a simulated single point target after range compression in the range frequency domain. It can be seen that both the constant term, i.e., the phase at zero frequency, and the linear term, i.e., the phase ramp are changing with azimuth time due to the range migration.

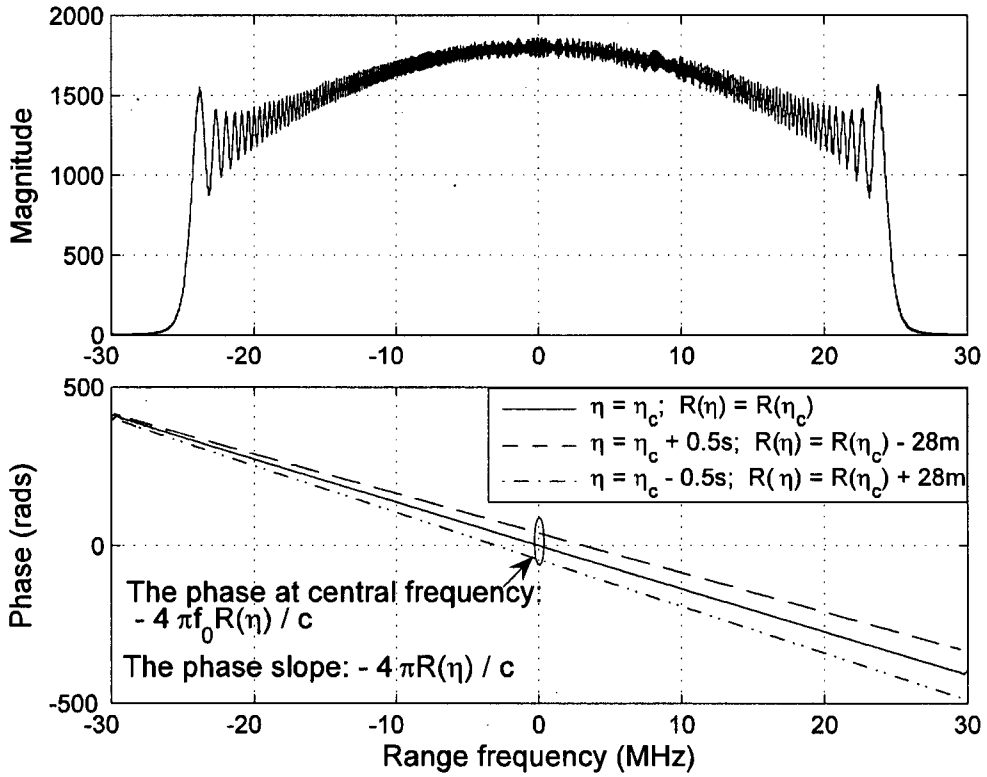

Figure 4-1 Spectrum of the signal after range compression

After converting the signal from the frequency domain to the time domain by a range IFFT, the range-compressed signal can be expressed as [15]:

$$\begin{aligned} s_{rc}(\tau,\eta) &= IFFT_r\{S_{RC}(f_\tau,\eta)\} \\ &= p_r[\tau - 2R(\eta)/c]\, w_a(\eta-\eta_c)\exp\{-j\,4\pi\, f_0\, R(\eta)/c\} \end{aligned} \tag{4.3}$$

where the linear phase range in (4.2) has been converted into a range shift of $2R(\eta)/c$ second. This allows us to observe the relationship between the signal in the range time domain and in the range frequency domain using the Fourier Transform (FT) properties.

4.1.2 Phase relationship

For convenience, we consider a range compressed pulse (target) whose peak is at time, $\tau = 0$. The time-domain signal at its peak can be expressed using the inverse FT of the frequency-domain signal as [24]:

$$\begin{aligned} s_{rc}(0,\eta) &= \int_{f_\tau \min}^{f_\tau \max} S_{RC}(f_\tau,\eta)\exp\{j2\pi f_r \tau\}\, df_\tau \;|_{\tau=0} \\ &= \int_{f_\tau \min}^{f_\tau \max} S_{RC}(f_\tau,\eta)\; df_\tau \end{aligned} \tag{4.4}$$

Because of the equality in (4.4), the phases of the left and right hand sides must be identical. Therefore, we can derive the phase of the time pulse directly from the frequency response by:

$$Phase\big(s_{rc}(0,\eta)\big) = Phase\left(\int_{f_\tau \min}^{f_\tau \max} S_{RC}(f_\tau,\eta)\, df_\tau\right) \tag{4.5}$$

The above equation shows that the phase of the range compressed pulse is equal to the phase of the integrated frequency response. It can be found that the phase corresponding to the large magnitude has more contribution to the final phase than the phase corresponding to small magnitude. This integral relationship is very important when analyzing the phase properties of the two range looks used in the MLBF algorithms. It also shows the importance of the symmetrical look extraction.

4.1.3 The symmetrical magnitude envelope

As discussed in Section 4.1.2, the phase properties of the time-domain signal can be derived from the phase of the frequency-domain signal. This section is to show that if the look magnitudes are symmetrical, the phase of the compressed pulse will be equal to the phase at the spectrum center, which will simplify the calculation in the MLBF algorithm considerably.

To better illustrate how the phase is computed, we introduce a parameter called "*central frequency*". The central frequency, $f_{\tau c}$, is defined as the frequency at which the phase of the look spectrum equals the phase of integrated spectrum on the right hand side of (4.5), and thus equals the phase of the compressed pulse. This definition can be expressed as:

$$\begin{aligned} Phase\left(S_{RC}(f_{\tau c},\eta)\right) &= Phase\left(\int_{f_{\tau}\min}^{f_{\tau}\max} S_{RC}(f_{\tau},\eta)\, df_{\tau}\right) \\ &= Phase\left(s_{rc}(0,\eta)\right) \end{aligned} \tag{4.6}$$

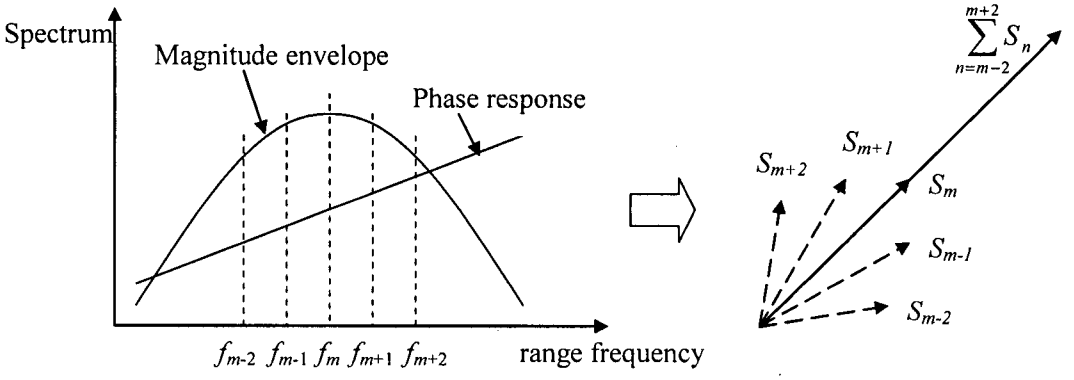

(a) Frequency response with symmetric spectrum

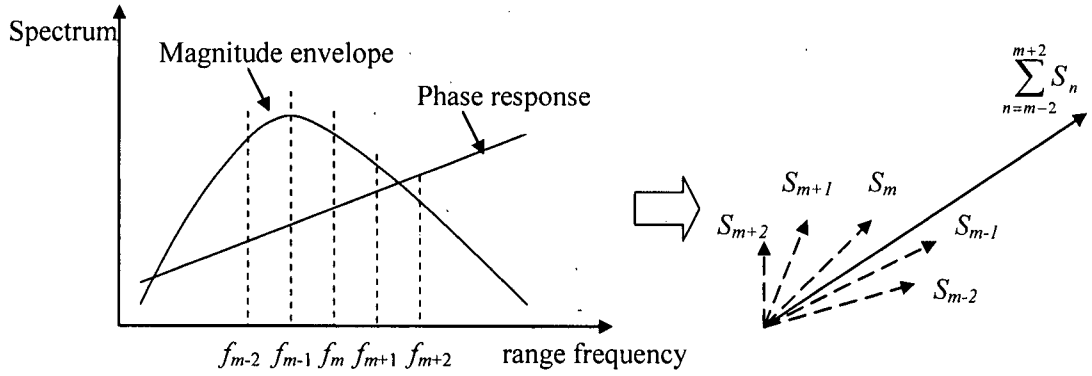

(b) Frequency response with asymmetric spectrum

Figure 4-2 Illustrating how asymmetrical range looks shifts the observed "central frequency" in the range spectrum

Given that the phase response is linear, the magnitude of the frequency response must have a symmetrical shape to guarantee that the "central frequency" is located at the

center of the spectrum. Figure 4-2 illustrates the importance of the symmetrical magnitude using a simple discrete case. When the spectrum has a symmetrical shape as shown in Panel (a), the summation of the five frequency terms has the same phase as the central term.

On the other hand, when the spectrum has an asymmetrical shape, as shown in Figure 4-2 (b), the phase of the summation has an offset from the phase of the central term. It can be seen that only when the spectrum has a symmetrical magnitude envelope, can the central frequency, f_{rc}, be obtained directly from the frequency of the central term, f_{center}. Otherwise, the two frequencies are not equal, $f_{rc} \neq f_{center}$, and a calibration factor is needed to compensate the difference [25].

4.2 Range Look Extraction

In the MLBF algorithm, we extract two looks from the range frequency domain. This section discusses two important issues in this processing.

4.2.1 Symmetric look extraction

As discussed in Section 4.1.3, the symmetrical magnitude spectrum is very important to guarantee that the phase of the range compressed signal can be derived directly from the phase of the central term of the frequency-domain signal. So, in the range look extraction, the two extracted range looks with symmetrical magnitude spectrums are desired. However, in range compression, weighting windows are usually used to reduce the side lobe effect. The weighting window makes the range spectrum curved and thus causes a tilted magnitude distribution when the looks are taken. Therefore, it is expedient to flatten the range spectrum then apply symmetrical look extraction filters. After applying the inverse window, the average magnitude envelope is flat. Figure 4-3 shows the weighted range spectrum after range compression and the flat range spectrum after applying the inverse window.

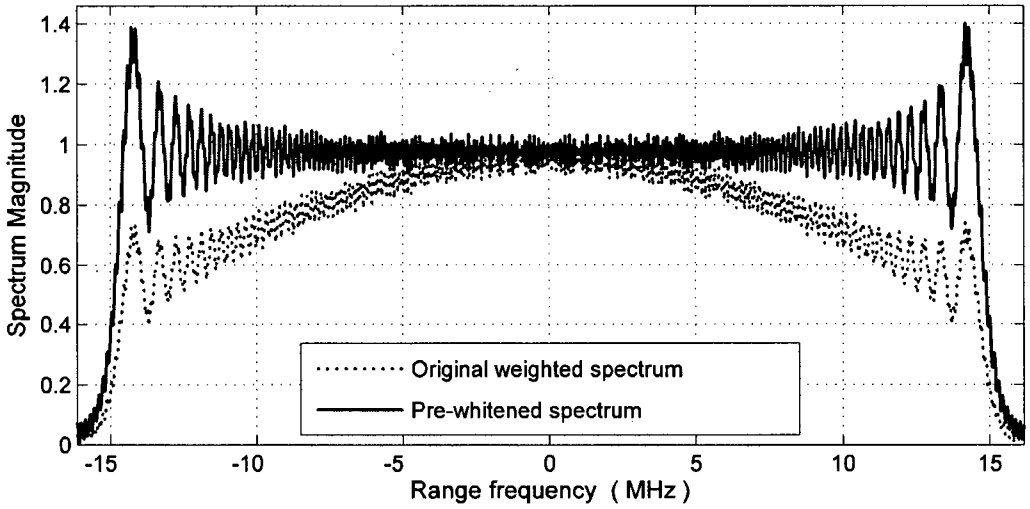

Figure 4-3 Weighted and flattened range spectrums

In addition, two symmetrical look extraction filters are generated to guarantee the symmetrical magnitude spectrums of the extracted range looks. Since the edges of the range spectrum may have some effect on the symmetry of the look spectra, the look extraction windows are tapered to minimize the edge effects.

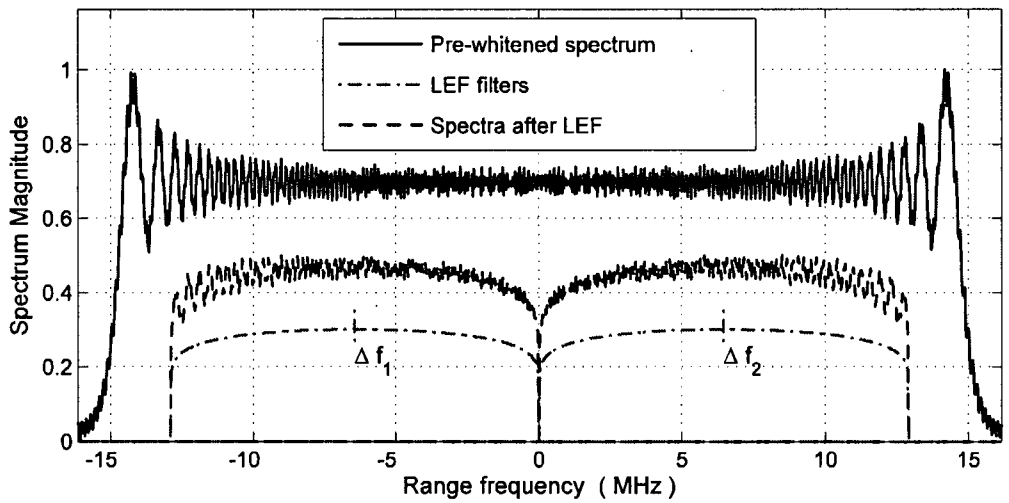

Figure 4-4 Look extraction windows and the extracted looks

Figure 4-4 illustrates the procedure of extracting two range looks using symmetrical windows. The variable, Δf_1 and Δf_2, are the frequency offsets of each look, where Δf_1 = - 6.47 Hz and Δf_2 = 6.47 Hz in this case. As we assume that the range spectrum has been demodulated to baseband (zero center frequency), they are also the actual center frequencies of each look. Moreover, as the spectra of the extracted looks are symmetrical, Δf_1 and Δf_2 also correspond to the "*central frequency*", $f_{\tau c}$, of the two looks.

After extraction, the range looks have a non-zero center frequency, i.e., they are not at baseband. As illustrated in Equation (3.33) and Figure 3.8 of [15], the non-baseband targets have a linear phase ramp through the peak of the pulse. If the central frequency of the range spectrum is Δf, the phase ramp equals $2\pi\, \Delta f\, (\tau - \tau_0)$. According to this concept, the extracted looks can be expressed as follows in the range time domain,

Look 1:

$$\begin{aligned} s_{r1\_nb}(\tau,\eta) &= IFFT_r\{S_{RCF}(f_\tau,\eta)\, W_1(f_\tau)\} \\ &= A_1\; p_r[\tau - 2R(\eta)/c]\, w_a(\eta-\eta_c) \\ &\quad \times \exp\{-j\, 4\pi\, f_0\, R(\eta)/c\} \exp\{-j\, 2\,\pi\, \Delta f_1 (\tau - 2R(\eta)/c)\} \end{aligned} \tag{4.7}$$

and Look 2:

$$\begin{aligned} s_{r2\_nb}(\tau,\eta) &= IFFT_r\{S_{RCF}(f_\tau,\eta)\, W_2(f_\tau)\} \\ &= A_1\; p_r[\tau - 2R(\eta)/c]\, w_a(\eta-\eta_c) \\ &\quad \times \exp\{-j\, 4\pi\, f_0\, R(\eta)/c\} \exp\{-j\, 2\,\pi\, \Delta f_2 (\tau - 2R(\eta)/c)\} \end{aligned} \tag{4.8}$$

where $s_{r1\_nb}(\tau,\eta)$ and $s_{r2\_nb}(\tau,\eta)$ are the signals of the range looks extracted from the non-baseband spectra, $S_{RCF}(f_\tau,\eta)$ is the flattened version of the range-compressed spectrum, (4.2), and $W_1(f_\tau)$ and $W_2(f_\tau)$ are the magnitudes of the range look extraction filters.

The second phase terms in (4.7) and (4.8) show that the range compressed pulses contain phase ramps over the main lobe, $2\,\pi\,\Delta f_1\,\tau$ and $2\,\pi\,\Delta f_2\,\tau$, with a different slope, $2\pi\,\Delta f_k$ for each look. However, as we are interested in the phase changes in the azimuth direction, these range direction phase are distracting.

4.2.2 Shifting to baseband

In order for the azimuth phases of the two looks to be easily compared, the range center frequencies of the two looks can be moved to the same frequency. For conceptual simplicity, the new centers will be moved to zero (baseband), where the phases over the main lobe of the compressed pulses are flat [26].

This bandshifting is done after the range look extraction step. As the shift in the frequency domain corresponds to a modulation in time domain, the signal of two extracted looks after the spectrum shift can be expressed in the time domain as,

Look 1:

$$\begin{aligned} s_{r1}(\tau,\eta) &= IFFT_r\{S_{RCF}(f_\tau+\Delta f_1,\eta)\,W_1(f_\tau+\Delta f_1)\} \\ &= A_1\; p_r[\tau-2R(\eta)/c]\,w_a(\eta-\eta_c) \\ &\quad\times\exp\{-j\,4\pi\,(f_0+\Delta f_1)\,R(\eta)/c\} \end{aligned} \tag{4.9}$$

and Look 2:

$$\begin{aligned} s_{r2}(\tau,\eta) &= IFFT_r\{S_{RCF}(f_\tau+\Delta f_2,\eta)\,W_2(f_\tau+\Delta f_2)\} \\ &= A_1\; p_r[\tau-2R(\eta)/c]\,w_a(\eta-\eta_c) \\ &\quad\times\exp\{-j\,4\pi\,(f_0+\Delta f_2)\,R(\eta)/c\} \end{aligned} \tag{4.10}$$

where $s_{r1}(\tau,\eta)$ and $s_{r2}(\tau,\eta)$ are the signals of the range looks extracted from baseband spectra. It can be seen that after shifting the spectra to baseband, the τ dependence of the phase is removed and the extracted looks are conditioned to generate the appropriate beat signal.

Figure 4-5 illustrates the frequency response and the impulse response of the baseband extracted looks in the single target simulation. It can be seen that the two baseband looks have the same phase slope ramps in the frequency response, but the phases at the central frequency (i.e., zero frequency) are different. In addition, the phases at the central frequency correspond to the phase of the main lobe in the impulse response, which verifies the theory discussed in Section 4.1.2 and 4.1.3.

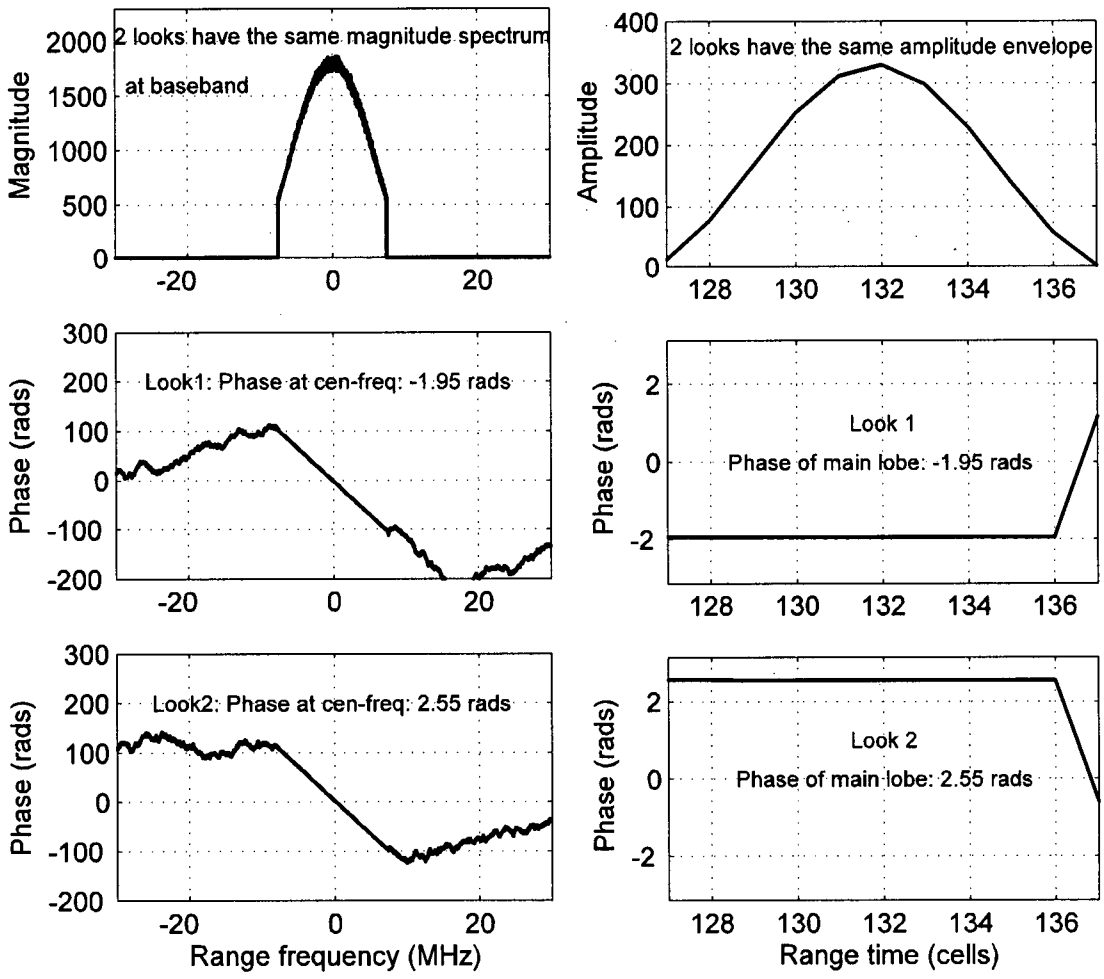

(a) Frequency response (b) Impulse response

Figure 4-5 Illustrating the phase relationship between frequency and time domain after shifting the extracted looks to baseband

4.2.3 Properties of the beat signal

After the shifting, the beat signal can be derived from the two baseband-extracted looks, (4.9) and (4.10), by multiplying one look with the conjugate of the other:

$$\begin{aligned} s_{beat}(\tau,\eta) &= s_{r1}^{*}(\tau,\eta)\, s_{r2}(\tau,\eta) \\ &= \left|A_1\, w_a(\eta-\eta_c)\right|^2 \exp\{-j\,4\,\pi\,\Delta f_r R(\eta)/c\} \end{aligned} \tag{4.11}$$

where $\Delta f_r = \Delta f_2 - \Delta f_1$ is the frequency difference of the two range looks.

It can be seen from (4.11) that the phase of the beat signal varies with azimuth time because of the change of the slant range function, $R(\eta)$. If we expand $R(\eta)$ about the central illuminated time, η_c, and ignore the small higher order components, the range between target and radar can be given by:

$$R(\eta) = R(\eta_c) - V_r \sin\theta_{r,c}(\eta - \eta_c) + \frac{1}{2}\frac{V_r^2 \cos^2\theta_{r,c}}{R(\eta_c)}(\eta - \eta_c)^2 \qquad (4.12)$$

where V_r is the effective radar velocity and $\theta_{r,c}$ is the beam squint angle measured in the slant range plane.

In (4.12), $R(\eta)$ has a linear and quadratic components. The linear component gives rise to a pure sine wave in the beat signal, whose frequency is given by:

$$f_{beat} = -\frac{2\Delta f_r}{c}\frac{dR(\eta)}{d\eta} = \frac{2\Delta f_r V_r \sin\theta_{r,c}}{c} = -\frac{\Delta f_r}{f_0} f_{\eta c} \qquad (4.13)$$

where $f_{\eta c} = -2 V_r \sin\theta_{r,c} / \lambda$ is the Doppler centroid frequency.

The quadratic component gives rise to a non-zero bandwidth in the beat signal. Usually the bandwidth of the beat signal is quite small compared to the PRF. Hence, the beat signal can be approximated by a single frequency with noise. The bandwidth of the beat signal will be discussed in more detail in Section 5.1.

In summary, the beat signal has an average frequency proportional to the absolute Doppler centroid frequency, which we are trying to estimate. The proportionality factor is the fractional separation of the range looks, $\Delta f_r / f_0$. At this point, the requirement of the symmetrical magnitude spectrum is recognized. If the looks are not symmetrical, the average frequency calculated from the beat spectrum will not equal (4.12), and a different look separation Δf_r must be "calibrated", as illustrated in Figure 4-2.

4.3 Cross Beating and the Use of RCMC

As described in the opening paragraph, as the existence of RCM in the received data may limit the signal duration within one range cell and reduce the sensitivity of the frequency estimation, there are some advantages to using RCM Correction (RCMC) in the MLBF algorithm. In this section, we discuss two phenomena that reduce the purity of the beat signal, and how range cell migration correction (RCMC) can be used to alleviate them.

4.3.1 The effect of the cross beating

The MLBF concept outlined in Section 4.2 is based on a single target in each range cell, which leads to the derivation of the beat signal, (4.13). However, in practice there is inevitably more than one target in each range cell. This leads to a cross beating effect that distorts the beat signal [13]. The cross beating arises when more than one significant target is present in a range cell, and the Look1 of one target beats with Look 2 of other targets. The beating between different targets (cross-beating) gives rise to spurious frequency components in the beat spectrum. Depending on the number, strength and distribution of the extra targets, the cross-beating can distort the beat spectrum or add noise to it.

In order to understand the effect of the cross beating, we first analyze the case of two targets. Consider two targets P and Q, which are in the same range cell but separated in azimuth, with beam center crossing times, η_P and η_Q. Then, the two range looks, $s_1(\eta)$ and $s_2(\eta)$, can be expressed as [13],

Look 1:

$$\begin{aligned} s_1(\eta) &= s_{P1}(\eta) + s_{Q1}(\eta) \\ &= A_P w_a(\eta-\eta_P)\exp\left\{-j\frac{4\pi}{c}(f_0+\Delta f_1)R(\eta-\eta_P)\right\} \\ &\quad + A_Q w_a(\eta-\eta_Q)\exp\left\{-j\frac{4\pi}{c}(f_0+\Delta f_1)R(\eta-\eta_Q)\right\} \end{aligned} \tag{4.14}$$

and Look 2:

$$\begin{aligned} s_2(\eta) &= s_{P2}(\eta) + s_{Q_2}(\eta) \\ &= A_P w_a(\eta - \eta_P)\exp\left\{-j\frac{4\pi}{c}(f_0 + \Delta f_2)R(\eta - \eta_P)\right\} \\ &\quad + A_Q w_a(\eta - \eta_Q)\exp\left\{-j\frac{4\pi}{c}(f_0 + \Delta f_2)R(\eta - \eta_Q)\right\} \end{aligned} \tag{4.15}$$

where $s_{P1}(\eta)$, $s_{P2}(\eta)$, and $s_{Q1}(\eta)$, $s_{Q2}(\eta)$ are the range compressed signals of Look 1 and Look 2 for Targets P and Q individually, A_P and A_Q are the amplitude of the targets after range compression and look extraction.

Then, the beat signal in this case becomes:

$$\begin{aligned} s_{beat}(\eta) &= s_1^*(\eta)\cdot s_2(\eta) \\ &= s_{P1}^*(\eta)\cdot s_{P2}(\eta) + s_{Q1}^*(\eta)\cdot s_{Q2}(\eta) \\ &\quad + s_{P1}^*(\eta)\cdot s_{Q2}(\eta) + s_{Q1}^*(\eta)\cdot s_{P2}(\eta) \end{aligned} \tag{4.16}$$

In (4.16), the first term represents the beat signal generated by Target P alone, the second term represents the beat signal generated by Target Q alone. These two auto-beat terms provide correct beat frequency, as in the case of single target. However, the third and fourth terms represent the signals generated by a target in one look beating with another target in the other look, a phenomenon referred to as cross beating.

The cross beating leads to extra frequencies in the beat signal spectrum. The third term of (4.16) can be expanded as:

$$\begin{aligned} & s_{P1}^*(\eta)\cdot s_{Q2}(\eta) \\ &= A_P^* A_Q w_a(\eta - \eta_c - \eta_P) w_a(\eta - \eta_c - \eta_Q) \\ & \exp\left\{j\frac{4\pi}{c}\left[(f_0 + \Delta f_1)R(\eta - \eta_P) - (f_0 + \Delta f_2)R(\eta - \eta_Q)\right]\right\} \end{aligned} \tag{4.17}$$

Using the expansion for $R(\eta)$ of (4.12), the frequency of this cross term is:

$$
\begin{aligned}
f_{P^*Q} &= \frac{2}{c}\frac{d\left[(f_0+\Delta f_1)R(\eta-\eta_P)-(f_0+\Delta f_2)R(\eta-\eta_Q)\right]}{d\eta}\Bigg|_{\eta=\eta_c} \\
&= \frac{2(\Delta f_2-\Delta f_1)V_r\sin\theta_{r,c}}{c}+\frac{2V_r^{\,2}\cos^2\theta_{r,c}f_0}{c\,R(\eta_c)}(\eta_P-\eta_Q) \\
&= f_{beat}+K_a\Delta\eta
\end{aligned}
\tag{4.18}
$$

where f_{beat} is the single-target beat frequency defined in (4.13), K_a is the Doppler FM rate of the signal, and $\Delta\eta=\eta_Q-\eta_P$ is the separation of the two targets in azimuth time.

Similarly, the cross frequency of the forth term of (4.16) can be expressed as:

$$
f_{PQ^*}=f_{beat}-K_{a,dop}\Delta\eta \tag{4.19}
$$

The cross beating leads to these extra frequencies in the beat signal spectrum. Equations (4.18) and (4.19) show that the offset, $\pm K_a\Delta\eta$, of the cross-beating frequencies from the expected beat frequency depends on the Doppler FM rate and the target separation, but does not depend on the look separation, $\Delta f_2-\Delta f_1$.

The amplitude of the cross-beating signals is usually less than the main beat signal, as one target is often smaller than the other target and because the duration of the overlap of the two targets is less than the exposure time of one target. Thus, the beat spectrum is not distorted much if $|A_P| >> |A_Q|$ and/or if the targets are well separated in azimuth. However, the effect of the cross beating on the spectrum becomes noticeable when A_Q becomes close to A_P in magnitude and there is substantial overlap between the targets.

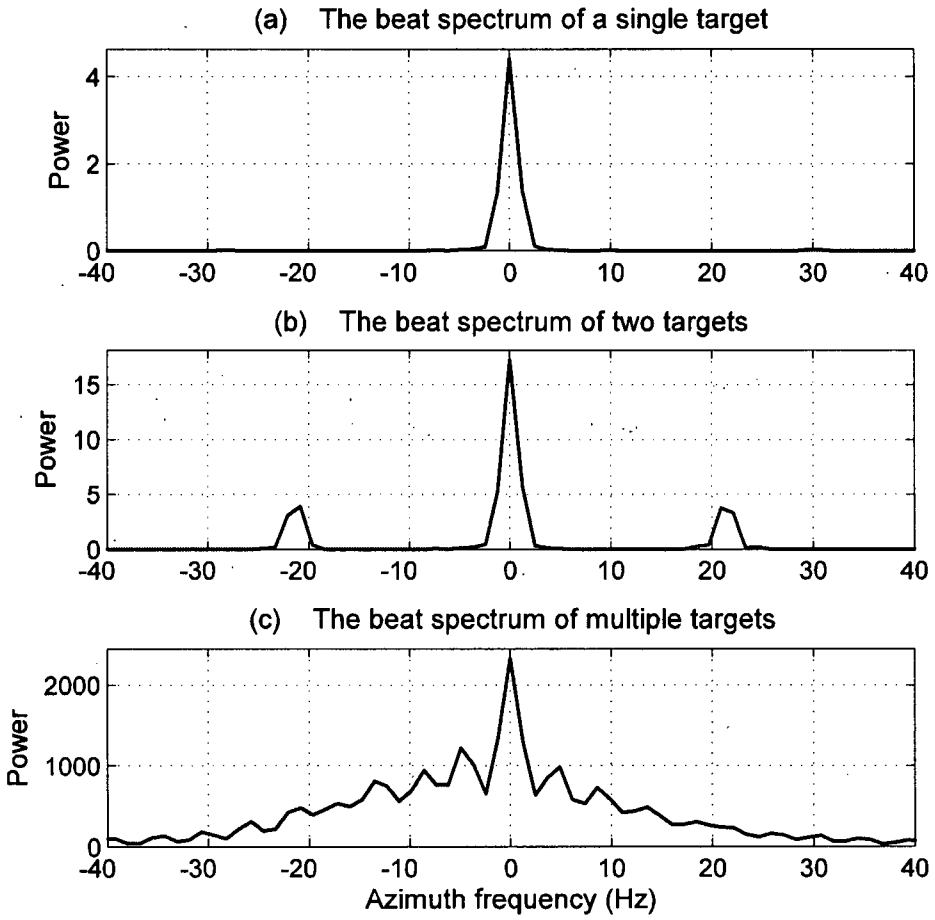

Figure 4-6 The effect of cross beating in the beat spectrum

Figure 4-6 uses a discrete-target simulation to illustrate to cross-beating effect that occurs when more than one target is present in the same range cell. Panel (a) shows the beat spectrum of single target in one range cell, and Panel (b) shows the beat spectrum of two overlapping targets. For simplicity, the Doppler centroid is assumed to be zero, so there is no range migration and the expected beat frequency is zero.

Comparing the top two panels, it can be seen that the cross beating creates two extra peaks in the beat spectrum of Panel (b). The strengths of the two targets are the same and the azimuth target separation is 15 pulses or 0.1193 seconds. The exposure time of each target is 700 pulses or 0.55 seconds, the PRF is 1257 Hz, the FM rate is -1790 Hz/s, parameters taken from the RADARSAT-1 FINE mode. With these parameters, the 15-cell azimuth separation gives a frequency shift of ± 21.4 Hz for the cross-beat

components. Therefore, the frequency shift of the cross-beating components observed in Panel (b) agrees with the offset frequencies of (4.18) and (4.19).

Panel (c) shows the extra distortion that occurs in the beat spectrum when there are many targets in the same range cell. In this simulation, there are 20 targets with a random separation in azimuth between 1 and 3 pulses. The target amplitudes are equal at one unit, and Gaussian noise is added with an RMS value of unity. The cross-beating components in the same range cell add coherently, which can result in spurious peaks and nulls in the beat spectrum.

In general, the cross-beating increases with the density of the targets. When the density is too high, the beat frequency may not be detected within the ambiguity error limits. That is why it is more difficult to estimate the beat frequency when there are many targets with similar magnitude, as in homogeneous, low contrast scenes.

4.3.2 The effect of RCM

A significant amount of range cell migration (RCM) is often present in satellite SAR data. With the existence of RCM, the signal trajectory has a slope over azimuth and the signal energy can be spread over several range cells during the exposure time. In this case, each target is fragmented in each range cell. As a consequence, the fragmented exposure time of the target in each rang cell leads to a wider peak and less resolution in the beat signal spectrum. Moreover, the partial exposures that exist with RCM create a higher density of targets in each range cell, resulting in more cross beating.

The effect of RCM is illustrated in Figure 4-7, which compares the trajectories of two targets that have a small displacement in range and azimuth. Panel (a) shows the locus of target energy in the range compressed data with no RCM, as in the case where the beam is steered to zero Doppler. When the Doppler centroid is well away from zero, significant RCM can be present, as shown in Panel (b).

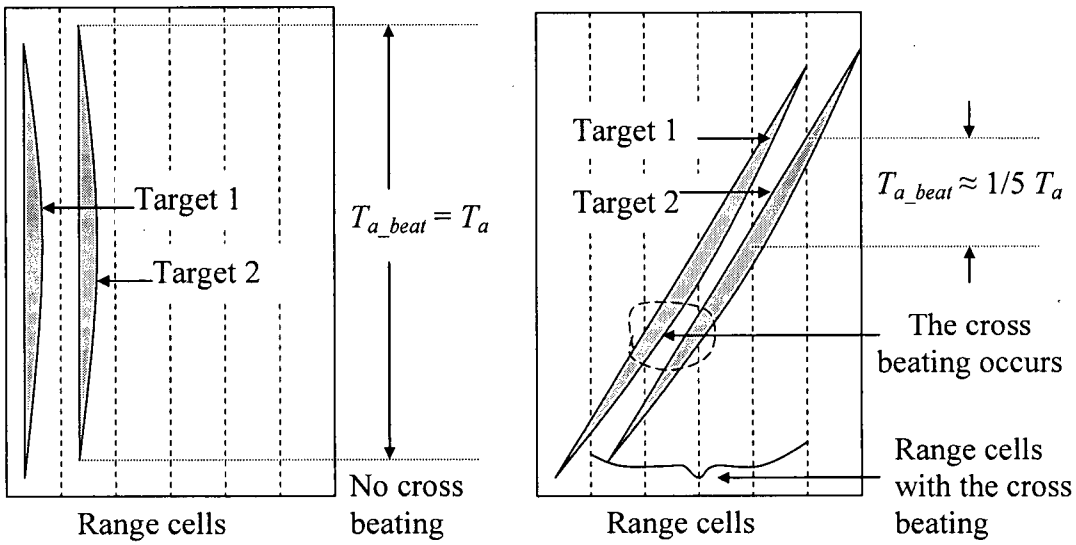

(a) With No RCM (b) With significant RCM

Figure 4-7 Distribution of the energy of two targets in range-compressed data

Figure 4-7 illustrates the effect of RCM, which compares the trajectories of two targets that have a small displacement in range and azimuth. Panel (a) shows the locus of target energy in the range compressed data with RCM, while Panel (b) shows the locus without RCM. It also can be seen that with RCM the target exposure time in each cell, $T_{a\_beat} = 1/5\ T_a$, is only one fifth of that without RCM, $T_{a\_beat} = T_a$. In addition, the partial exposures that exist with RCM create a higher density of targets in each range cell, resulting in more cross beating.

Two effects are noticed in Figure 4-7. First, the exposure time of each target is reduced by the RCM, when observed within a single range cell. In this example, the exposure time within a range cell has been reduced to $T_a / 5$ by the 5-cell RCM, where Ta is the full exposure time of a target. As the beat signal takes place within one range cell, the reduced exposure time means that the resolution of the beat signal is broadened. Second, while there is only one target in each range cell when there is no RCM, the RCM has created two targets in each cell. This creates the cross-beating effect discussed in Section 4.3.1, as long as the partial exposures overlap. Both of these effects reduce the

sensitivity of the beat frequency estimation. The cross-beating effect tends to get larger when a high density of targets is present, although the target overlap is reduced when the exposure within a cell is smaller.

Figure 4-8 illustrates the effect of the RCM on the beat spectra using a discrete-target simulation. RADARSAT-1 FINE parameters are used, with a PRF of 1257 Hz and an exposure time of 700 pulses. Three cases of RCM are shown. In the first row, the Doppler centroid is set to zero, so there is no linear RCM, and only a small amount of quadratic RCM (about half a cell). In the second row, the Doppler centroid is set to 4.7 PRFs, giving the target(s) an RCM of 20 cells. In the third row, the Doppler centroid is set to 9.4 PRFs, giving the target(s) an RCM of 40 cells.

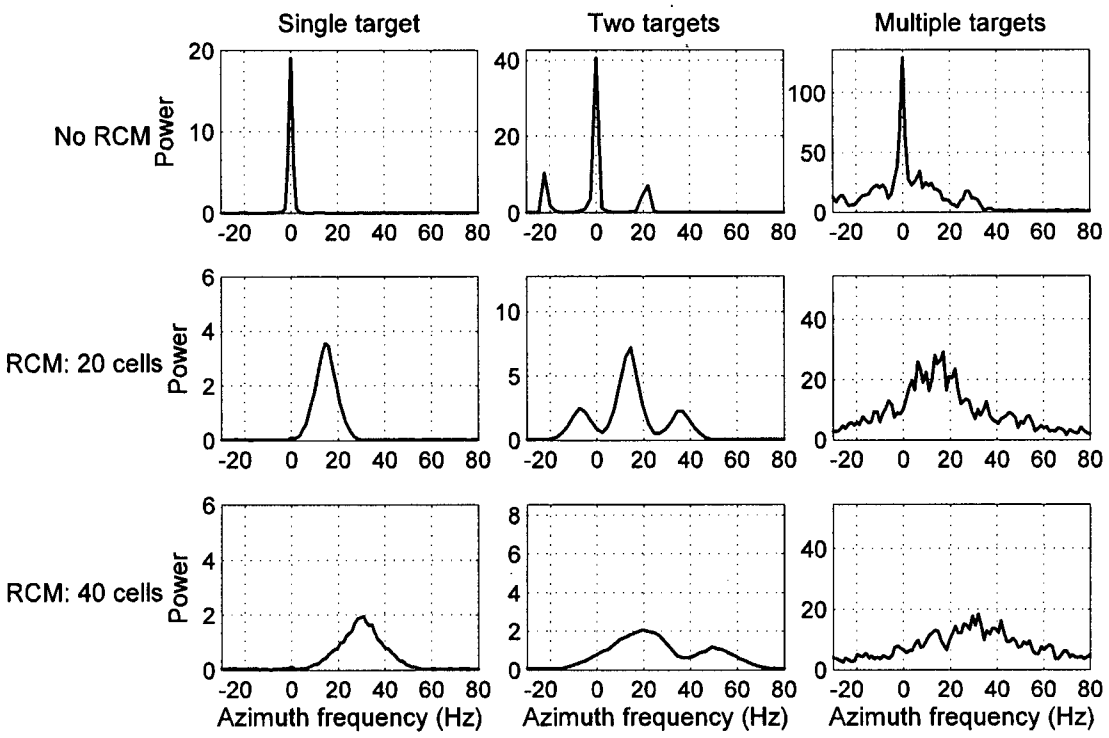

Figure 4-8 Illustrating the effects of RCM on the beat signal resolution – single, double and multiple targets case

The first column shows the beat spectrum in the case of single target. This allows the effect of limited target exposure time in one range cell to be isolated. When there is no RCM, the target is fully exposed in the range cell, and the beat signal resolution is the finest. However, when RCM is appreciable, the reduced exposure time in each range cell broadens the spectrum of the beat signal, and lowers the height of the peak.

The second column shows the beat spectrum when there are two targets of the same strength in the same range cell, with a separation of 15 pulses, as in Figure 4-6. In the first row, the RCM is zero, so the exposure time is 700 pulses and the target overlap is 685 cells. The long exposure time and overlap gives strong auto-beat and cross-beat components, with a fine resolution. In the second row of Column 2, the exposure in each range cell has been reduced to about 45 cells by the RCM, and the target overlap similarly reduced. The auto-beat and the cross-beat strengths have been reduced accordingly, and the resolution of the peaks has broadened. In the third row, the RCM has been increased to 40 cells, and the reduced exposure has further broadened the resolution to the point where the auto- and cross-beat signals are becoming mixed.

The third column shows the results when there are multiple targets in each range cell. In this part of the simulation, 100 targets are randomly placed in a 30×30 sample square, with Rayleigh amplitude distribution and random phases. The cross beating is now much more complex, and adds noise-like components to the spectrum. In the first column, it is easy to see how the three values of Doppler centroid change the beat frequency from zero to 17 and 34 Hz. With a single target in one range cell, the correct beat frequency is easily estimated. Even if there were other targets with much smaller magnitude present, the strong target would dominate the spectrum, and the beat frequency would likely be estimated correctly. However, the second and third columns show that when there are two or more targets of comparable magnitude present, the beat frequency can easily become obscured, possibly leading to Doppler ambiguity estimation errors. For example, in Row 3 of Column 2, the beat frequency has apparently been shifted from 34 to 20 Hz. In summary, the limited target exposure in one range cell, the smaller target

overlap and the cross-beating of multiple targets tend to increase the error in the estimation of the beat frequency as the RCM increases

4.3.3 Benefit of applying RCMC

In this section, we discuss the benefits of applying RCM Correction (RCMC) before the beat frequency is estimated. When RCMC is applied with the correct ambiguity number, each target is confined to one range cell, and the beat signal arising from a target beating with itself (auto-beating) has the finest possible resolution.

However, there is another effect of RCMC, which may help or hinder the beat signal frequency estimation, depending on the distribution and strength of targets. RCMC may bring other targets into the same range cell, with a full exposure. The overlap with the existing target may be larger, giving rise to a stronger, sharper, cross-beat component. Figure 4-9 illustrates how RCMC can help to improve the beat frequency estimation. In the simulation, 100 targets are used, randomly placed within a 30×30 sample grid. Their amplitudes have a Rayleigh distribution, and their phases are random. Panel (a) shows the beat spectrum before RCMC, while Panel (b) shows the spectrum after RCMC. The beat spectrum has been averaged incoherently across range cells.

Due to the effect of the RCM and the cross beating, the spectrum before RCMC is wide and noisy in Panel (a). But after RCMC in Panel (b), a much cleaner, narrower spectrum results from increasing the exposure time in each range cell, and reducing the cross beating. In this example, there is an average of three targets in each range cell. The narrow peak increases the accuracy of the MLBF algorithm by improving the estimation of the beat frequency.

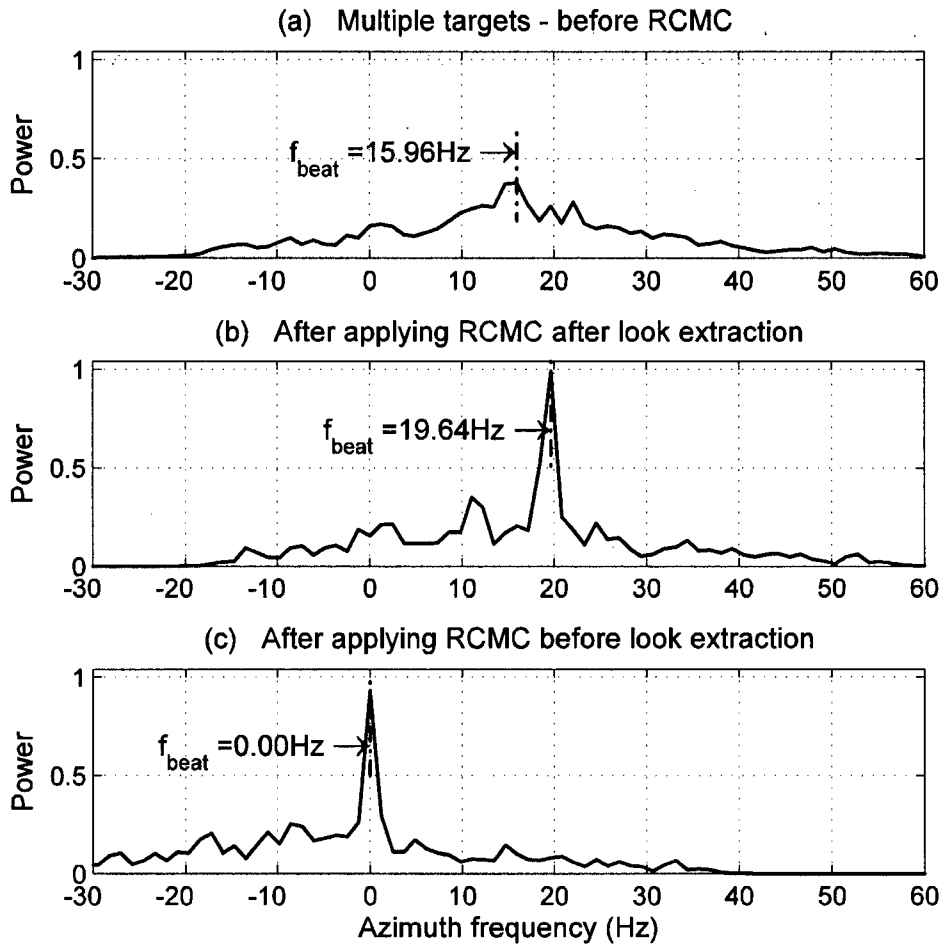

Figure 4-9 Illustrating the effects of RCMC on the beat signal resolution

4.3.4 Examples with real data

In our study, the RADARSAT-1 fine mode scene of Vancouver is selected to illustrate the properties of Doppler estimators. The processed image of the whole scene is shown in Figure 4-10. There is water, farmland, city and mountains in the scene [15].

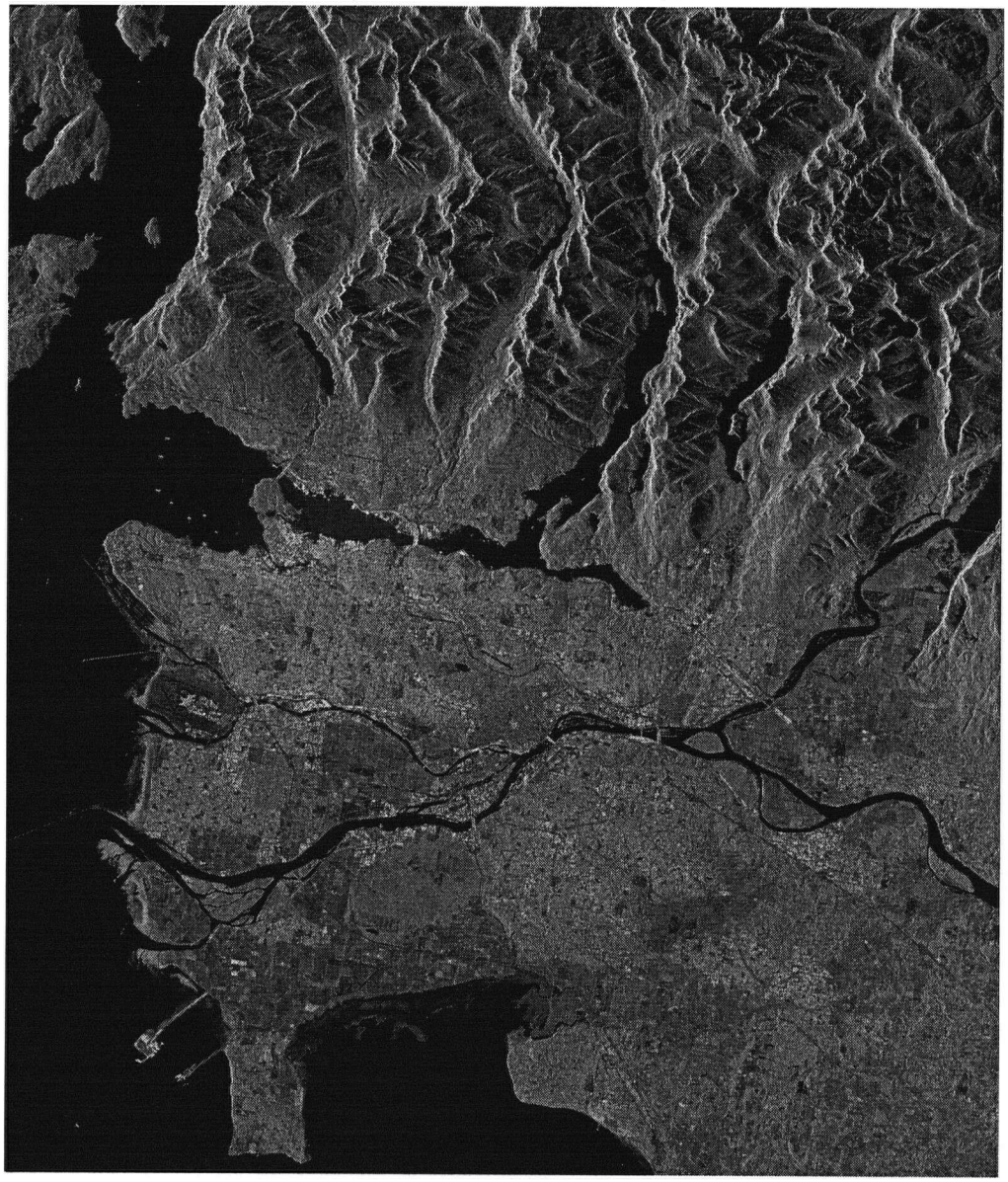

Figure 4-10 RADARSAT-1 scene of Vancouver used in the Doppler estimation experiments [15]

The benefits of applying RCMC is further illustrated in Figure 4-11, using the "ships scene" with the bright targets around Vancouver harbor. In Panel (a), cross-beating makes the spectrum asymmetrical and the peak occurs at an incorrect frequency. Panel (b) illustrates how RCMC reduces cross-beating and narrows the bandwidth of the beat signal. The correct ambiguity number can then be obtained from the frequency estimate.

The origin of the asymmetry in Panel (a) is not known ---- it is likely due to the coherent addition of the many scatters in each large ship combined with a small amount of range curvature in the C-band data.

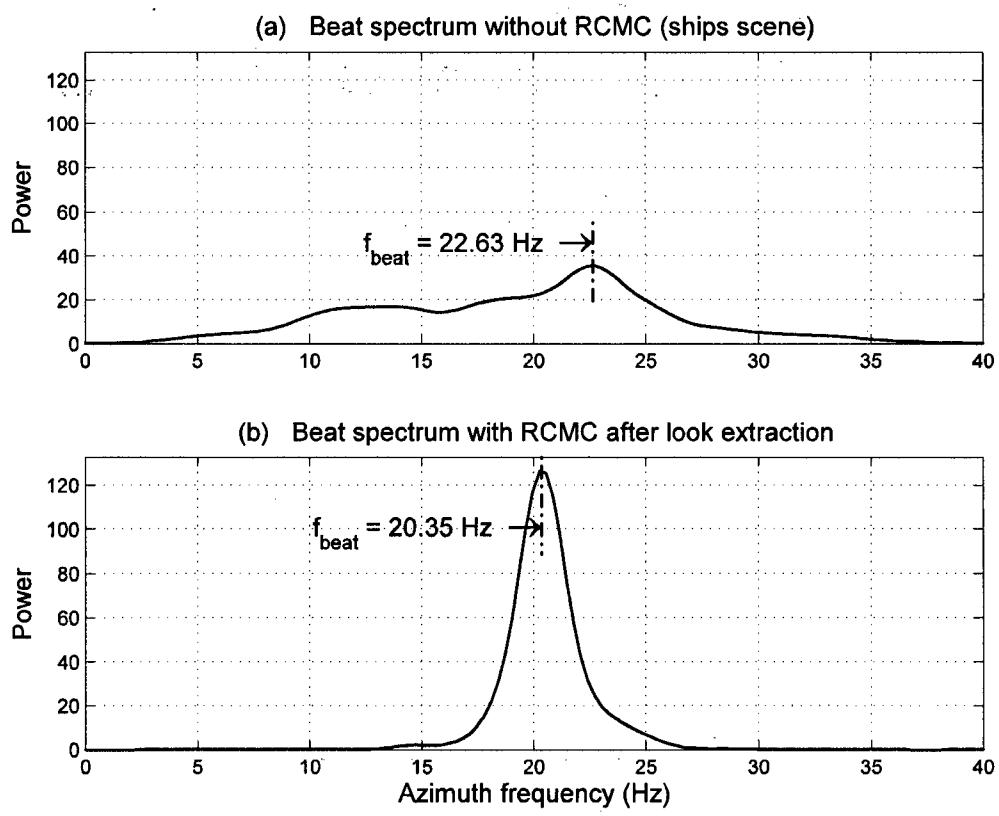

Figure 4-11 Effects of RCMC on the beat signal resolution in the Vancouver "ships" scene

In the example of the "ships" scene, there are only a few strong targets in each range cell. In lower contrast parts of the scene, a large number of similar-size, weak targets in one range cell can hide the peak in the spectrum. This effect is illustrated in Figure 4-12, where a low contrast part of the Vancouver scene in the mountains is selected. Although the spectral peak is quite obscure compared to the high-contrast scene, it can be seen that RCMC does help by revealing a small peak at the correct beat frequency.

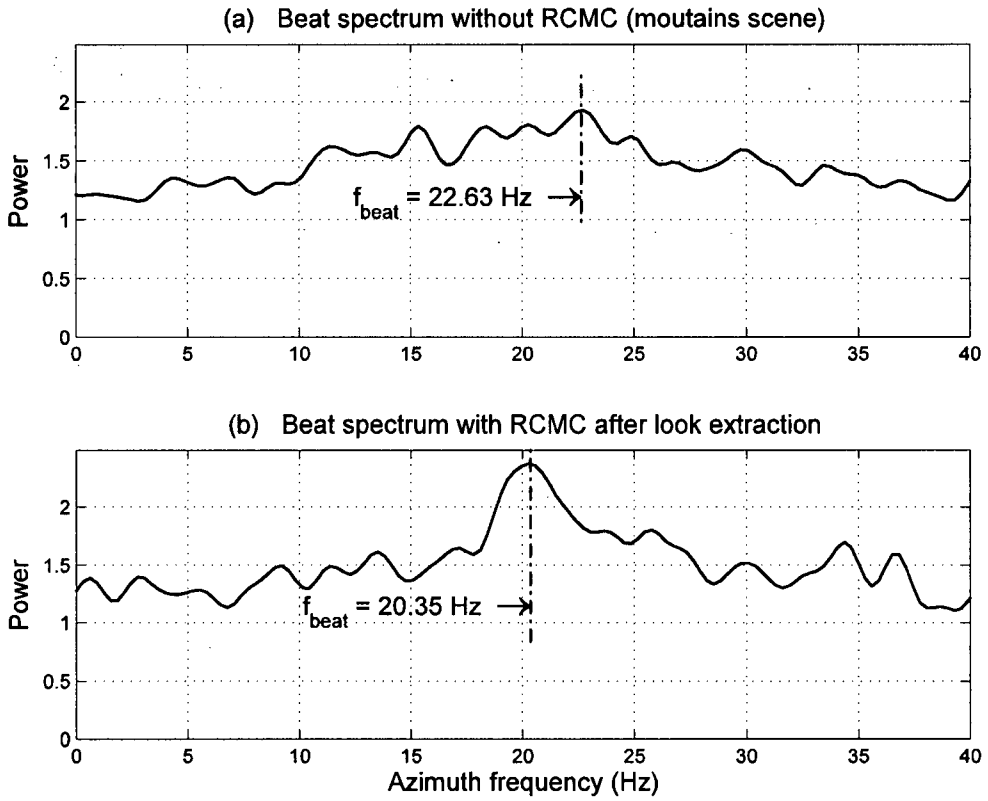

Figure 4-12 Effects of RCMC on the beat signal resolution in the Vancouver "mountains" scene

4.3.5 Why RCMC must be applied after look extraction

As illustrated Section 4.1.2, it is the variation along azimuth of the slope of the phase in the range spectrum that makes the MLBF algorithm work. Therefore, if RCMC is to be applied in the MLBF algorithm, one must be careful not to destroy this phase variation.

Case I: RCMC before look extraction

If we apply RCMC before range look extraction, the RCMC changes the target range from $R(\eta)$ to R_0 in all range lines in (4.2), where R_0 is the reference slant range for that target. This has the effect of removing the phase ramp along azimuth time after the

range FFT, so that when the two range looks are extracted, there is no phase difference between the two looks.

To observe this, note that the phase ramp in the range frequency domain in (4.2) has been changed from - $4\pi f_\tau R(\eta)/c$ to - $4\pi f_\tau R_0/c$ by the RCMC, so the range phase slope, $4\pi R_0/c$, is no longer azimuth dependent. In other words, the range-compressed signal in the range frequency domain of (4.2) has been changed to:

$$S_{RCMC}(f_\tau,\eta) = A_1' W_r(f_\tau) w_a(\eta-\eta_c) \exp\left\{-j\frac{4\pi f_0 R(\eta)}{c}\right\} \exp\left\{-j\frac{4\pi f_\tau R_0}{c}\right\} \tag{4.20}$$

The second exponential factor shows that the slope of the phase ramp in f_τ is now the same in every range line. Note that the $R(\eta)$ dependency in the first exponential term still remains, because it was created by the demodulation process, and is not affected by the RCMC. Then, the only azimuth phase change is due to the first exponential term, and as this term does not depend upon f_τ, the azimuth phase change is the same for each look. Figure 4-13 illustrates the effect of RCMC on the phase response in simulation, which verifies the discussion above.

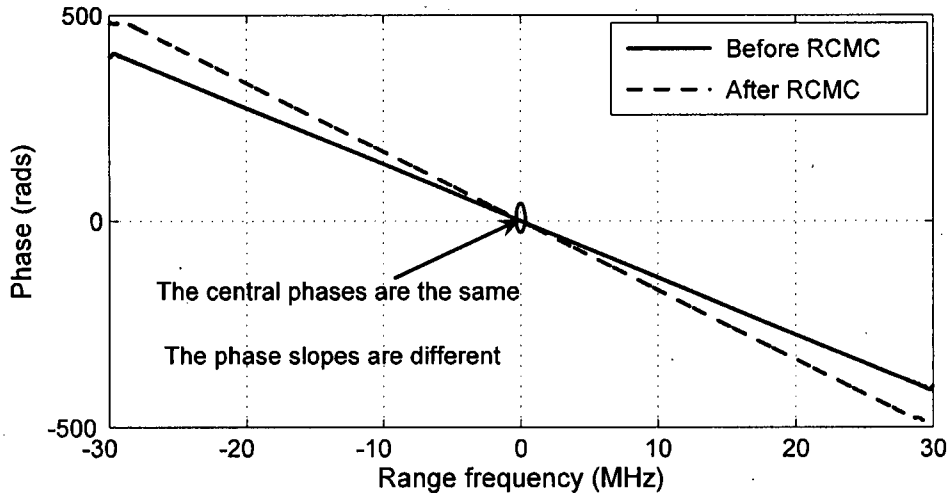

Figure 4-13 The effect of RCMC on the phase response

Correspondingly, the two range looks extracted from the signal after RCMC can be expressed as,

Look1:

$$s_{r1}'(\tau,\eta) = A_1\ p_r[\tau - 2R_0/c]\, w_a(\eta-\eta_c) \times \exp\{-j\,4\pi\ f_0\ R(\eta)/c\}\exp\{j\,4\,\pi\,\Delta f_1\ R_0/c\} \tag{4.21}$$

And Look 2:

$$s_{r2}'(\tau,\eta) = A_1\ p_r[\tau - 2R_0/c]\, w_a(\eta-\eta_c) \times \exp\{-j\,4\pi\ f_0\ R(\eta)/c\}\exp\{-j\,4\,\pi\,\Delta f_2\ R_0/c\} \tag{4.22}$$

As a result, in the case of applying the RCMC before look extraction, the beat signal can be expressed as:

$$s_{beat}'(\tau,\eta) = s_{r1}'^{*}(\tau,\eta)\ s_{r2}'(\tau,\eta) = \left|A_1\ w_a(\eta-\eta_c)\right|^2 \exp\{-j\,4\,\pi\,\Delta f_r\ R_0/c\} \tag{4.23}$$

As the phase of the beat signal is a constant in azimuth (compare (4.23) with (4.11)), the beat signal has zero frequency, and the information used to obtain a Doppler estimate has been lost, as follows:

$$f_{beat}' = \frac{2\Delta f_r}{c}\frac{dR_0}{d\eta} = 0 \tag{4.24}$$

Figure 4-14 illustrates the simulation results in this case. It can be seen that the phases of the two looks have the same changing pattern and hence their difference is constant. As a consequence, the beat frequency obtained from the two looks is zero, and thus cannot be used to obtain a Doppler estimate.

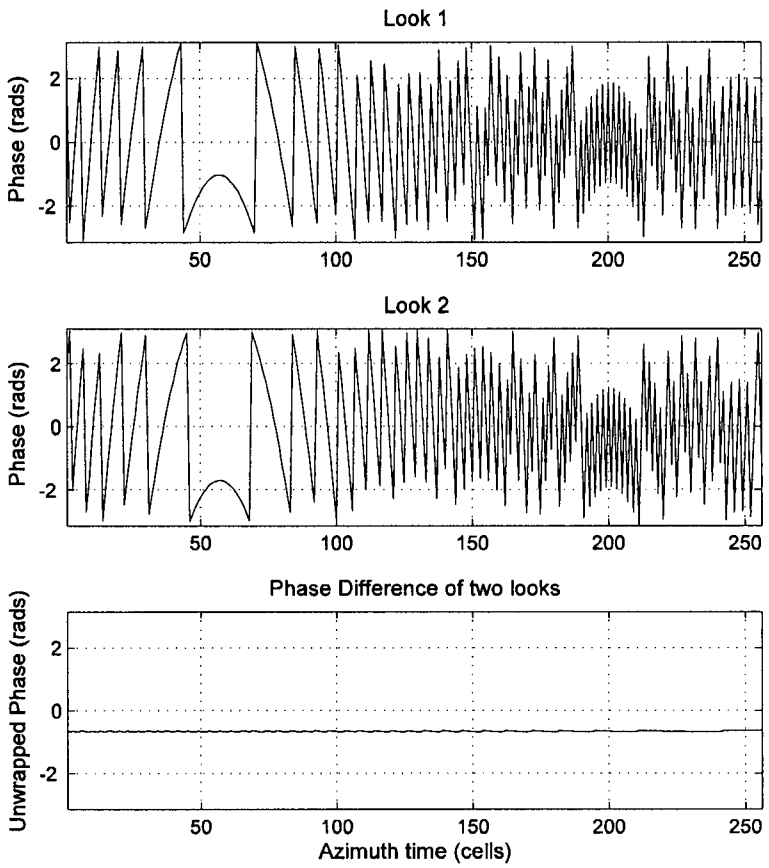

Figure 4-14 Azimuth phase when RCMC before the look extraction

Case II: RCMC after look extraction

On the other hand, if RCMC is applied after the baseband look extraction, the phases in the compressed pulses of two looks are not changed. When RCMC applied to the signal (4.9) and (4.10), only the range envelope is changed from $p_r[\tau - 2R(\eta)/c]$ to $p_r[\tau - 2R_0/c]$, but the phase term (the argument of the complex exponential) is not affected. The two range looks in this case can be expressed as,

Look 1:

$$s_{r1}''(\tau,\eta) = A_1\ p_r[\tau - 2R_0/c]\, w_a(\eta-\eta_c) \times \exp\{-j\,4\pi\ f_0\ R(\eta)/c\}\exp\{j\,4\,\pi\ \Delta f_1\ R(\eta)/c\} \tag{4.25}$$

And Look 2:

$$s_{r2}''(\tau,\eta) = A_1\ p_r[\tau - 2R_0/c]\, w_a(\eta-\eta_c) \times \exp\{-j\,4\pi\ f_0\ R(\eta)/c\}\exp\{-j\,4\,\pi\ \Delta f_2\ R(\eta)/c\} \tag{4.26}$$

Consequently, the azimuth phase difference of the two looks still maintains the correct dependence on the range migration. Figure 4-15 shows azimuth phase plots when RCMC is applied after the look extraction. Comparing to Figure 4-14, the phase difference of two looks is not constant, but changing with azimuth time. Moreover, it can be seen that the phase difference is almost a linear function of azimuth time, and the slope of the linear phase gives the value of the beat frequency. As a result, the correct Doppler estimate can be obtained from this phase variation.

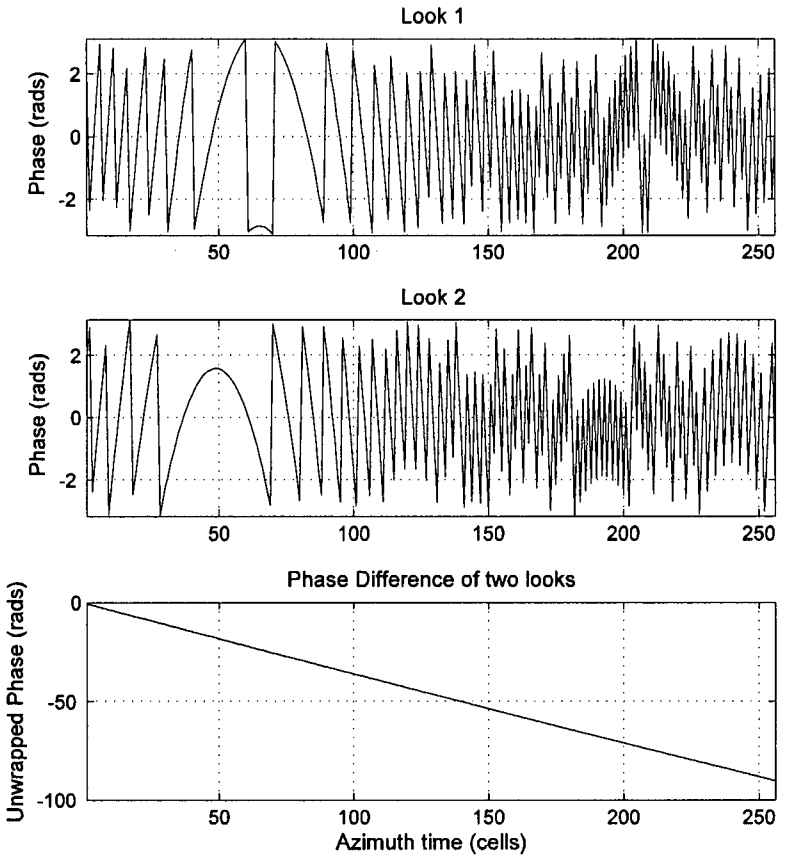

Figure 4-15 Azimuth phase when RCMC after the look extraction

These effects are illustrated in the Panels (b) and (c) of Figure 4-9. In Panel (b), RCMC is applied after range look extraction, and the benefits of RCMC described in Section 4.3.3 are obtained. In Panel (c), however, RCMC has been applied before range

look extraction, the beat frequency has been shifted to zero, and the distinctive beat frequency, has been lost.

In conclusion, applying RCMC after look extraction gives the same beat frequency as without RCMC, but applying RCMC before the look extraction shifts the beat frequency to zero. Therefore, the RCMC should be applied after the baseband look extraction in order to preserve the correct beat frequency [26].

4.4 Iterative Procedure Using RCMC

The existing MLBF algorithm is not as reliable as it could be, due to the coarse resolution of the beat frequency and the occurrences of the cross-beating between multiple targets in one range cell. In this section, the implementation scheme of the method using RCMC is discussed and the experimental results on real satellite SAR data show that this method has a better performance than the existing MLBF algorithm.

4.4.1 The iterative procedure

RCMC can only be applied correctly if the Doppler ambiguity number is known, which is not available until after the current estimation procedure is completed. Hence, in order to take advantage of the RCMC routine in the MLBF algorithm, an iterative procedure is proposed --- see the flowchart in Figure 4-16.

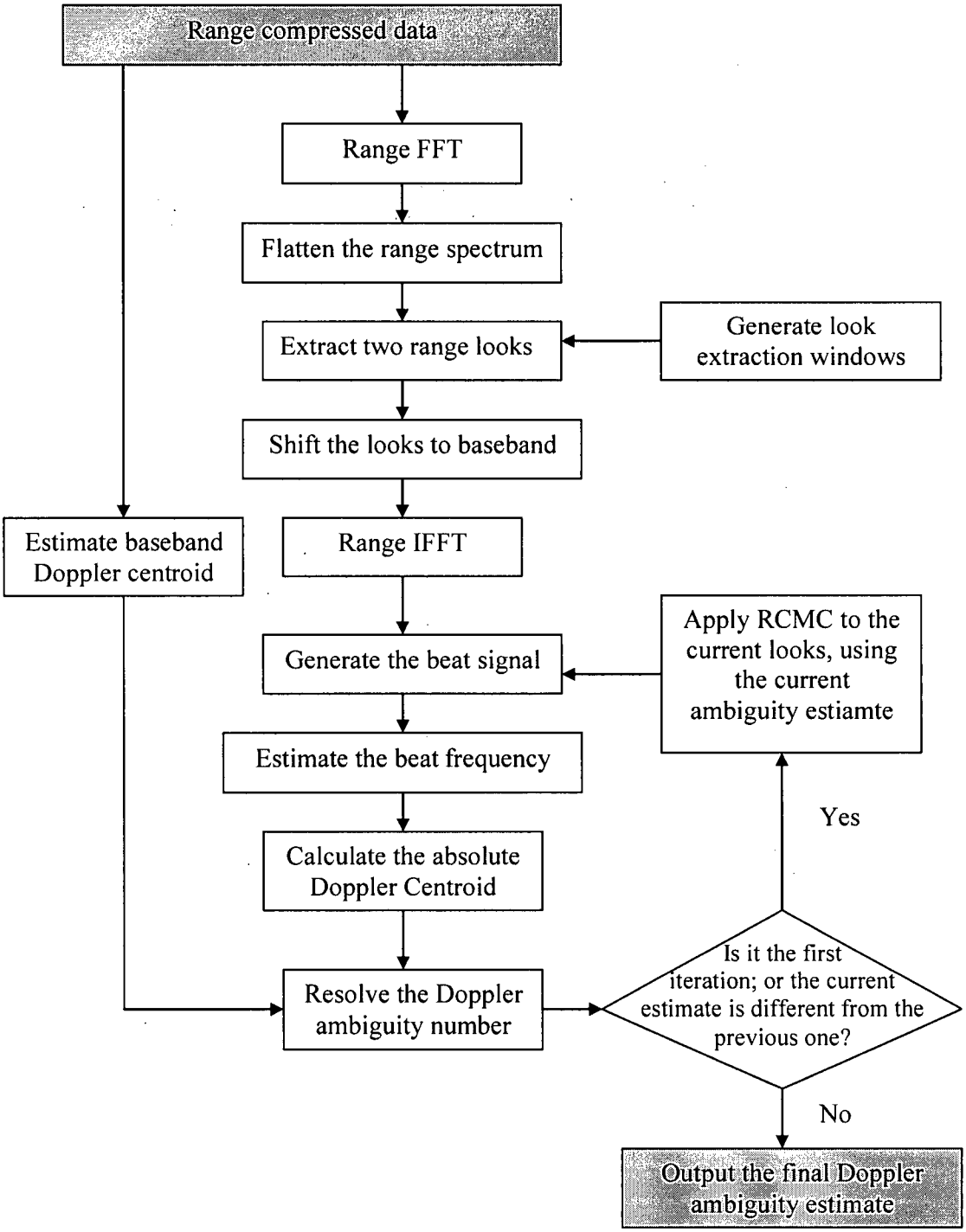

Figure 4-16 Flowchart of the proposed RCMC/MLBF algorithm

In the first iteration, since we don't yet know the absolute Doppler centroid, the conventional MLBF algorithm can be implemented without RCMC to obtain the initial

estimate. In some cases, an initial estimate of the Doppler centroid from geometry can be used in the first iteration. In subsequent iterations, RCMC can be applied using the current Doppler ambiguity estimate. As the RCMC is refined, the bandwidth of the beat signal is reduced, and lower bandwidth will benefit the ILP frequency estimator. The iterations continue until the Doppler ambiguity settles down to a stable value --- we have found that usually only two iterations are required with real data (see Section 4.4.2). Note that in this method, as in other ambiguity resolvers, the baseband Doppler estimates are obtained first and unwrapped so that a single Doppler ambiguity number applies over the whole scene.

As the iterative algorithm requires applying the RCMC and the MLBF algorithm more than once, the computation time is a little more than the standard MLBF algorithm. As the RCMC is applied after range look extraction, the look extraction is only applied once as the RCMC is changed. We have found that the extra computation load is acceptable, and the iterative MLBF computation only occupies a small portion of the whole SAR processing time.

4.4.2 Experimental results

In Section 4.3.4, the Vancouver "ships" and "mountains" scenes give two examples of how the iterative RCMC method can improve the sensitivity of the MLBF algorithm. In order to test its performance on different kinds of terrain in satellite SAR data, we apply them to real SAR data of RADARSAT-1 find mode Vancouver scene, as shown in Figure 4-10. In order to take advantage of spatial averaging and avoid bad estimates from areas with very weak backscatter, we make use of the concept of "spatial diversity" [19]. In this approach, the whole scene is divided into blocks, the estimators are applied and specific quality measurements are calculated for each block to exclude areas of the scene that are likely to lead to incorrect Doppler estimates. In this experiment, we divide the Vancouver data set into 12 range × 19 azimuth blocks, with each of the 228 blocks having 655 range cells and 1024 range lines. The block borders are outlined in the "range-compressed image" of Figure 4-17.

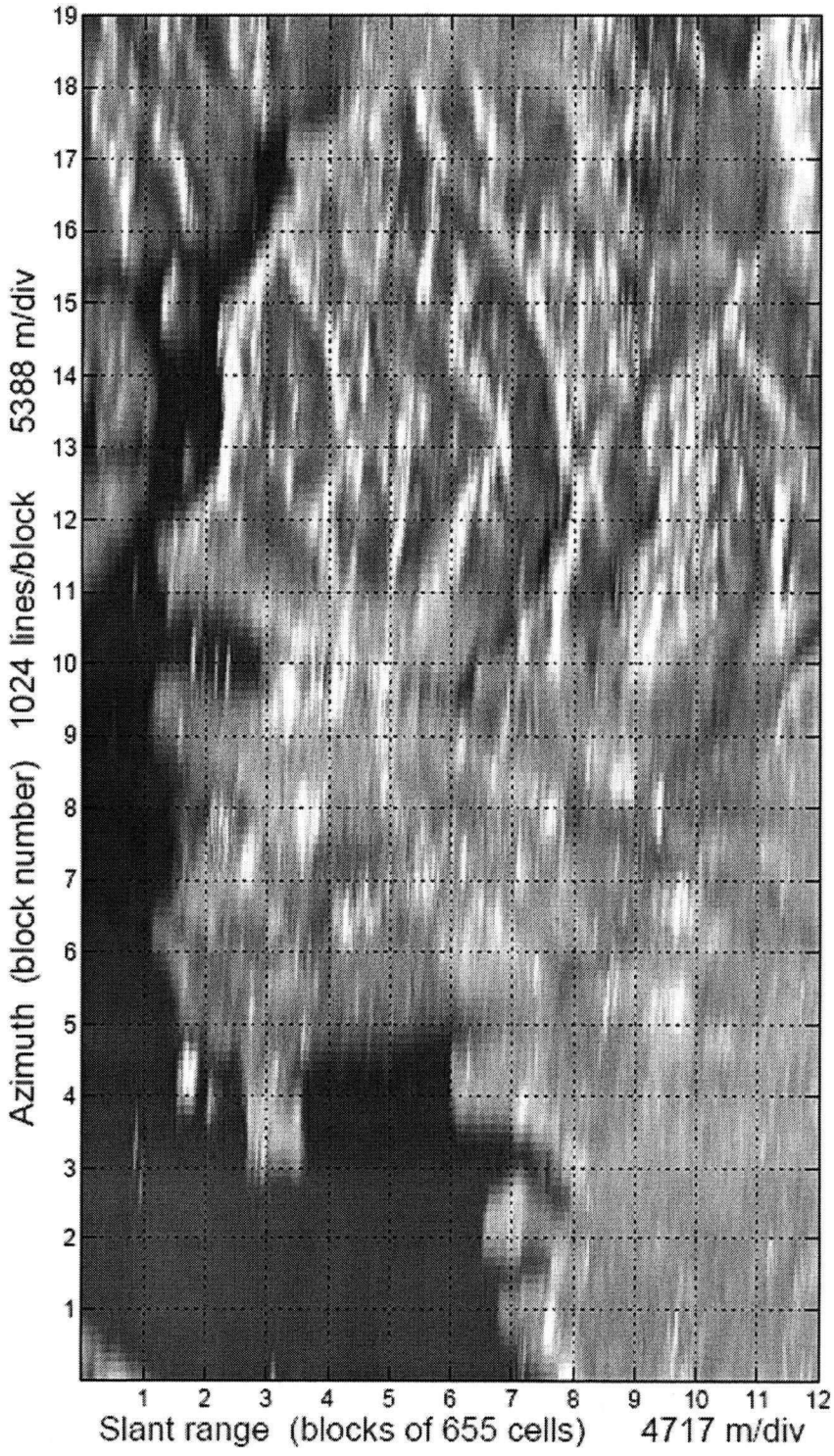

Figure 4-17 Range compressed image of Vancouver used in the Doppler estimation experiments [15]

Both the standard MLBF algorithm and the iterative MLBF algorithm using RCMC are implemented for each block. In this experiment, we use the frequency estimator based on the FFTs to estimate the beat frequency [13]. After processing all the blocks, the blocks with the possible bad estimates are removed using quality criteria. In order to compare the performances of all methods, the same quality criterion (the SNR of the range-compressed data larger than -1 dB) is applied in each case, so that the same blocks are removed. Then, a single Doppler ambiguity number is obtained for the whole scene using a "majority vote" or an average operation.

The iterative RCMC method shows an even better improvement. It has the highest success rate of all the estimators. Because the beat spectrum is cleaner after RCMC, the choice of frequency estimator is not so critical, and the simple FFT estimator works well.

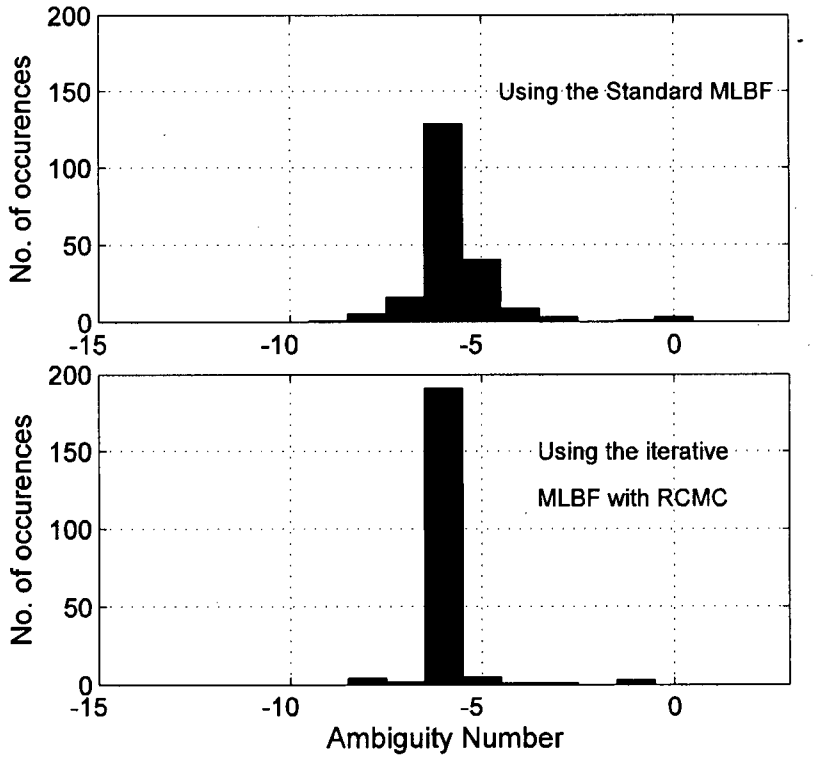

Figure 4-18 Histogram of the MLBF estimates of each block with and without RCMC

Table 4-1 Doppler Ambiguity estimates using Standard MLBF and the proposed method

Doppler Ambiguity estimators	Mean (PRFs)	St. Dev. (PRFs)	Success rate (%)
Standard MLBF	-5.74	1.09	62
Iterative MLBF using the RCMC	-5.92	0.73	92

The histogram and the comparison table show that the iterative MLBF using RCMC has a much better performance than the existing standard MLBF. The Standard deviation is reduced by about 30%, and the success rate increases considerably to 92%. In this experiment, most of the blocks that are taken as the good estimates only need two iterations. Only 2% blocks with good estimates need three iterations.

4.5 Summary

The MLBF algorithm is the one of the most reliable methods for Doppler ambiguity resolution. By examining the phase of the frequency-domain signal, we found that the azimuth phase variation caused by range migration plays an important role in the generation of the beat signal. We also presented the importance of having symmetrical range looks.

Then, we presented the method of applying RCMC to improve the sensitivity of the MLBF algorithm. The cross beating caused by multiple targets in a range cell introduces spurious signals into the spectrum of the beat signal. The presence of RCM reduces the exposure time in one range cell and thereby broadens the resolution of the beat signal. Then, we have shown how RCMC can alleviate these effects by increasing the resolution of the beat signal, and possibly reducing the cross beating. The analysis also shows that RCMC must be applied after the range look extraction, and that an iterative scheme must be used because the correct ambiguity is needed to perform RCMC

properly. Finally, experiments with RADARSAT-1 data are used to illustrate the improved estimation accuracy of the modified algorithm.

Chapter 5
Improved Beat Frequency Estimation in the MLBF algorithm

Among the Doppler ambiguity resolvers, the Multi-look Beat frequency (MLBF) algorithm proves to have good performance, especially in high contrast areas. It also avoids estimating the offset frequency, which is required in the WDA and MLCC algorithms. However, the existing MLBF algorithm has some problems. As it uses *FFT* operations to measure the central frequency of the beat signal by finding the maximum coefficient, it leads to quantization errors as only the energy at discrete frequencies is evaluated. In this method, the limited exposure in each range cell also reduces resolution of the spectrum. In addition, the algorithm using FFTs requires a zero-padding procedure when applied to burst mode data, such as ScanSAR data [13]. Therefore, more efficient and accurate methods are required to improve the performance of the MLBF algorithm

In this chapter, several frequency estimators are introduced to improve the beat frequency estimation in the MLBF algorithm. First, the center of gravity is used to measure the beat frequency from the beat signal spectrum. Then five established frequency estimators based on phase increments are applied to measure beat frequency from the phase information.

5.1 The Principle of the Beat Signal

As described in Chapter 3 and Chapter 4, the MLBF algorithm is based on the fact that the Doppler Centroid frequency can be derived from the azimuth phase difference between two looks that are extracted from the range spectrum. By multiplying

the signal of one look with the conjugate of the other look, a beat signal results, which can be expressed as [15]:

$$\begin{aligned} s_{beat}(\tau,\eta) &= s_{r1}^{*}(\tau,\eta)\, s_{r2}(\tau,\eta) \\ &= \left|A_1\, w_a(\eta-\eta_c)\right|^2 \exp\{-j\,4\,\pi\,\Delta f_r\, R(\eta)/c\} \end{aligned} \tag{5.1}$$

where $\Delta f_r = \Delta f_2 - \Delta f_1$. Δf_1 and Δf_2 are the central frequencies of the two range looks separately, assuming the two looks have symmetrical magnitude spectra.

To examine how the beat signal varies with azimuth time, we expand the slant range function $R(\eta)$ about the central illumined time η_c. If the small higher order components are ignored, the range between target and radar can be given by:

$$R(\eta) = R(\eta_c) - V_r \sin\theta_{r,c}(\eta-\eta_c) + \frac{1}{2}\frac{V_r^{\,2}\cos^2\theta_{r,c}}{R(\eta_c)}(\eta-\eta_c)^2 \tag{5.2}$$

where $\theta_{r,c}$ is the beam squint angle measured in the slant range plane

As the linear component, $-V_r \sin\theta_{r,c}(\eta-\eta_c)$, has a much larger value than the quadratic component, $\frac{1}{2}\frac{V_r^{\,2}\cos^2\theta_{r,c}}{R(\eta_c)}(\eta-\eta_c)$, the beat signal expressed by (5.2) mainly contains a single frequency with a narrow bandwidth.

According to the phase history of (5.1), Figure 5-1 shows the Azimuth frequency/time history of the beat signal. It can be seen that the beat signal has an average (central) frequency and a bandwidth.

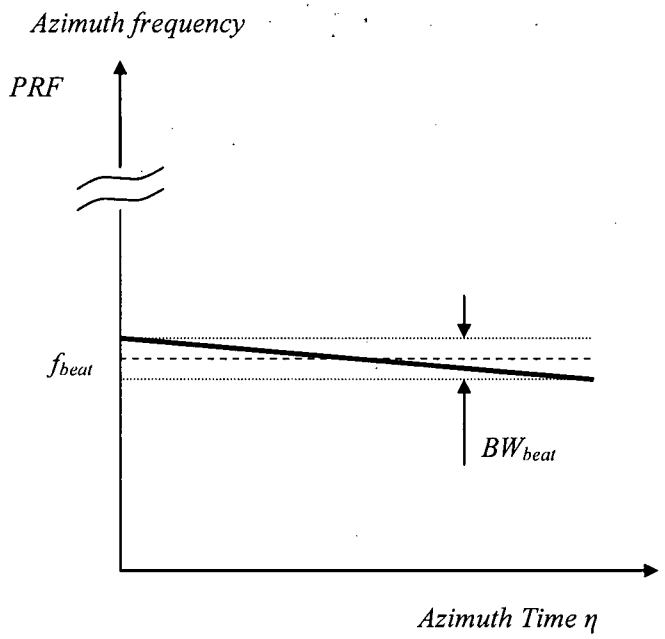

Figure 5-1 The frequency spread-out of the beat signal along azimuth

The central frequency of the beat signal, f_{beat}, can be derived from the phase of (5.1) and the linear component of (5.2), and is given by:

$$f_{beat} = -\frac{2\Delta f_r}{c}\frac{dR(\eta)}{d\eta} = \frac{2\Delta f_r V_r \sin\theta_{r,c}}{c} = \frac{\Delta f_r}{f_0} f_{\eta c} \tag{5.3}$$

where $f_{\eta c}$ is the Doppler Centroid frequency and $f_{\eta c} = -\frac{2 V_r \sin\theta_{r,c}}{\lambda}$.

Similarly, the bandwidth of the beat signal, BW_{beat}, can be derived from the phase of (5.1) and the quadratic component of (5.2), which is expressed as:

$$\begin{aligned} BW_{beat} &= -\frac{2\Delta f_r}{c}\frac{d^2R(\eta)}{d\eta^2} = -\frac{\Delta f_r V_r^{\,2}\cos^2\theta_{r,c}}{c\,R(\eta_c)} \\ &= -\frac{\Delta f_r}{f_0} BW_{azimuth} \end{aligned} \tag{5.4}$$

where $BW_{azimuth}$ is the azimuth bandwidth of the received signal and $BW_{azimuth} = \frac{V_r^{\,2}\cos^2\theta_{r,c}}{\lambda\,R(\eta_c)}$.

Both the center frequency, f_{beat}, and the bandwidth, BW_{beat}, of the beat signal are quite small compared to the system PRF. Taking the RADARSAT-1 Vancouver scene data as an example, where $f_{\eta c} \approx$ -5900Hz, f_{beat} is about 21 Hz, the predicted BW_{beat} is about 2.5 Hz, while the PRF is 1275 Hz, as shown in Figure 5-1. The small value of f_{beat} compared to the PRF avoids unwrapping and makes this algorithm suitable for Doppler ambiguity estimation. (The ambiguity error limits are +/- 3.5 Hz in this case.) The narrow bandwidth, BW_{beat}, justifies that the beat signal can be approximated by a single frequency with noise.

As the beat frequency is proportional to the absolute Doppler centroid in (5.3), the absolute Doppler centroid frequency can be estimated from the measurement of the beat frequency, which can be expressed as:

$$f_{\eta c} = -\frac{f_0}{\Delta f_r} f_{beat} \tag{5.5}$$

The above analysis is based on the existence of a single target in each range cell without noise. However, in implementation noises are usually inevitable. In addition, when there is more than one target, cross beating exists, which lowers the SNR of the beat signal and makes it harder to estimate the beat frequency accurately [15].

5.2 Single Frequency Estimation

As discussed in Section 5.1, the beat signal can be approximated to a single frequency signal with noise. Therefore, single frequency estimators can be applied to the estimation of the beat frequency. In this section, the model for single frequency estimation is established and analyzed. Then, the survey results give several single frequency estimators and each estimator is described separately.

5.2.1 Introduction

The problem of estimating the frequency of a complex exponential in additive white noise is a fundamental and well-studied problem in estimation theory. In particular, consider the N-point received data to consist of a single complex sinusoid in complex white Gaussian noise, which has the form of:

$$x(n) = A\exp\{j(\omega n + \varphi)\} + z(n), \qquad (5.6)$$
$$n = 0,\quad 1,\quad 2,\quad \ldots,\quad N-1$$

where $\omega, -\pi \le \omega < \pi$, is the frequency in radians/sample, and A and φ, $-\pi \le \varphi < \pi$ are unknown constants. The noise z is a zero-mean complex white Gaussian process with: $z(n) = z_r(n) + jz_i(n)$. Its components $z_r(n)$ and $z_i(n)$ are real, uncorrelated, zero-mean Gaussian random variables with variance $\sigma^2/2$ (σ^2 is the variance of $z(n)$ from the calculation of $E[(z(n) - E(z(n)))(z(n) - E(z(n)))^*]$.)

According to estimation theory, the ultimate accuracy bound for frequency estimation is derived from the Cramer-Rao inequality, which is called the Cramer-Rao Bound. The Cramer-Rao Bound can be calculated as [27]:

$$CRB = \frac{6}{SNR\,N\,(N^2-1)} = \frac{6}{\frac{A^2}{\sigma^2}N\,(N^2-1)} \qquad (5.7)$$

where SNR is the Signal to Noise Ratio, and N is the length of the signal array.

As illustrated in Figure 5-2, our survey results show that the frequency estimators can be classified into two categories: algorithms based on *FFTs* and algorithms based on phase increments. In the following sections, we will be discussing seven frequency estimators. The methods based on *FFTs* include measuring the frequency of the maximum *FFT* coefficient and measuring the Center of Gravity. The methods based on phase increments include Kay's estimator, ACCC estimator, FCFB estimator, HLC estimator and ILP estimator. The contents and the organization of the following subsections are shown in Figure 5-2.

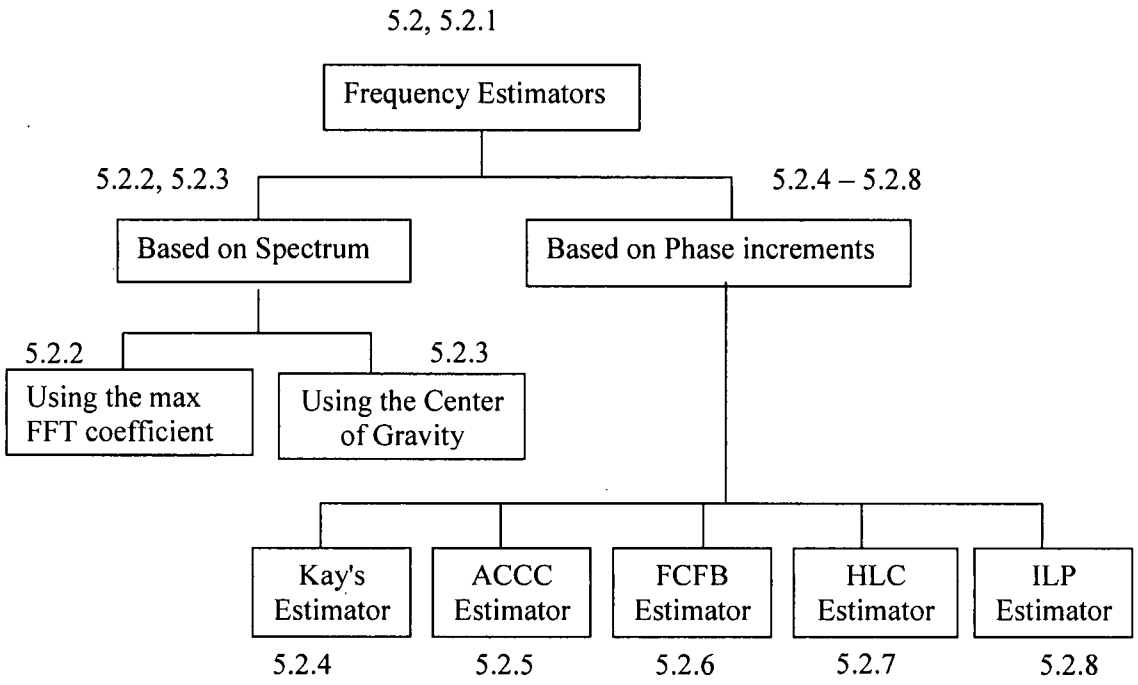

Figure 5-2 The outline of frequency estimators

5.2.2 Estimator based on the maximum FFT coefficient

The frequency estimator using *FFT* operations is based on Maximum likelihood estimation (MLE) of a single frequency, which was studied by Rife and Boorstyn in [27]. The MLE can be derived from the periodogram, which is given by:

$$\hat{\omega} = \arg\max_{\omega'} \left| \sum_{n=0}^{N-1} x(n) \exp\{-j\omega' n\} \right|^2 \tag{5.8}$$

where $\hat{\omega}$ is the estimated frequency of MLE and the argmax returns the value of the element noted below that makes the function attain the maximum value, which is different to the function 'arg' as used later.

Equation (5.8) is expressed as a continuous function of frequency ω'. For calculation efficiency, it is rewritten at a set of discrete frequencies and the FF*T* algorithm can be used to obtain the periodogram. The estimation equation is given by [27]:

$$\hat{\omega} = \frac{2\pi}{N_{FFT}} \arg\max_{0 \le m < N_{FFT}-1} \left| \sum_{n=0}^{N_{FFT}-1} x(n) \exp\{-j(2\pi m n / N_{FFT})\} \right|^2 \tag{5.9}$$

where N_{FFT} is the FFT length.

It is straight-forward from equation (5.9) that the frequency can be estimated by finding the discrete frequency that corresponds to the maximum FFT coefficient. The existing MLBF algorithm uses such method in the beat frequency estimation. However, this method leads to quantization error because it only evaluates the energy at discrete frequencies. In this case, the maximum quantization error is given by:

$$\Delta f_{\eta c} = \left| \frac{f_0}{\Delta f_r} f_{FFT-scale} \right| = \left| \frac{f_0}{\Delta f_r} \frac{1}{2} \frac{PRF}{N_{FFT}} \right| \tag{5.10}$$

In the implementation of RADARSAT-1 dataset, if we apply a 1024-point FFT and separate the two range looks by about half of the range spectrum bandwidth, the maximum quantization error is about 100 Hz. Since the existence of the quantization error restricts the accuracy of the estimator even at high SNR, more accurate frequency estimators are required to improve the beat frequency estimation.

5.2.3 Estimator based on the "center of gravity"

Since the frequency of the signal corresponds to the peak center of the signal spectrum, we can measure the frequency by finding the *"center of gravity"* in the spectrum of the beat signal in order to reduce the effects of the quantization errors and other addictive errors [29]. Similar to Section 5.2.2, we use *FFTs* to obtain the spectrum of the signal. Then, the single frequency can be estimated by this method using:

$$\hat{\omega} = \frac{\sum_{i=1}^{N} \omega_i \, FS_i}{\sum_{i=1}^{N} FS_i} \tag{5.11}$$

where $\hat{\omega}$ is the estimated frequency from the "*center of gravity*", ω_i is the discrete frequency of each FFT cell, and FS_i is voltage of the signal spectrum (i.e. *FFT* coefficient) at ω_i. As illustrated in Figure 5-3, this method is equivalent to finding the frequency, $\hat{\omega}$, that balances the integral of the shaded areas, I_1 and I_2, when the integral is taken to the left and to the right of the estimated frequency. This estimated frequency can be a value between two discrete frequencies, and therefore the quantization errors are reduced. In addition, when the spectrum curve obtained from *FFTs* is not symmetrical due to other noise, the center of gravity is a more accurate estimate than the position of the maximum value.

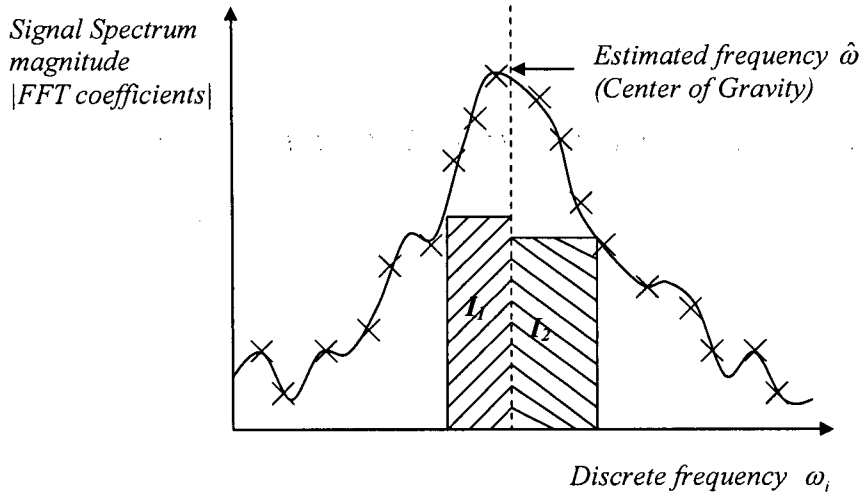

Figure 5-3 Center of gravity in signal spectrum

However, the frequency estimator based on the centre of gravity still has some limitations. Since it is also based on *FFT* operations, the estimation accuracy is still related to the *FFT* length. In addition, the *FFT* operations cannot be applied to ScanSAR processing directly due to the gaps between the two burst.

5.2.4 Kay's estimator

The frequency estimators based on phase increments can avoid the problems and limitations of the estimators based on the *FFT* operations. Kay's estimator (proposed by Steven Kay in 1989 [30]) is the basic single frequency estimator that uses phase increments instead of the periodogram to estimate the signal frequency. If we assume that the SNR, which is A^2/σ^2, is large, the data model of (5.6) can be rewritten by replacing additive noise by phase noise, which is given by:

$$x(n) \approx A \exp\left(j\,(\omega n + \varphi + u(n)\,\right) \qquad (5.12)$$

$$n = 0, 1, 2, \cdots, N-1$$

where $u(n)$ is zero mean white Gaussian phase noise with variance $\sigma^2/2A^2$.

Therefore, the phase of the signal can be written as:

$$\arg(\,x(n)\,) = \omega n + \varphi + u(n) \qquad (5.13)$$

where arg returns the argument (phase) of a complex number.

The differenced phase data can be given as:

$$\Delta\arg(\,x(n)\,) = \arg(\,x(n+1)\,) - \arg(\,x(n)\,) \qquad (5.14)$$

The formula can be simplified as:

$$\Delta\arg(\,x(n)\,) = \omega + u(n+1) - u(n) \qquad (5.15)$$

The problem now is to estimate ω from a process with colored Gaussian noise, $u(n+1) - u(n)$. The MLE of ω is equivalent to the minimum variance unbiased estimator. After some algebra, the estimate based on the weighted phase average is obtained as:

$$\hat{\omega} = \sum_{n=0}^{N-2} w(n)\,\Delta\arg(\,x(n)\,) \qquad (5.16)$$

where $w(n)$ is the weighting function that guarantees that the estimator attains the Cramer-Rao Bound. It has the parabolic form [30]:

$$w(n) = \frac{\frac{3}{2}N}{N^2 - 1}\left\{1 - \left[\frac{n - \left(\frac{N}{2} - 1\right)}{\frac{N}{2}}\right]^2\right\} \tag{5.17}$$

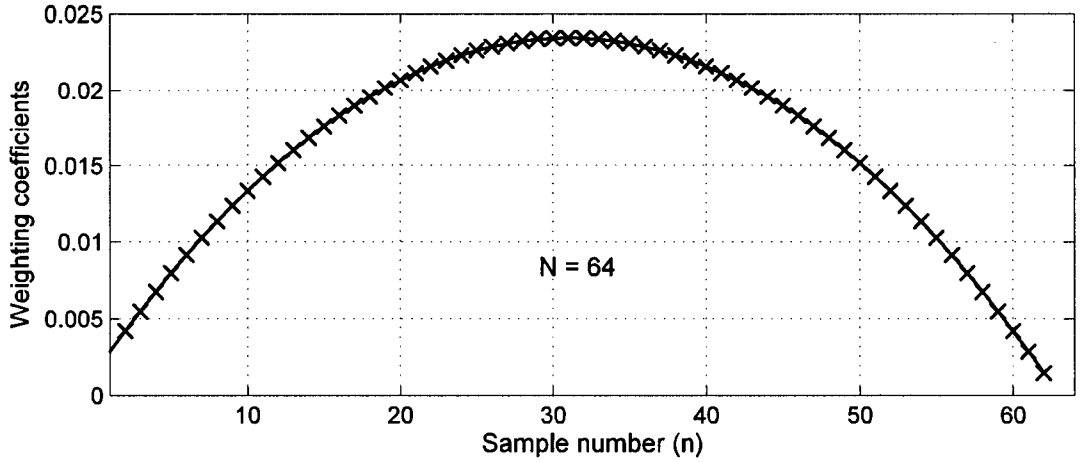

Figure 5-4 Weighting function of Kay's estimator

Figure 5-4 shows the weighting function of Kay's estimator for a 64-point signal. The weighting is used to recognize the fact that the middle part of the array contains more information of the frequency than the edges.

In addition, Kay also proposed four options in [30], which include weighted linear predictor, unweighted linear predictor, weighted phase averager and unweighted phase averager. The difference between linear predictor and phase average is the exchanged operations of taking the summation and the angle. Since arg is non-linear operation, when it is interchanged with the sum operation, a different result is obtained.

5.2.5 ACCC estimator

In the linear predictor option of Kay's estimator, the frequency estimator may further be written by using the equivalence:

$$\begin{aligned}\Delta\arg(x(n)) &= \arg(\,x(n+1)\,) - \arg(\,x(n)\,) \\ &= \arg(x^{*}(n)\,x(n+1)\,)\end{aligned} \tag{5.18}$$

Therefore, the calculation of the phase increment is equivalent to the calculation of the Cross Correlation Coefficients (CCC) at lag one. For simplification, if we ignore the colored noise in (5.15), the estimator then is to calculate the average cross correlation coefficients (ACCC) as:

$$\hat{\omega} = \arg\left(\frac{1}{N-1}\sum_{n=0}^{N-2} x^{*}(n)\,x(n+1)\right) \tag{5.19}$$

It is worth noting is that the use of the CCC in Baseband Doppler Centroid Estimation was proposed by Soren Madsen in 1989 [8], the same year in which Kay proposed his estimator. In that algorithm, the Baseband Doppler Centroid is measured using the average of CCC (ACCC) along the azimuth lines. In order to reduce the effect of noise, the estimate results can be further averaged along range cells. Because the CCC is a complex number and we implement the average before taking the argument operation in the complex domain, the results of ACCC algorithm are weighted by the magnitude of the CCC vectors.

It is concluded in [30] that the original Kay's estimator using the weighted phase average gets closer to the Cramer-Rao Bound than ACCC estimator at high SNR. However, the accuracy of both estimators decreases dramatically when the SNR is below some value. Such a SNR value is called the "SNR threshold" and the SNR threshold can be used to evaluate the performance of the frequency estimators. The lower the SNR threshold is, the better results the frequency estimator can get under noisy conditions.

5.2.6 Four channel filter banking (FCFB) estimator

Since Kay's estimator and ACCC estimator may suffer from a relatively high SNR threshold, the idea of applying a filter to enhance the SNR is brought out in the four channel filter banking (FCFB) method [31] proposed by M. Fowler and J. Johnson in

1999. In this method we apply four simple filters to overlapping frequency bands that cover $(-\pi, \pi]$, as shown in Figure 5-5. The four channel filters work as band pass filters, which let the signal pass through while remove the noise outside the pass band. Then we detect which band the frequency lies in by comparing the energy in the four channels. The output signal with the highest energy is then processed using the ACCC estimator. Finally, the estimate result is adjusted to achieve the correct answer according to which channel is used.

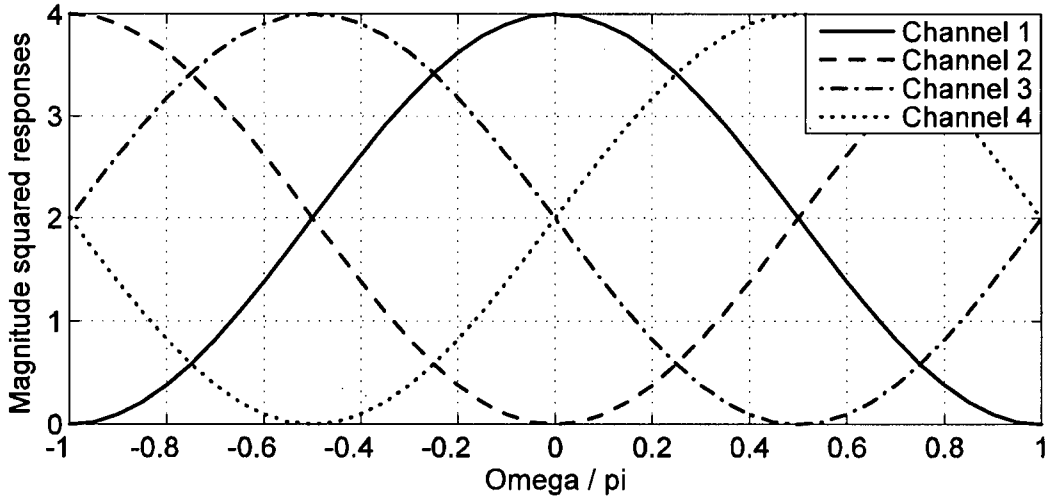

Figure 5-5 Four channel filters in FCFB estimator

The steps of the algorithm are given as following:

1) Digitally heterodyne $x(n)$ with $\exp\{-j(\pi/2)n\}$, $\exp\{-j\,0\,n\}$, $\exp\{j(\pi/2)n\}$, and $\exp\{j\,\pi\,n\}$, respectively to generate $x_1(n)$, $x_2(n)$, $x_3(n)$, and $x_4(n)$.
2) Filter and decimate these signals to get $\tilde{a}_i(n) = x_i(2n-1) + x_i(2n)$, for $n = 1, 2, \ldots, N/2-1$;
3) Calculate the detection statistic as $\Gamma_i = \left| \sum_{n=1}^{(N/2)-1} \tilde{a}_i(n+1)\ \tilde{a}_i^*(n) \right|, \quad i = 1, 2, 3, 4$
4) Select $\tilde{a}_m(n)$ to be the signal whose detection statistic $\Gamma_m = \max\{\Gamma_1, \Gamma_2, \Gamma_3, \Gamma_4\}$; if two Γ_i's equal the maximum, either can be chosen;

5) Compute the fine estimate using the formula (5.19) and adjust it by $\hat{\omega} = \left\lfloor \hat{\omega}_f + (m-2)\pi/2 \right\rfloor_{\bmod 2\pi}$, where m is the number of the channel used.

Since this estimator only adds very simple filters into the basic ACCC estimator, its computational complexity is acceptable. The experimental results show that this estimator can improve the SNR threshold of the basic Kay's and ACCC estimator to some extent, but the improvement is not significant [33] .

5.2.7 Higher lag correlation (HLC) estimator

Another method for improving the basic Kay's and ACCC estimators, proposed by Michael P. Fitz [32] in 1994, is to use the correlation at higher lag instead of only the correlation at lag one in the estimation. The correlation at higher lag can provide extra information of the angle and therefore improve the accuracy of the estimator.

$$\begin{aligned} \arg\left(x^*(n)\, x(n+m)\right) &= \arg\left(x(n+m)\right) - \arg\left(x(n)\right) \\ &= m\, \Delta \arg(x(n)) + Noise \end{aligned} \tag{5.20}$$

where $x^*(n)\, x(n+m)$ is one term in the correlation calculation at lag m. It can be seen from (5.20) that the angle of the correlation at higher lag can be written as the accumulations of the angles of the correlation at lag one with noise.

The high lag correlation estimator is derived by taking the derivative of the periodogram w. r. t. (with respect to) ω' as shown in (5.8), and then set it equal to zero. After grouping terms, the likelihood equation can be expressed as [32] :

$$L_{\omega'}(m) = \mathrm{Im}\left[\sum_{m=1}^{N} m\, \hat{R}_N(m) \exp(-j\omega' m)\right] = 0 \tag{5.21}$$

where $\hat{R}_N(m)$ is the correlation at high lag. And it can be expressed by:

$$\hat{R}_N(m) = \sum_{n=m+1}^{N} x(n)\, x^*(n-m) \tag{5.22}$$

With large N, (5.21) can be approximated as:

$$\sum_{m=1}^{N} m\left[\arg\left(\hat{R}(m)\right) - m\,\omega'\right] \approx 0 \tag{5.23}$$

And the estimator can be derived as:

$$\hat{\omega} = \sum_{m=1}^{N} \frac{6m}{N(N+1)(2N+1)} \arg\left\{\hat{R}_N(m)\right\} \tag{5.24}$$

With the increase of N, the computation amount increases dramatically. Therefore, the summation in (5.24) is truncated at indices $M = J$, where J is much less than N. A more practical estimator has the form as:

$$\hat{\omega} = \frac{\sum_{m=1}^{J} m \arg\left\{\hat{R}_N(m)\right\}}{\sum_{m=1}^{J} m^2} \tag{5.25}$$

In the selection of J, there is a trade-off between accuracy and computation complexity. When an optimal value of J is selected, this method is computationally efficient yet obtains near optimum performance at moderate SNR.

5.2.8 Iterative linear prediction (ILP) estimator

A more accurate estimator is proposed by Tyler Brown in 2002 [33], called the iterative linear prediction (ILP) method. This method takes advantages of iteration processing and low-pass filtering to improve the basic Kay's and ACCC estimators.

In this algorithm, the coarse estimate of the frequency is first obtained by ACCC estimator. Then the original signal is shifted to a lower band, according to the initial frequency estimate, and then low pass filtered with a rectangular filter with coefficients $h_i = 1$, i = 0, 1, 2, ..., M -1. (We found that using the *sinc* filter instead of the rectangular filter can get better results.) The low pass filter reduces the out-of-band noise and enhances the SNR. Therefore, by applying ACCC estimator again, the estimated frequency error can be obtained with a better accuracy than the initial estimate. After that,

the coarse frequency estimate is corrected by the estimated frequency error and the next iteration starts by shifting the original signal with the corrected frequency estimate. After each iteration, the bandwidth of the low-pass filter is reduced by two. In this way, the SNR is enhanced by a narrower filter bandwidth, which improves the estimation accuracy. Therefore, by iteratively applying the ACCC estimator, the procedure can reduce the error of the estimated frequency at each iteration. The iterative procedure can be ended when there is no significant improvements detected or the bandwidth of the low pass filter is smaller than the bandwidth of the beat signal.

The iterative calculation and frequency estimate at iteration k are given by:

$$\tilde{x}_k(n) = \exp(-j\hat{\omega}_{k-1} n)\, x(n) \tag{5.26}$$

$$v_k(n) = \sum_{m=0}^{M_k-1} \tilde{x}_k(M_k n + m), \quad n = 0\ ,\ 1\ ,\ \ldots\ ,\ \frac{N}{M_k - 1} \tag{5.27}$$

$$\Delta\hat{\omega}_k = \frac{1}{M_k} \arg\left[\sum_{n=1}^{N/M_k-1} v^*_k(n-1)\, v_k(n) \right] \tag{5.28}$$

$$\hat{\omega}_k = \left(\Delta\hat{\omega}_k + \hat{\omega}_{k-1}\right)_{-\pi}^{\pi} \tag{5.29}$$

where $\hat{\omega}_0$ is the initial estimate of the basic Kay's estimator, $v_k(n)$ is the signal after low-pass filtering, $\Delta\hat{\omega}_k$ is the estimated frequency error in the current iteration, and $\hat{\omega}_k$ is the corrected frequency estimate in the current iteration.

As the analysis above, the ILP estimator improve the performance of the basic estimators by iteratively applying low-pass filters. As the bandwidth of the low-pass filter is reduced at each iteration, the frequency estimate is getting more and more accurate. Consequently, the ILP estimator has the best performance among the survey results of frequency estimators.

5.2.9 Simulations of single frequency estimators

To test and compare the performance of the discussed frequency estimators, we simulate a single frequency signal with white noise and use these estimators to measure the frequency separately. In this experiment, we use Mean Square Error (MSE) as the accuracy measurement. The MSE is defined as the average of the square of the difference between the estimated frequency and the actual frequency, which can be calculated as: which is defined as

$$MSE(\omega) = \sqrt{E\left[(\hat{\omega} - \omega_{true})^2\right]} \tag{5.30}$$

where $E[\ ]$ is the calculation of expectation, $\hat{\omega}$ is the estimated frequency, and ω_{true} is the true frequency.

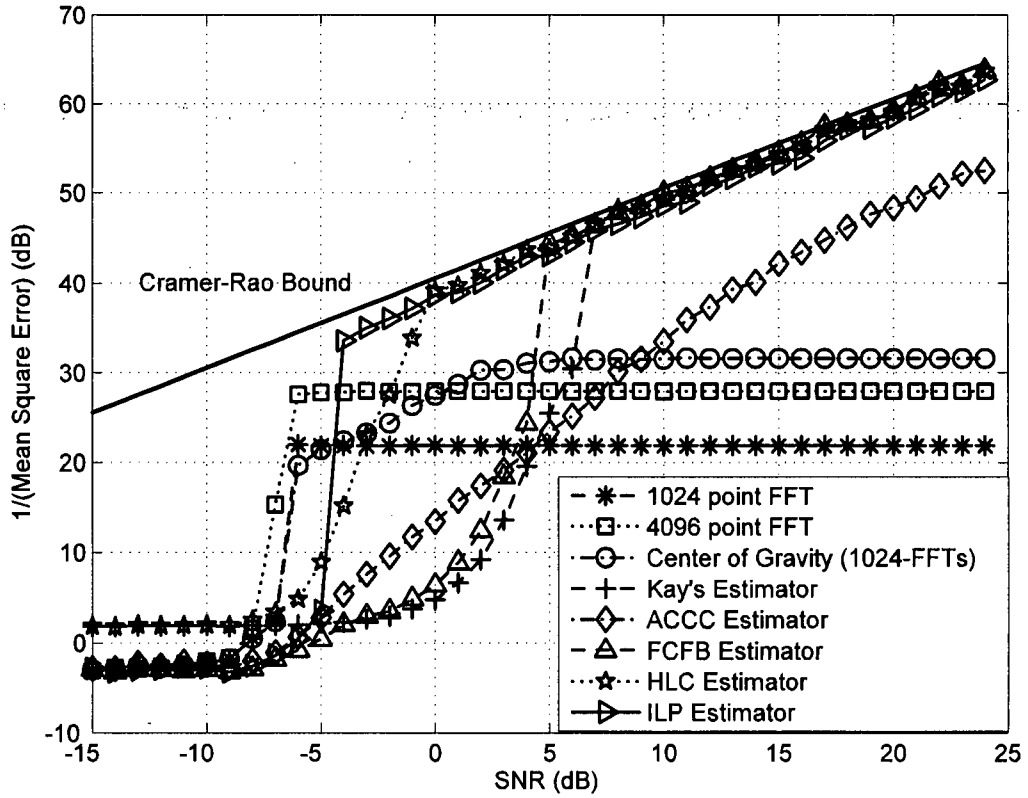

Figure 5-6 Comparison of single frequency estimators

Figure 5-6 shows the estimation results of all the frequency estimators for comparison. In Figure 5-6, it can be seen that all the estimators suffer from the SNR threshold. As we discussed before, the SNR threshold is defined as the SNR value, below which the estimate accuracy decreases dramatically. As illustrated in the figure, the SNR threshold of the ILP estimator is about -4 dB; the SNR thresholds of the FFTs estimators (including the estimator using Center of Gravity) are about -7 dB despite of the FFTs length; the SNR threshold of the FCFB estimator is about 6 dB; and the SNR threshold of the High Lag Correlation estimator is about 0 dB. In addition, the ACCC estimator does not appear to exhibit a sharp SNR threshold but gradually deteriorates in performance with decreasing SNR. The results show that the estimation algorithms based on periodogram have a relatively lower SNR threshold. Moreover, the estimation error of the estimator using the maximum FFT coefficient keeps constant beyond the SNR threshold due to the quantization errors. Even using the Center of Gravity, the estimate results of the FFT methods still cannot get an approach to the Cramer-Rao Bound as close as the algorithms based on phase increments. Considering the closeness to the Cramer-Rao Bound as well as the SNR threshold, we can come to the conclusion that the ILP estimator is the best algorithm for the single frequency estimation problem among all the estimators in this study.

5.3 The Beat Frequency Estimation

As discussed in Section 5.1, the beat signal can be approximated by a single-frequency narrow-band signal. Therefore, the frequency estimators discussed in Section 5.1 can be applied to the beat frequency estimation. However, as the existence of noise, the bandwidth, and the cross beating, the accuracy of the beat frequency estimation is not as good as in the ideal condition.

5.3.1 The application of the frequency estimators

If we use the beat frequency, f_{beat} in (5.2), to substitute the linear term in (5.1), and ignore the quadratic term, the beat signal with additive noise can be expressed in discrete time as:

$$s_{beat}(n) \approx A(n)\exp\left(j2\pi \frac{f_{beat}}{PRF} n\right) + z(n) \qquad n = 0, 1, 2, \ldots, N-1 \tag{5.31}$$

where n is the azimuth time index, $A(n)$ is the azimuth envelope, and $z(n)$ is the complex noise with variance σ^2.

So, comparing the beat signal in discrete time (5.31) to the single frequency signal model (5.6), the frequency estimators can be applied directly to the beat signal. Using the basic Kay's estimator, the estimated beat frequency has the similar form as in (5.16) , which is given by:

$$\hat{f}_{beat} = \frac{PRF}{2\pi} \sum_{n=0}^{N-2} w(n)\, \Delta \arg\{s_{beat}(n)\} \tag{5.32}$$

where $w(n)$ is the same weighting function as in (5.17).

Similarly, other phase-based frequency estimators can be applied to the beat frequency estimation. In those estimators, the ILP estimator is expected to have the best performance. The estimated beat frequency using the ILP estimator can be obtained by the following calculation:

$$\hat{f}_{beat}^{(k)} = \Delta \hat{f}_{beat}^{(k)} + \hat{f}_{beat}^{(k-1)} \tag{5.33}$$

where $\hat{f}_{beat}^{(0)}$ is the initial estimate of the basic Kay's estimator, $\Delta \hat{f}_{beat}^{(k)}$ is the estimated frequency error in the current iteration, and $\hat{f}_{beat}^{(k)}$ is the frequency estimate in the current iteration after correction.

With the estimate of the beat frequency, the absolute Doppler centroid frequency and the Doppler ambiguity can be obtained using the same procedure as in the existing MLBF algorithm, described in Chapter 3.

5.3.2 Quality criteria

In order to avoid corruption by bad estimates from the areas with very weak backscatter or low contrast, quality criteria can be used to detect and remove bad estimates from the final absolute Doppler estimate, when the "spatial diversity" approach [19] is used. In addition to the data quality criteria of SNR and contrast used in [19], two other estimator quality criteria that are specific to the operation of the beat frequency estimators were examined:

Peak to Mean Ratio (PMR)

In the frequency estimators based on *FFTs*, the periodogram can be checked for quality. A good periodogram with a sharp and clear peak would give a good frequency estimate. Therefore, by checking the shape of the periodogram, we can obtain the measurement of how good the frequency estimate could be. A quality criterion "Peak to Mean Ratio (PMR)" is introduced for this purpose. As shown in Figure 5-7, the Peak to Mean Ratio is defined as the ratio between the global peak and the mean value of the non-peak area in the periodogram. The peak area is the area within the 10 dB bandwidth downward from the peak of the main lobe, and the non-peak area is the remaining area other than the peak area. This ratio is usually expressed in dB units, and is given by:

$$PMR = 20 \log\left(\frac{Peak_{global}}{Mean_{non-peak}} \right) \tag{5.34}$$

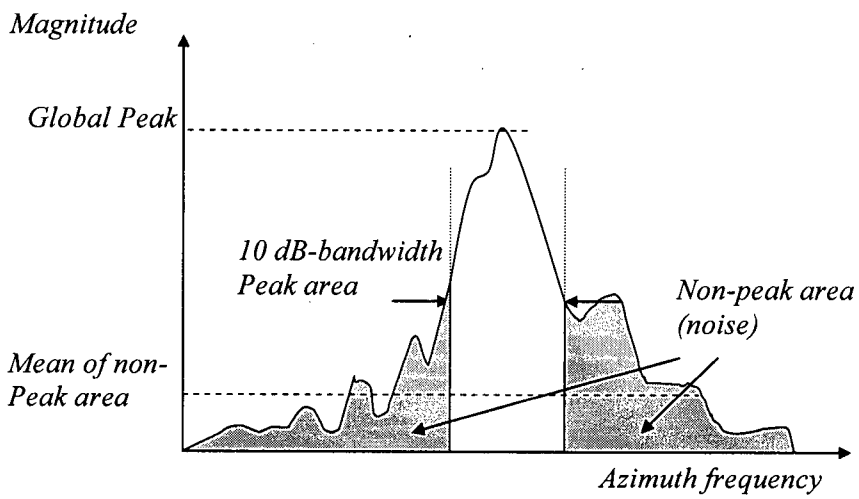

Figure 5-7 Measurement of PMR

Phase Coherence

In the estimators based on phase increments, the more consistent the phase increments are, the better estimates can be obtained. Hence, in this case the phase coherence is found to be the most appropriate quality measurement [34]. The phase coherence measures the consistency of the phase increments of the beat signal. It is defined as the ratio between the absolute value of the summation and the summation of the absolute value of the vectors that contains the phase increments, and can be expressed as:

$$Ph\_coher = \frac{\left|\sum_{n=0}^{N-2} s^{*}_{beat}(n)\, s_{beat}(n+1)\right|}{\sum_{n=0}^{N-2} \left|s^{*}_{beat}(n)\, s_{beat}(n+1)\right|} \tag{5.35}$$

where $s_{beat}^{*}(n)\, s_{beat}(n+1)$ is the correlation of the beat signal, whose phase is the phase increments of the beat signal.

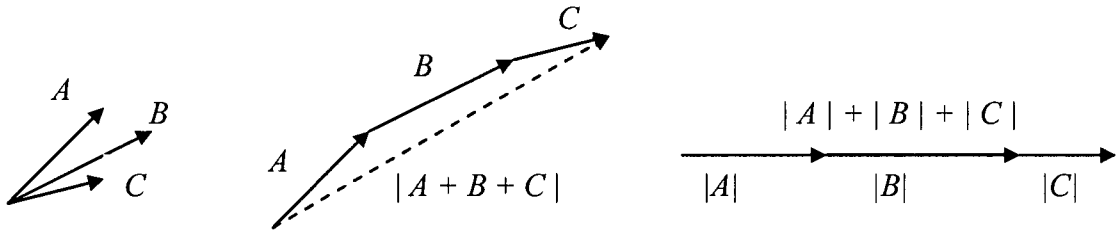

Figure 5-8 Illustration of the measurement for phase coherence

As illustrated in Figure 5-8, the absolute value of the summation of three complex vectors is always less than or equal to the summation of their absolute values. The closer the phases of the three vectors, the larger value the first operation would obtain. These two operations can obtain equal values only when the phases of the vectors are the same. In this sense, the ratio between these two values indicates how consistent the phases of the vectors are. Consequently, the defined quality criterion, phase coherence, is within the range from 0 to 1. The value reaches its maximum value 1 only when the beat signal is a pure tone without noise. A larger value of this measurement corresponds to a better beat signal for estimation and thus a better Doppler estimate.

5.4 Experiments on Real SAR Data

To examine how the estimators behave with general scenes of Satellite SAR data, the RADARSAT-1 fine mode scene of Vancouver, the same as shown in Figure 4-10, is selected. In addition, the "spatial diversity" approach [19] is applied and the same block separation scheme is taken as what was done in Figure 4-17.

In Doppler Centroid estimation procedure, the proposed estimators are applied into each block, and the quality criteria are measured as well. For comparison, we also test the performance of the existing standard MLCC algorithm and standard MLBF algorithm.

5.1.1 Examining the quality criteria

In this experiment, SNR, PMR of the periodogram and the phase coherence are measured as the quality criteria of the estimators to remove the possible bad estimates. For the Vancouver scene, the true Doppler ambiguity number is -6. So the good quality criteria should keep the blocks with correct Doppler ambiguity estimates and remove the blocks with incorrect Doppler ambiguity estimates as many as possible.

Table 5-1 Examining quality criteria with MLBF using ILP estimator

Quality Criteria	Number of blocks with Good estimate	Number of blocks with Bad estimate
SNR > -2.8 dB	172	30
SNR < -2.8 dB	7	19
PMR > 1.5 dB	170	30
PMR < 1.5 dB	9	19
Phase Coherence > 0.17	175	30
Phase Coherence < 0.17	4	19

Table 5-1 shows how the quality criteria behave in recognizing the blocks with good estimates from those with the bad estimates. It can be seen that a threshold can be chosen that does a reasonable job of separating those blocks that yield good estimates from those blocks that give bad estimates. In this experiment, we adjust the thresholds so the number of blocks excluded is the same for each criterion. From the result, it can be seen that the quality criterion of the phase coherence with a threshold at 0.17 shows the best performance in rejecting the possible bad estimates while keeping the good estimates. In this case, 21 blocks out of total 228 blocks (about 10%) are rejected.

5.4.1 Results of Doppler ambiguity estimates

After removing the possible bad estimates, the final Doppler ambiguity estimate can be obtained by an average or "majority vote" operation. The estimate results of all the estimators within the remaining 207 blocks are listed in Table 5-2. In this table, the ambiguity error before rounding, the standard deviation, and the success rate of the correct estimates are considered as the measurements of the estimator's performance. We consider the standard deviation as the best parameter to evaluate the estimator because it shows how the estimate results disperse around the true value and it's the most direct measurement of the randomness of the estimator. In addition, it is worth noting that since there are many bright isolated targets in the Vancouver scene, the estimate results of MLBF algorithm are much better than those of MLCC algorithm.

Table 5-2 Comparison of Doppler ambiguity resolvers for the Vancouver data

Doppler Ambiguity Resolvers	Mean (PRFs)	St. Dev. (PRFs)	Success rate (%)
Standard MLCC	-5.99	1.36	41
Standard MLBF	-5.72	1.09	62
MLBF using Center of Gravity	-5.75	0.92	69
MLBF using Kay's	-5.95	0.92	55
MLBF using ACCC	-6.02	0.90	57
MLBF using HLC	-5.94	0.75	63
MLBF using FCFB	-5.88	0.83	56
MLBF using ILP	-5.89	0.43	85

Figure 5-9 shows the histogram of the Doppler ambiguity estimates by using different Doppler ambiguity resolvers. It illustrates the same results as shown in Table 5-2

in a more visible way. The height of the peak at the correct ambiguity number corresponds to the success rate, and the spread of the "bars" is related to the standard deviation of the estimates. The symmetry of the bar chart is very important to get the correct average (mean).

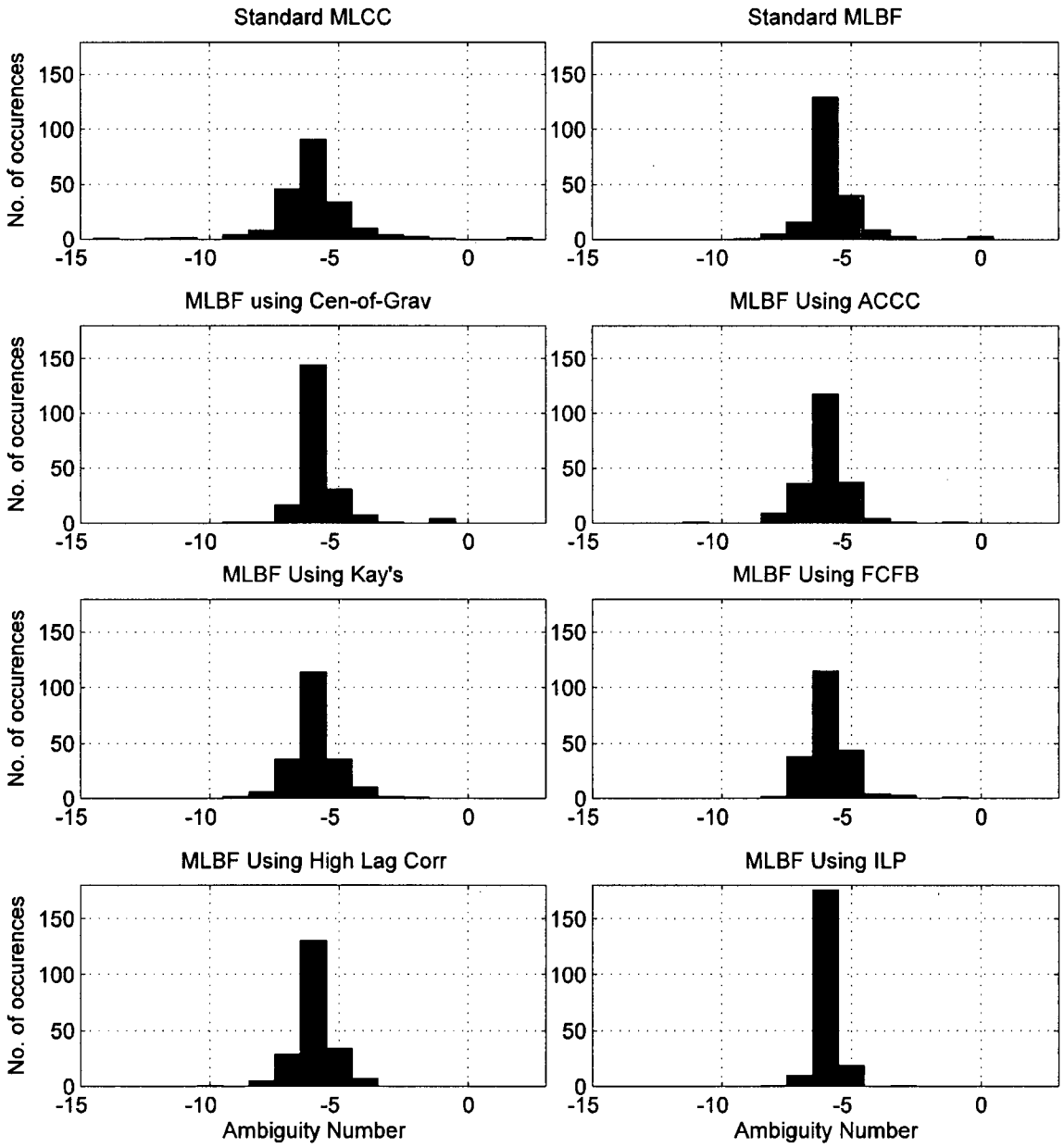

Figure 5-9 Histogram of the Doppler ambiguity estimates by DARs of the 207 selected blocks

It can be seen in Table 5-2 as well as in Figure 5-9 that the frequency estimators using the phase increments have lower standard deviation than the estimators using FFTs. It means that the frequency estimators show better performances than the existing frequency estimators in the MLBF algorithm. Especially, the ILP estimator has the best performance among all the estimators. It has the lowest standard deviation (less than half of the existing estimator) as well as the highest success rate (23% higher than the existing estimator). So, in implementation, we recommend to apply the ILP estimator in the beat frequency estimation in the MLBF algorithm.

5.5 Summary

In this chapter, we applied improved beat frequency estimation methods to the MLBF algorithm for the Doppler ambiguity resolution. As the existing MLBF algorithm uses the maximum *FFT* coefficient to measure the beat frequency, the estimate accuracy is limited by the quantization errors and RCM segmentation. As a survey result, several frequency estimators are introduced to avoid such quantization errors. We first analyzed and examined the estimator based on the center of gravity in the periodogram. Then, we introduced and compared five frequency estimators that are based on phase increments. To improve the beat frequency estimation, we applied the frequency estimators discussed with better accuracy in the MLBF algorithm. The experimental results on RADARSAT-1 real data show that the proposed method gives more consistent estimates than the existing MLBF algorithm. It can achieve correct Doppler ambiguity estimates in a higher percentage of the blocks and its estimation error is less than half that of the existing algorithm.

Chapter 6
Improved Slope Estimation for Doppler Ambiguity Resolution

The Look Misregistration algorithm proposed in 1986 [10] uses the fact that the average slope of the target trajectory before range cell migration correction (RCMC) is proportional to the beam squint angle and the Doppler centroid. Consequently, the Doppler centroid frequency can be estimated by measuring the slope of the target trajectory in range compressed image. Kong et al. have proposed to apply the Radon Transform in the slope estimation to estimate the Doppler centroid frequency of airborne SAR data in 2005 [35]. In this chapter, Kong's method is well explained and adapted for Doppler ambiguity resolution for satellite SAR data. In addition, a simpler method of combining RCMC and integration in slope estimation is presented. Through the experiments on real data, both the Radon method and the new method prove to have good performances in estimating the Doppler ambiguity number for satellite SAR data, not only in scenes with bright isolated targets, but also in the areas with low to medium contrast.

6.1 Geometry of a SAR Target Trajectory

As discussed in Chapter 2, the Doppler centroid can be derived from the geometry model of the SAR system; with an accurate knowledge of the system parameters such as the satellite attitude (see Appendix 12A of [15]). The geometry model of the SAR system is shown in Figure 6-1, where V_r the effective SAR is forward velocity, and $\theta_{r,c}$ is the beam squint angle measured in the slant range plane. If we know the parameter values, the total Doppler centroid $f_{\eta c}$ can be expressed as:

$$f_{\eta c} = \frac{2V_r}{\lambda_c} \sin\theta_{r,c} \tag{6.1}$$

where λ_c is the wavelength corresponding to the radar carrier frequency. However, as the attitude measurements are not accurate enough for precision processing, the Doppler centroid are usually estimated from the received data.

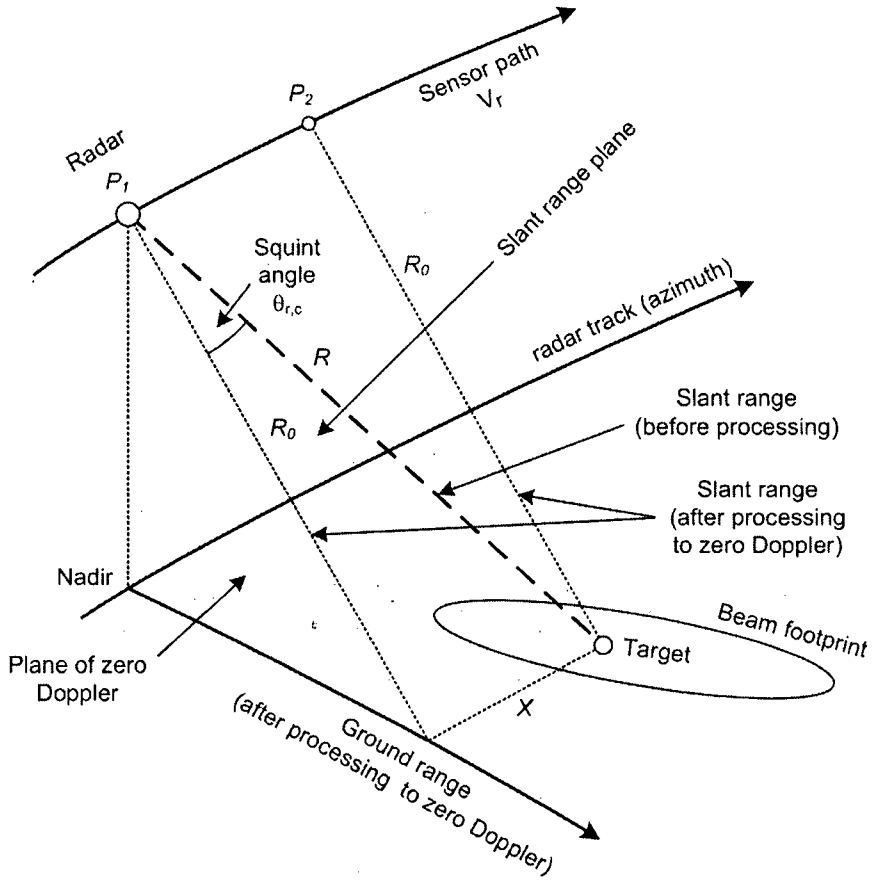

Figure 6-1 Geometry model of SAR data acquisition in the slant range plane [15]

A non-zero squint angle, $\theta_{r,c}$, leads to migrated targets trajectory in the slant range/azimuth plane. If this slope of the average migration can be measured, the squint angle and thereby the Doppler centroid can be estimated.

As a simple way to illustrate how to estimate the Doppler centroid from the slope measurement, the point target response after range compression is examined. Figure 6-2 shows a single target trajectory in the slant range/azimuth plane. It is seen that the signal

energy can be spread over several range cells during the exposure time. The variation of range with time is called Range Cell Migration (RCM). As the direction of the beam center line is perpendicular to the target trajectory at the middle of the target exposure, the squint angle, $\theta_{r,c}$, is equal to the angle of the linear component of RCM.

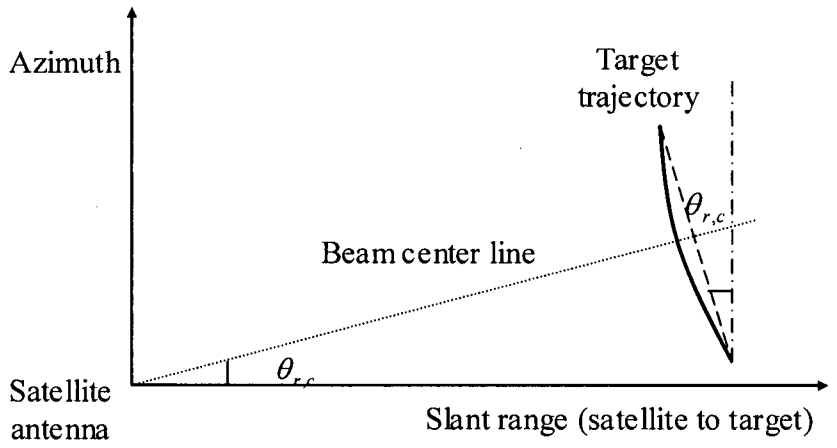

Figure 6-2 Range migration of a point target in range compressed domain

To illustrate variation of the slant range with time, the slant range equation is examined. We expand the equation of the slant range about the beam center crossing time η_c and ignore the higher order components. Then the range from the satellite to the target at certain azimuth time, $R(\eta)$, can be approximated by the parabola:

$$R(\eta) = R(\eta_c) - V_r \sin\theta_{r,c}\ (\eta - \eta_c) + \frac{1}{2}\frac{V_r^{\ 2}\cos^2\theta_{r,c}}{R(\eta_c)}(\eta - \eta_c)^2 \qquad (6.2)$$

From (6.2), we see that the average RCM slope can be expressed as - $V_r \sin\theta_{r,c}$, in units of *m/s*. If the slope is positive, that is, the range increases with azimuth time, the antenna has a "backward" or negative squint angle – the Doppler frequency is negative, as is typical of ascending orbits without yaw steering. On the other hand, a negative slope corresponds to a forward squint angle of the antenna.

Therefore, if the RCM slope is measured correctly, the absolute Doppler centroid can be derived directly from (6.1), with the knowledge of the radar wavelength, λ and satellite effective velocity, V_r. While there are more accurate ways of estimating the baseband Doppler centroid, the methods of measuring the RCM slope can provide a reliable estimate of the Doppler ambiguity number.

In this chapter, we introduce two Doppler ambiguity resolvers based on the RCM slope estimation. One is using the Radon Transform, and the other is using RCMC and azimuth integration.

6.2 Using the Radon Transform

The Radon Transform is a well-known method of detecting linear features in an image, such as the slope of lines [36] [37]. Kong et al. have applied the Radon Transform to estimate the Doppler centroid frequency of airborne SAR data in 2005 [35]. In this section, we explain Kong's method in more detail and apply it to the Doppler ambiguity estimation for satellite SAR data. In addition, a few improvements are proposed.

6.2.1 The Radon transform for linear feature detection

In order to extract the information of RCM slope from the range compressed image, certain image processing techniques can be applied. The Radon transform is an effective technique in extracting the parameters of linear features, such as their slope, even in the presence of noise [36] [37]. Because of its advantageous property in detecting lines with arbitrary orientation, the Radon transform has been successfully used in the SAR imagery processing, such as ship wake detection [38]. This transform integrates intensity along every possible direction in the image and maps this information into a feature space parameterized by the angle with respect to the positive y-axis, θ, and its distance from the origin, ρ.

The angle, θ, and the distance, ρ, form the coordinates in the transformed representation of a line. The concept is that a concentrated point in the transform space represents a linear feature in the image. This approach is particularly suited for noisy images, since the integration process tends to average out intensity fluctuations due to noise. The Radon transform equation for the image, $g(x, y)$, is defined as [36]:

$$\hat{g}(\rho,\theta) = \int_{-\infty}^{\infty}\int_{-\infty}^{\infty} g(x,y)\delta(\rho - x\cos\theta - y\sin\theta)dxdy \qquad (6.3)$$

where δ is the Dirac delta function and $\delta(\rho - x\cos\theta - y\sin\theta)$ directs the integration along the angle, θ. The range of θ is limited to $0 \leq \theta < \pi$.

To illustrate the relationship between the image coordinates, (x, y), and the transform parameters, (θ, ρ), a range compressed SAR magnitude image with three point targets is simulated in Figure 6-3 Panel (a). A significant linear RCM is assumed, and the quadratic RCM is negligible. The skew angle of the target trajectories is 30 degree, and the Radon transform is taken over angles from 28 to 32 degrees, in steps of 0.2 degrees. The transform result is shown in Panel (b), where only the central part of the ρ axis is displayed. When the integration in (6.3) is taken along the true direction of the lines, the energy is most concentrated along the ρ axis. It can be seen that there are three concentrated areas of energy in the vicinity of $\theta = 30^{o}$, which indicates the angle of the skewed lines in the image.

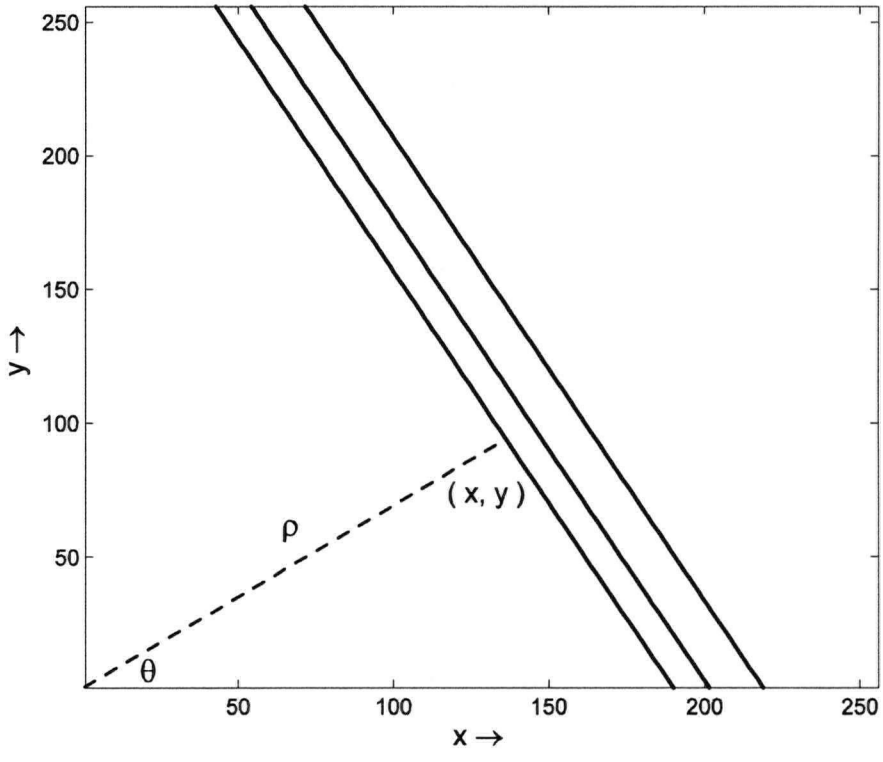

(a) Simulated SAR magnitude image

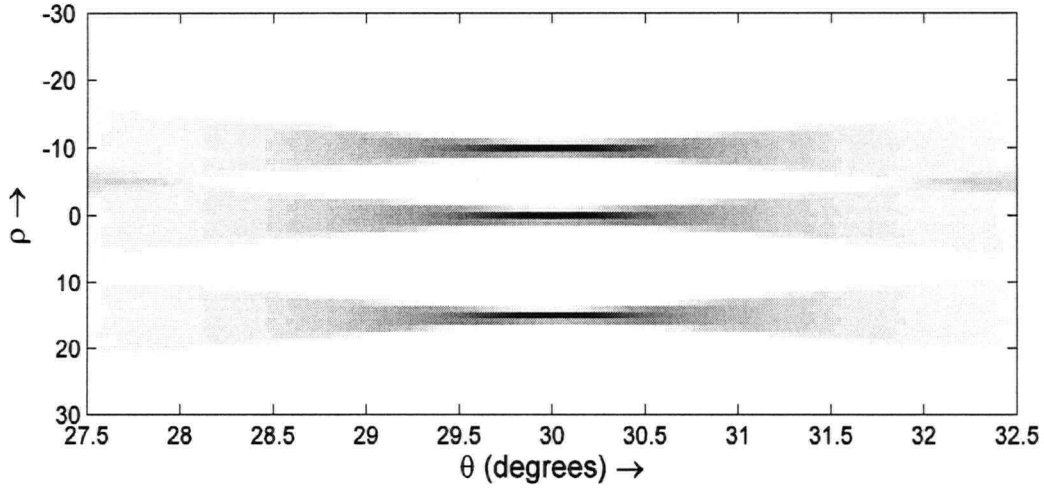

(b) Radon Transform of (a)

Figure 6-3 Simulated SAR magnitude image and its Radon transform

In order to investigate the results in more detail, we take vetical slices along the ρ axis of Figure 6-3 Panel (b) at several angles. Figure 6-4 shows those five slices from 26 degree to 32 degree. It can be seen that the Radon Tranform result is highly concentrated at the actual skew angleof the target trajectories and increasingly dispersed at other angles. In this way, the RCM slope in the range-compressed SAR image can be estimated by finding the skew angle, $\hat{\theta}$, that gives the maximum concentration of the Radon Transform energy along the ρ axis. A detection method of the Feature Space Line Detector (FSLD) was proposed in [37], which it was shown that the calculation of the variance of the slices along the ρ axis is a good measurement of the concentration.

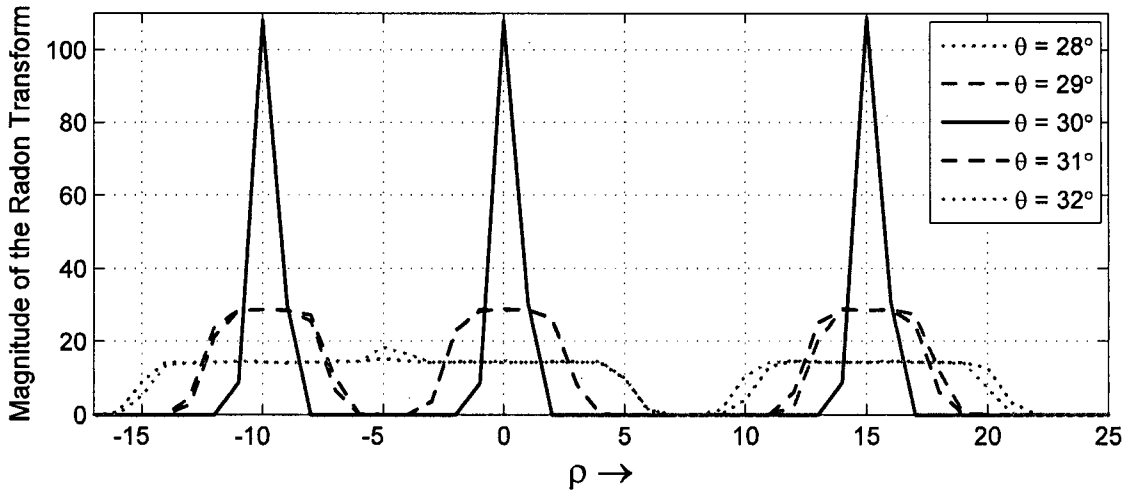

Figure 6-4 Vertical slices through Radon transform of Figure 6-3 Panel (b)

6.2.2 Applying the Radon transform to Doppler estimation

Due to its ability of detecting the linear features in an image, Kong et al. applied the Radon transform into Doppler centroid estimation of airborne SAR data in their geometry Doppler estimator (GDE) [35]. However, due to the lack of bright isolated targets in most real SAR data, the measurements are usually not precise enough for the estimation of the baseband part of the Doppler centroid. Since there are several

algorithms that can obtain very accurate baseband Doppler estimates, we recommend that the estimator using the Radon transform only be used to obtain the Doppler ambiguity number. The detailed processing of this estimator can be stated as follows.

First, take the magnitude or power of the range compressed image and then calculate the Radon transform. As the Radon transform requires an amount of computing time, restrict the angles to within a small range around the expected value. For example, we can estimate the squint angle from the geometry model of the satellite SAR system, with the assumption of the maximum yaw/pitch angle deviations. Otherwise, if the range of angles is not easy to estimate *a priori*, the Radon transform can be applied first using coarse angle increments, and later with a reduced range of angles and finer angle increments as the estimates are refined. In the implementation, the Radon transform is calculated with discrete parameter steps, and the transformed image can be expressed as:

$$R(n,m) = \hat{g}(\rho_0 + n\Delta\rho, \theta_0 + m\Delta\theta), \quad 0 < n < N-1, \quad 0 < m < M-1 \qquad (6.4)$$

where n, m are the indexes of distance and angle, $\Delta\rho$ and $\Delta\theta$ are the step sizes of ρ and θ respectively, and ρ_0 and θ_0 are the starting values of the Radon Transform parameters.

In order to illustrate the principle of the estimator, we first examine it with a part of an image with bright targets. The "ships" scene of the RADARSAT-1 fine mode scene of Vancouver can provide a good example (see Figure 4-10). The ships in this image can be considered as isolated bright targets and appear as several near-linear trajectories in the range compressed image. The linear component of range migration is clearly seen. The quadratic term is relatively small – about half a range cell.

The Radon transform is applied to the range-compressed image of the "ships" scene, using angles, θ, from 1.4 *degree* to 2.0 *degree* with an increment of 0.02 *degree*. Similar to Figure 6-4, Figure 6-5 shows three vertical slices along ρ in the Radon transform of the "ships" scene at three different angles (for clarity, the horizontal axis of

the figure is expanded so that only one of the ships is shown). It can be seen that the curve at 1.72 degree is more concentrated than the curves at the other two angles. It was found that the concentration of the energy dispersed for angles away from 1.72 degree, so this 1.72 degree very close to the true squint angle.

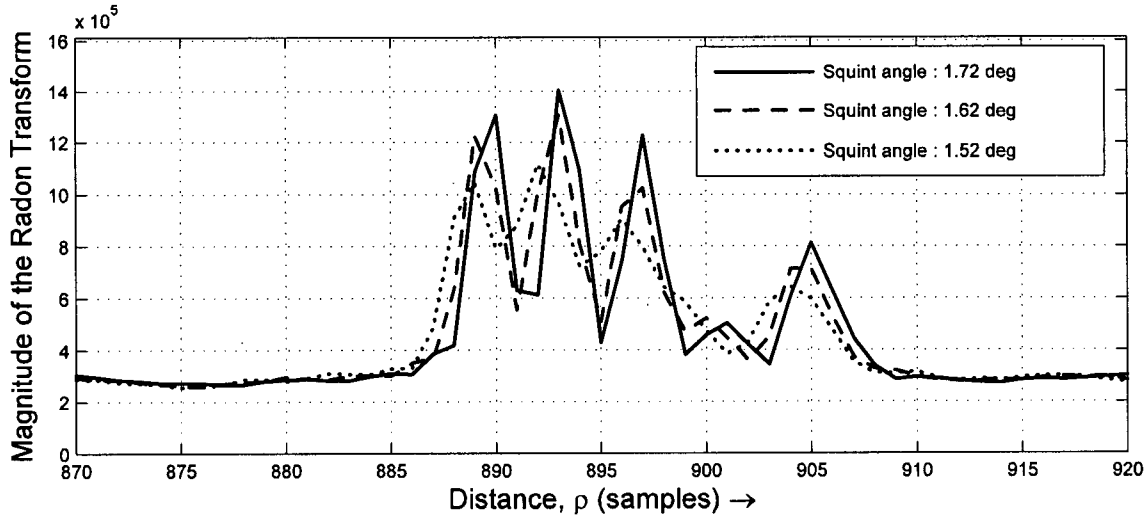

Figure 6-5 Slices taken from the Radon transform of the "ships" scene

To get better sensitivity, Kong et al. calculate the differential of the transform slices along ρ to emphasize the energy concentration [35]. Figure 6-6 shows the differential operation results of Figure 6-5 . It can be seen that the curve close to the true skew angle exhibits higher variance, while the curves away from the true skew angle have lower variance, as the energy in the integral is more dispersed. In both Figure 6-5 and Figure 6-6, the slices at 1.82 degree and 1.92 degree are similar to the slices taken at 1.62 degree and 1.52 degree.

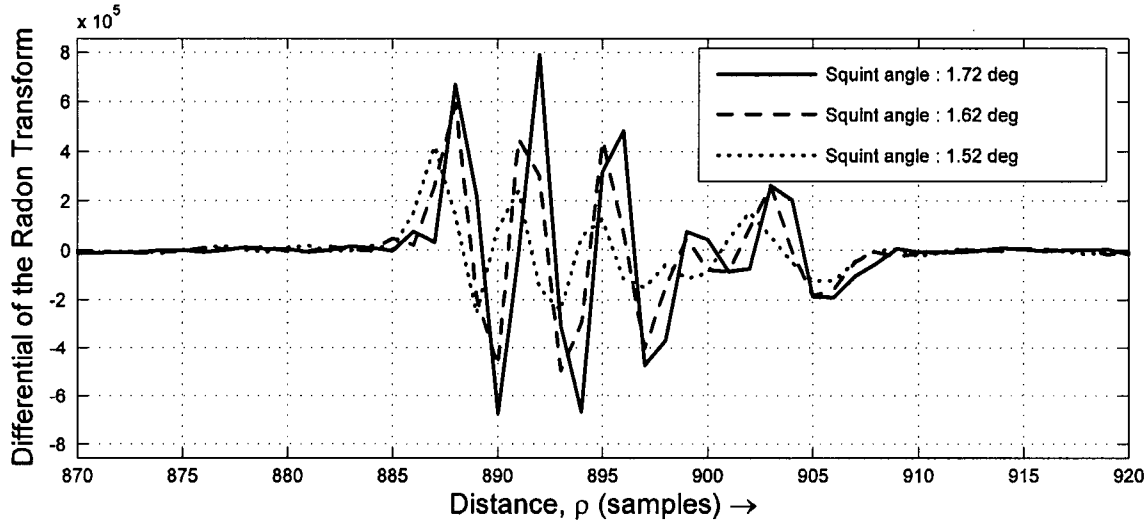

Figure 6-6 The differential of the slices in Figure 6-5

To quantify the variability of the differential curve of Figure 6-6, the variance of the differential is calculated over the ρ dimension, for each angle in the Radon transform. It was presented in [38] that the calculation equation at $\theta = \theta_0 + m\,\Delta\theta$ can be expressed as:

$$d(n,m) = R(n+1,m) - R(n,m) \tag{6.5}$$

$$Var(m) = \frac{1}{N-1}\sum_{n=0}^{N-2} d^2(n,m) - \left\{\frac{1}{N-1}\sum_{n=0}^{N-2} d(n,m)\right\}^2 \tag{6.6}$$

where n is the index of ρ, m is the index of θ, and $d(n,m)$ is the differential of the Radon transform, $R(n,m)$, along the ρ axis. The variance curve will have a peak at the angle where the concentration of energy is greatest.

6.2.3 Measuring the squint angle from the variance curve

As discussed in the previous Section 6.2.2, the squint angle can be estimated by measuring the location of the peak in the variance of differential curve along the ρ axis. However, in practice the presence of noise and clutter can distort the variance curve, as it is not a normal case that a SAR scene has isolated point targets. Rather than simply

finding the peak of the variance curve, a curve fitting approach can find the central angle more accurately.

Kong et al. have recommended using a Gaussian function with four unknown parameters to fit the variance curve and measure the peak location from the fitting parameters. The Gaussian function is defined as:

$$G(x) = A \exp\left(-\frac{(x-\mu)^2}{2\sigma^2}\right) + C \qquad (6.7)$$

where x is the independent angle variable, and the four unknown parameters are: the amplitude, A, the mean or peak location parameter μ, the standard deviation, σ, and the additive constant (pedestal), C.

In the definition, a certain Gaussian function can be fully expressed by the four parameters: A, μ, σ, and C. After finding a set of parameters that can form a Gaussian function with a closest shape to the actual curve, the peak location of the curve can be measured from the mean value μ. Figure 6-7 shows the curve fit procedure.

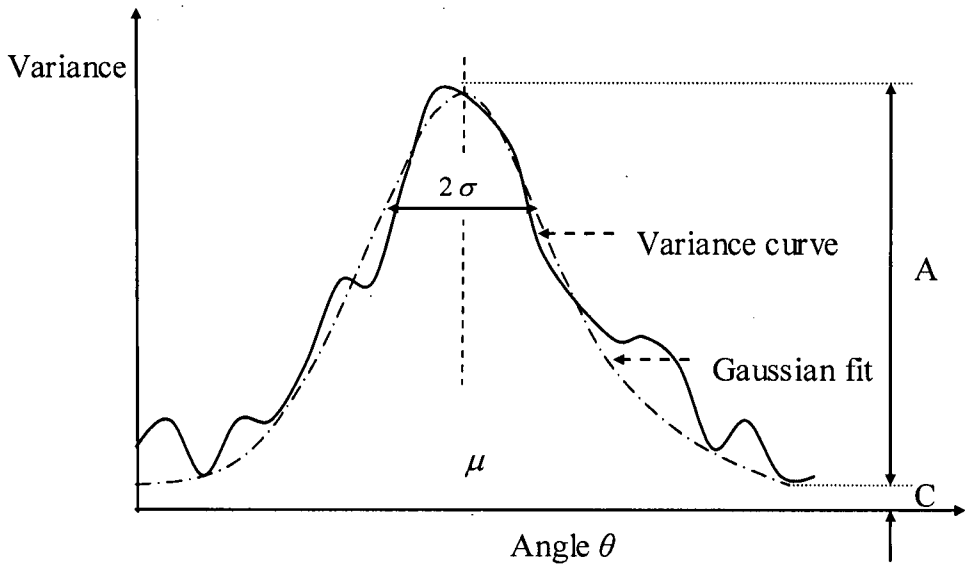

Figure 6-7 Fitting a Gaussian function to the variance curve

Gaussian fitting needs search procedure, which is time and computation consuming. To avoid the complexity of curve fitting, a simpler and almost as accurate method of finding the location of the peak of the variance curve is to fin the "center of gravity" of the curve. The center of gravity is the position that can balance the integral of its two sides, and can be calculated using:

$$\hat{\theta}_c = \frac{\sum_{m=1}^{M} \theta_m \cdot Var(m)}{\sum_{m=1}^{M} Var(m)} \tag{6.8}$$

where $\hat{\theta}_c$ is the estimated "center of gravity", and $Var(m)$ is the variance value at angle θ_m.

As illustrated in Figure 6-8, this method is equivalent to finding the angle $\hat{\theta}_c$, that makes the integral of the two shaded areas, $\mathbf{I}_1$ and $\mathbf{I}_2$ equal, when the integral is taken to the left and to the right of the estimated angle. When the variance curve is not symmetrical because of noise and clutter, the center of gravity is a more accurate estimate than simply the position of the maximum value.

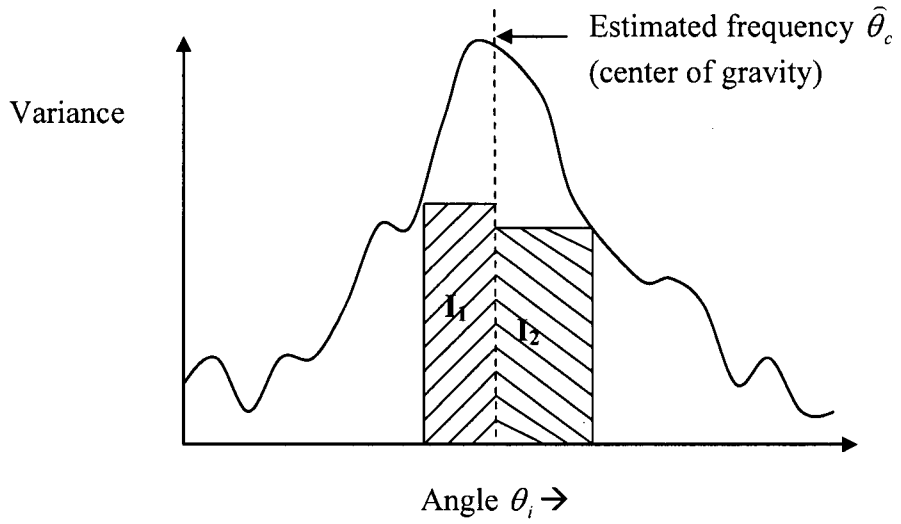

Figure 6-8 Finding the "peak" of the variance curve by the "center of gravity"

To test the performances of the two measurements, we implement them with the "ships" scene. In the implementation, we use MATLAB's `fminsearch` routine to find the four unknown parameters for the Gaussian fit. This routine uses the Nelder-Mead parameter search procedure [39]. Figure 6 -9 shows the measurement results of the Gaussian fit and center of gravity for the "ships" scene. Because the variance curve is quite symmetrical and the noise level is low in this high contrast case, the Gaussian fit curve is very close to the actual variance curve. The closeness of the fit curve shows that the Gaussian function is an appropriate fitting function for this SAR data. It is also shown in the figure that using Gaussian fit the measured squint angle is 1.726 degree, and using the center of gravity the measured squint angle is 1.731 degree. Both of the measurements are very close to the true squint angle of 1.720 degree. While the Gaussian fitting method obtains the best estimate in this case, the error of the center of gravity method is fairly small, well within the ambiguity error limit (the ambiguity error limit represents the range of angles that do not lead to a Doppler ambiguity error). In summary, the Gaussian fitting method can give the best squint angle measurement. The center of gravity method can be viewed as a simpler but still adequate way.

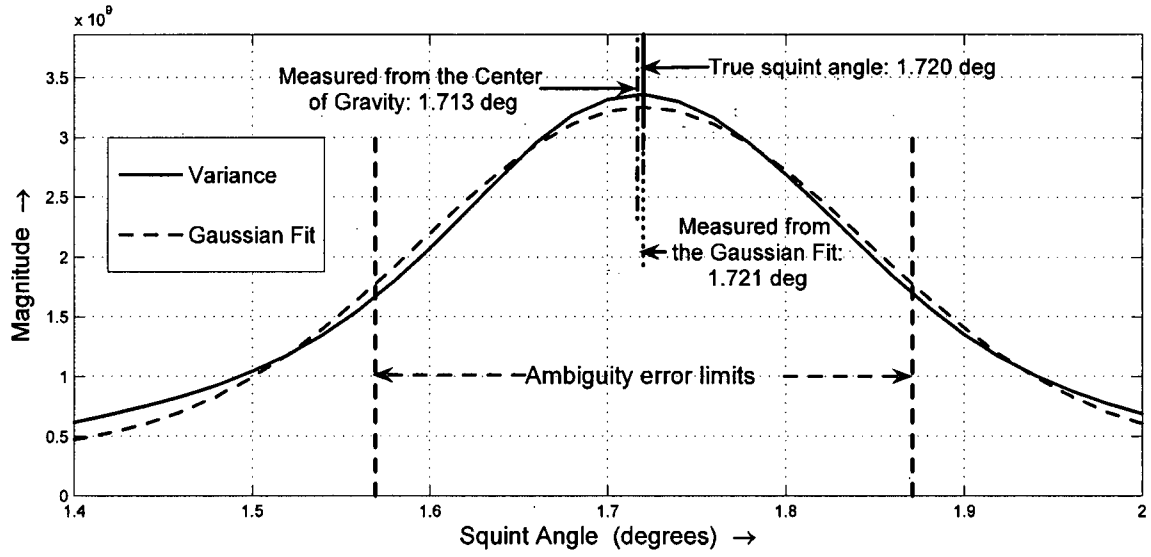

Figure 6-9 Estimating the squint angle from the variance curve ("ships" scene)

6.2.4 Resolving the Doppler ambiguity

However, the estimated squint angle is in the unit of range samples per azimuth sample and needs to be changed into unit of meters per second. So, the estimated angle is multiplied by $c/(2F_r)$ to change range samples into meters and by the PRF to change azimuth samples into seconds. After the adjustments, the result is measured in the same unit of the squint angle of the radar beam and the Doppler centroid can be calculated directly from (6.1).

As in other Doppler ambiguity resolvers, the baseband Doppler Centroid should be measured first using "spectral fit" or ACCC algorithm [15]. Then, the baseband Doppler centroid is subtracted from the estimated absolute Doppler frequency and the result is divided by the PRF. After this, the ambiguity estimate is obtained by a rounding operation. This reduces the ambiguity estimate to the more reliable estimate of an integer. The calculating procedure can be expressed as [15]:

$$M_{amb} = round\left(\frac{f_{\eta c} - f_{\eta c}'}{PRF}\right) \tag{6.9}$$

where $f_{\eta c}$ is the absolute Doppler frequency estimate from the Radon method, $f_{\eta c}'$ is the accurate baseband Doppler centroid estimate, and M_{amb} is the estimated ambiguity number.

6.2.5 Discussion

In this subsection, two SAR signal processing procedure are discussed that would provide some improvements to the Radon estimation method.

Removing Quadratic RCM

As shown in (2.6) of Chapter 2, the RCM is not a purely linear function and the quadratic components of RCM cannot be ignored in some SAR system. If the quadratic RCM is significant, the estimated slope will vary along the target trajectory and the peak

of the variance curve will be further dispersed, reducing the sensitivity of the estimator. Therefore, in order to adjust the RCM to a straight line, it is recommended to remove the quadratic part from the full RCM before applying the Radon Transform.

The quadratic RCM in meters in azimuth time domain can be expressed as:

$$\Delta R_{quad}(\eta) = \frac{V_r^{\,2} \cos^2 \theta_{r,c}}{2\, R(\eta_c)} (\eta - \eta_c)^2 \approx \frac{V_r^{\,2}}{2\, R(\eta_c)} (\eta - \eta_c)^2 \qquad (6.10)$$

where the approximation is used when the squint angle, $\theta_{r,c}$, is small enough and $\cos^2 \theta_{r,c}$ can be approximated by 1. The variable η_c is the beam center crossing time and $R(\eta_c)$ is the slant range at the time when the target is illuminated by the beam center.

Fortunately, for most C-Band satellite SAR systems, such as RADARSAT-1 and ENVISAT, the quadratic part of RCM is relatively small. For example, in the "ships" scene that is acquired by the F2 beam of RADARSAT-1, the maximum quadratic RCM is about one half a range cell. Hence, removing the quadratic RCM would not lead to a significant improvement in this case. But for L-band satellites data, the quadratic part of RCM could be as large as several cells, and removing this part will improve the estimator considerably. It is also worth noting that the quadratic component of RCM can only be efficiently removed in the azimuth frequency domain and that the Radon method can be adapted to operate in this domain.

Secondary Range Compression

Depending upon the radar system parameters and the squint angle, secondary range compression (SRC) may have to be applied to sharpen the focus in the range Doppler domain. As discussed in Chapter 6 of [15], without SRC the range-compressed image can be defocused in the azimuth frequency domain, even though it is well focused in the azimuth time domain. On the other hand, if SRC is applied with the range compression filter, the image is well focused in the azimuth frequency domain, but possibly defocused in the azimuth time domain.

Therefore, if we apply the Radon Transform into RCM slope detection in the azimuth time domain (as we do in the examples in this Chapter), SRC should be implemented after the estimator. Otherwise, if RCM slope is detected in the azimuth frequency domain, SRC should be implemented before the estimator.

6.2.6 Quality Criteria

In order to avoid the corruption of the bad estimates from the areas with very weak backscatter or low contrast, quality criteria are used to detect and remove bad estimates from the final estimate, when the "spatial diversity" approach [19] is applied. In addition to the common quality criteria of SNR and contrast used in [15], four other estimator quality criteria that are specific to the estimator using the Radon Transform are examined as following:

Gaussian fit flag

This flag is to indicate whether the Gaussian fit method can achieve a expected fitting curve. If the search for the four Gaussian fit parameters does not converge, the fit procedure fails and the MATLAB `'fminsearch'` routine will come out with an error flag (flag = 0). In addition, if the fit parameters are beyond a reasonable range, we also declare that the fit procedure fails and set the flag to zero. On the other hand, if the fit is deemed successful, the flag is set to one and the next three criteria are examined.

Fit distortion (Fit_std)

The Fit distortion is defined as the normalized standard deviation of the difference between the measured variance curve and the fitting Gaussian function. This quality parameter is used to measure how close the shape of the variance curve to the Gaussian function. If the fit distortion has a fairly small value, it means that the variance curve is well-shaped and most possibly can provide a good estimate. On the contrary, if the fit distortion has a relatively large value, it means that the variance curve is distorted considerably and may provide a bad estimate.

Peak to Pedestal Ratio (PPR)

In addition, the shape of the fitted Gaussian function can be used to measure how good the estimate is. The Peak to Pedestal Ratio is obtained from the Gaussian fitting parameters by $PPR = (A+C) / C$. This quality parameter is used to measure the relative height of the peak. The bigger the ratio, the more outstanding the peak, and consequently the better the estimate.

Width of Gaussian fit

The parameter of standard deviation, σ, of the Gaussian function gives the width of the Gaussian fit. It is used to measure the sharpness of the variance curve. As we assume that sharper variance curves indicate better the estimates, it is preferred that the width of Gaussian fit has a smaller value.

6.3 Using the RCMC and Integration

The Doppler ambiguity resolver using the Radon Transform is a reliable method to obtain Doppler ambiguity estimates. However, the Radon Transform requires large and complex computations. In this section, we propose a new Doppler ambiguity resolver using RCMC and integration, which is based on the similar principle as the algorithm using the Radon transform but only requires simple calculations. Similar to the algorithm using the Radon Transform, this estimator cannot provide accurate baseband Doppler centroid frequency, but has good performance in Doppler Ambiguity estimation.

6.3.1 RCMC and azimuth integration

As discussed in the Section 6.2.2, the slope of the target trajectories with residual Range Cell Migration (RCM) is proportional to the Doppler centroid. In the proposed algorithm, RCMC is used to change the slope of the targets trajectories, and the azimuth integration is used to measure straightness of the trajectories along azimuth.

The absolute Doppler centroid frequency consists of baseband Doppler centroid part and Doppler Ambiguity part, which can be expressed by:

$$f_{\eta c} = f_{\eta c}' + M_{amb}\ PRF \tag{6.11}$$

where $f_{\eta c}'$ is the baseband Doppler centroid frequency, M_{amb} is the ambiguity number.

In this algorithm, in order to resolve the correct Doppler ambiguity number, correct baseband Doppler centroid estimates, $f_{\eta c}'$, are required. The coarse baseband Doppler estimates can be obtained by baseband Doppler estimators, such as "spectral fit" and ACCC algorithms. Then, the baseband Doppler is found as a function of range over the whole scene and unwrapped over the PRF jumps. In addition, the possible range of the Doppler ambiguity number is estimated from the geometry model, with the assumption of the maximum satellite attitude variation. As a result, a set of candidate absolute Doppler centroid frequencies is obtained from (6.11) according to the Doppler ambiguity range.

After that, full RCMC (e.g., both the linear and quadratic parts) is applied over the whole range compressed image using the candidate Doppler centroid frequencies. For processing efficiency, RCMC is usually implemented in range time and azimuth frequency domain, which is also called the range Doppler domain. In our study, RCMC is performed by using an interpolator based on the *sinc* function in the range Doppler domain. The *sinc* kernel is truncated and weighted by Kaiser Window. This equation represents the target displacement as a function of azimuth frequency f_η and the amount of RCM to correct is given by the second term in (6.10)

$$RCM(f_\eta) = \frac{\lambda^2 R(\eta_c)\left(f_\eta - f_{\eta c}\right)^2}{8\,V_r^{\,2}} \tag{6.12}$$

where $f_{\eta c}$ is the absolute Doppler centroid used, λ is the signal wavelength, and V_r is the radar effective velocity.

If RCMC is applied with correct Doppler ambiguity number, the target trajectories should be sprightly parallel to the azimuth direction and the energy gets most concentrated in certain range cells. Otherwise, if RCMC is applied with Doppler

ambiguity errors, the target trajectories have residual migration over several range cells, and the energy is dispersed over those range cells. Therefore, the correct Doppler ambiguity can be estimated by finding the ambiguity number with which RCMC can fully remove the RCM and make the target trajectories exactly straight to the range direction.

Applying azimuth integration of the data magnitude or power is found to be an effective way to measure the straightness of the target trajectory after RCMC. This operation is similar to what we do in the Radon Transform when the skew angle is zero. If the target trajectories are fully straight to the range direction, the energy vs. range is most concentrated. On the other hand, if the target trajectories have skewed slope along azimuth, the energy vs. range is dispersed.

To test its performance, the RCMC with azimuth integration method is applied to the "ships" scene, the same as the one we used in Section 6.2.2. The results of the azimuth integration using several ambiguity numbers are shown in Figure 6-10. It can be seen that the result with the most concentrated energy is obtained when the correct ambiguity number, $M_{amb} = -6$ is used. The results are dispersed, when the ambiguity numbers are away from the correct number, - 6. The larger the errors, the more dispersed the energy.

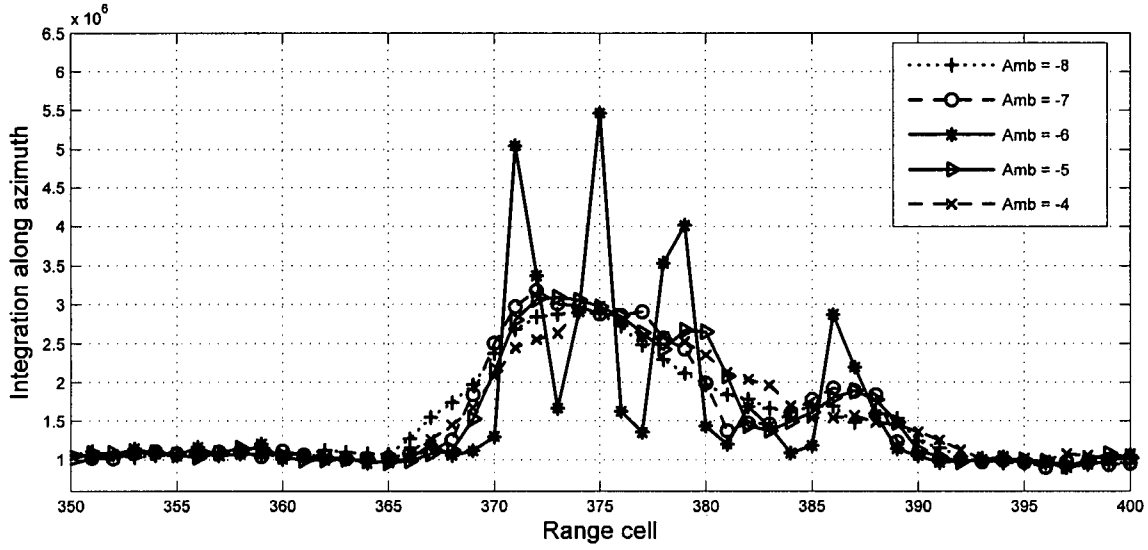

Figure 6-10 Azimuth integration of the "ships" scene after RCMC

6.3.2 Finding the Doppler ambiguity

As discussed in Section 6.2.2, the variance is a good parameter to measure the concentration of the curve. In this estimator, the variance of the integration curve vs. the Doppler Ambiguity number is calculated. The variance can be obtained by:

$$Var(m) = \frac{1}{N-1}\sum_{n=0}^{N-2} Int^2(n,m) - \left\{\frac{1}{N-1}\sum_{n=0}^{N-2} Int(n,m)\right\}^2 \qquad (6.13)$$

where m is the index of the Ambiguity number, n is the index of range cell, and $Int(n,m)$ is the azimuth integration at the specific range cell and ambiguity number.

The correct answer is even more apparent when the differential and variance are taken over the range variable. These results are plotted in Figure 6-11, which shows that the RCMC/integration results agree closely with the Radon transform results.

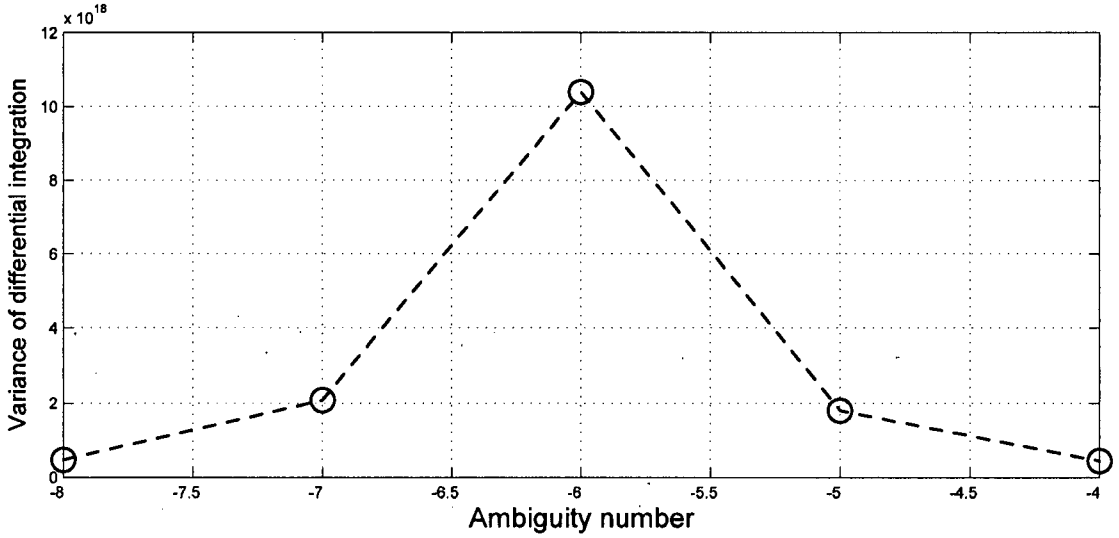

Figure 6-11 Variance curve in RCMC/Integration method

6.3.3 Discussion

Essentially, this method replaces the Radon transform with a simple integration of the image energy over one dimension (azimuth). Only one ambiguity number results in

RCMCed data that is aligned accurately in azimuth, and quality checks are an effective way of checking the accuracy of the alignment.

The baseband centroid estimates must be unwrapped so that a single ambiguity number applies over the whole scene. The spatial diversity, curve fitting method is the most reliable way of ensuring accurate estimates that vary smoothly over the scene, and the unwrapping is correct [19].

The RCMC is best applied in the azimuth frequency domain, as in the range Doppler algorithm, so that the quadratic RCMC can be performed efficiently. The subsequent estimation can be done in this domain, which is why SRC should be applied with the range compression filter (i.e., using Option 3 described in Chapter 6 of [15]).

6.3.4 Quality criteria

As in any ambiguity estimation method, parts of each scene will likely yield bad estimates. These usually occur in areas of low image SNR and/or low image contrast. Using the "spatial diversity" approach [19] over small blocks of the scene, quality criteria can be used to reject the bad blocks and obtain higher confidence in the answer. In addition to measuring the SNR and contrast of each block, the Peak to Pedestal Ration (PPR) is a suitable quality parameter.

As described in Section 6.2.4, the quality criteria are measured to remove the bad estimates. In this algorithm, we examine the quality measurements that are obtained from the shape of the variance curve. It can be found in the analysis that the sharper the curve of variance vs. Ambiguity number is, the more isolated targets are contained in the block and the more accurate estimate would be obtained. Therefore, we use the PMR and Normalized peak as the quality criteria.

Peak to Pedestal Ratio (PPR)

Similar to the quality measurement PMR described in Section 5.3.2, this measurement is used to measure the height of the peak compared to the non-peak values. The ratio is obtained by dividing the value of the peak point by the mean value of the other points.

6.4 Experiments on Real Satellite Data

As shown in the simulations and results of "ships" scene, the estimators using the Radon Transform and the RCMC/integration method have good performances in the area with isolated bright targets, since the targets have clearly-defined linear features after range compression. Kong has examined this estimator using the Radon Transform on three sets of airborne SAR data. In this section, we examine the performances of the estimators on general scenes of Satellite SAR data with different kinds of terrain. For comparison with other Doppler Ambiguity solvers, the RADARSAT-1 Vancouver scene is selected, as shown in Figure 4-10. In this experiment, the "spatial diversity" approach [19] is applied to obtain a single ambiguity number over the whole scene and the same block separation scheme is taken as what was done in Figure 4-17.

After range compression, the accurate "spectral fit" baseband Doppler estimator is applied and the PRF wraparound is removed. The quadratic component of RCM is removed. Then, the Radon and the RCMC/integration methods are applied to estimate the Doppler ambiguity. The quality criteria are measured for each block to test their effectiveness and to remove biased or noisy estimates

6.4.1 Analysis of typical results

Typical results are shown in Figure 6-12. This figure shows the results of the 12 blocks in the first row of the scene. The blocks run in the range direction of the scene, and are numbered from left to right, starting from the top of the figure. The horizontal axis refers to the angle used in the Radon transform, but is expressed in units of ambiguity

number for compatibility with the RCMC/integration method and for visibility of the result in ambiguity units. The baseband centroid is removed from the estimate, so the answer should be an integer. The correct answer is indicated by the vertical solid line and equals -6, and the vertical dashed lines indicate the ambiguity error limits (exceeding these limits results in an ambiguity error).

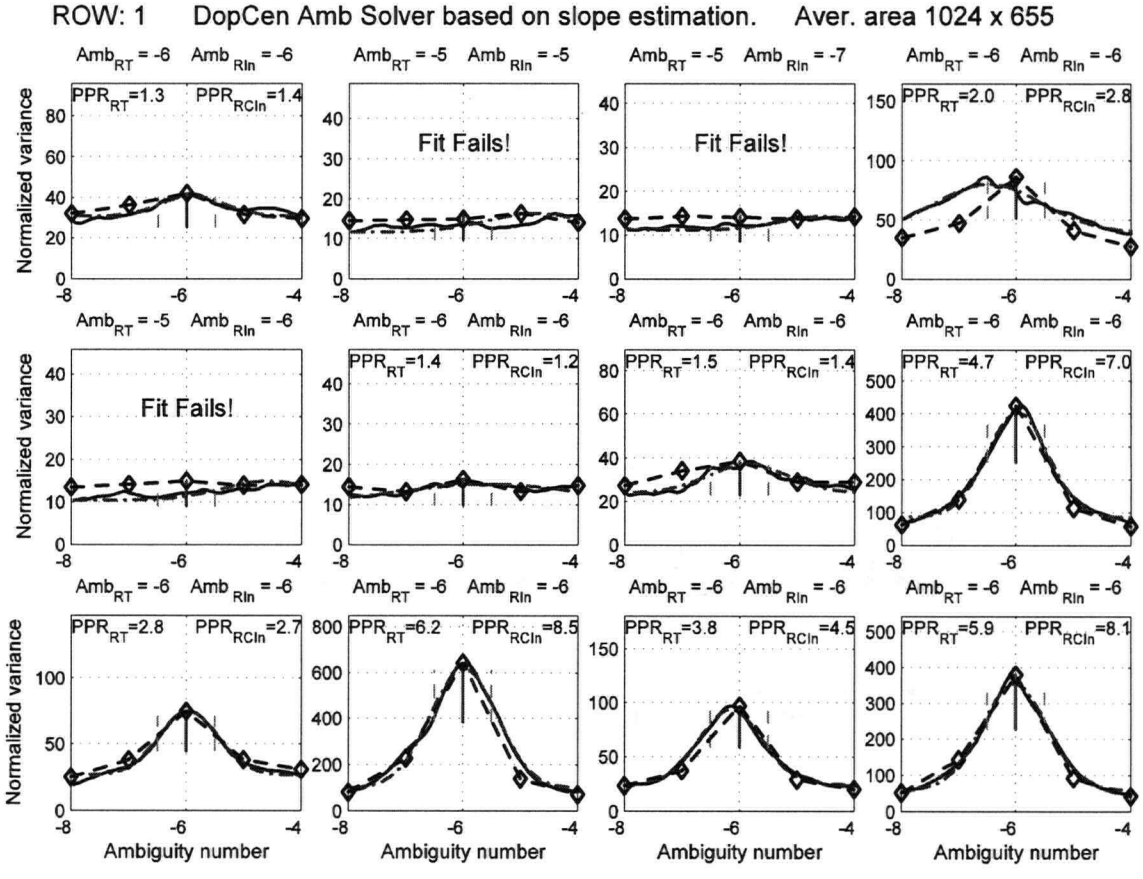

Figure 6-12 Finding the location of the peak of the variance curve by the Radon transform (Gaussian fit) method and by the RCMC/integration method -- Vancouver scene, Row 1

In each subfigure, the solid curve shows the variance of the difference of the Radon transform, referred to as the variance curve. Range compression is performed without SRC, and then the Radon transform is applied. The Gaussian fit to the Radon variance is indicated by the dash-dot line, and a quality criterion is expressed in the Peak-to-Pedestal ratio (PPR_{RT}). The other quality criteria discussed in Sections 6.2.6 are also

computed and checked, but are not shown on the plots for clarity reasons. The RCMC/integration results are shown by the diamonds and the connecting dashed line. This line is more quantized as it is only calculated at integer ambiguity numbers. Its Peak-to-Pedestal ratio (PPR_{RCin}) is also annotated to analogous to the PPR_{RT}. However, the two ratios are not totally comparable due to the quantization of the calculations. Finally, the estimated ambiguity values are given at the top of each subfigure for the Radon transform (left) and the RCMC/integration methods (right).

From Figure 6-12, it can be seen that the estimators can behave differently with different scene content, as referring to the bottom row of Figure 12.31 of [15]. Block 1 is half on land and half in the water. Even though the land is on a wooded island with few cultural features, there is enough contrast in the land to give the correct estimate with both methods, although the peak to pedestal ratios are quite low compared to other successful blocks. Similarly, Block 7 is mainly in the water, but has enough land area to give a good result. Blocks 2, 3, 5 and 6 are almost entirely in the water, with no bright targets and a low SNR because the water is not rough. The curves of variance vs. ambiguity number are dispersed, flat and random due to the lack of contrast. In three of these cases, the Radon variance curve does not have a well-defined peak and the Gaussian fit fails. In Block 5, the RCMC/integration method just barely gives the correct estimate. Both estimates are correct in Block 6, but the PPRs of both methods are low, which indicates a higher probability of error.

In comparison, Blocks 8 to 12 are in a suburban/agricultural/wooded area in northern Washington State, with relatively high contrast. The shapes of the variance curves are sharper, narrower, and closer to the Gaussian function and have a larger PPR than the other blocks. As a result, the angle estimates are well within the ambiguity error limits. Block 4 is also in the water, but contains the partial exposure of a single ship. The Radon variance curve and its Gaussian fit have a peak just outside the ambiguity error limit and give an incorrect result. However, the RCMC/integration method has a well-defined peak at $M_{amb} = -6$, and gives the correct result.

The quality criteria are found to reflect the effect of the scene content on the accuracy of the estimates when the block has fewer bright targets, less contrast or lower SNR, the Peak to Pedestal Ratio and the height of the variance curve are smaller. The estimates of the low-SNR Blocks 1-6 have a significant randomness and should be removed from the estimate average by the SNR, PPR or other quality criteria.

6.4.2 Assessments of quality criteria

In the Vancouver scene results, we find that the performance of the estimator is related to the scene content. Therefore, estimator quality criteria can be used to automate the assessment of scene content and the estimation results, to determine the suitability of each part of the scene for providing robust ambiguity estimates.

For the Radon transform method, we find that the Gaussian fitting flag is the most efficient quality criteria to remove most of the bad estimates. As shown in Table 6-1, for the whole 228 blocks, 204 block gave correct ambiguity estimates when the fit was deemed successful (flag = 1), while only 10 blocks gave wrong estimate when the flag = 1. When the fit was deemed unsuccessful (flag = 0), 9 blocks were indeed bad estimates, while 5 blocks actually had correct estimates. So, if the fitting flag = 1 were used as the only quality criterion to remove the possible bad estimates, the correct ambiguity would be obtained after an "averaging" or "majority vote" operation.

Table 6-1 Performance of the Gaussian fit flag as a quality measure

Quality Criteria	Number of blocks with Good estimate	Number of blocks with Bad estimate
Flag = 1	209	5
Flag = 0	2	12

In addition, we also assess the other quality criteria discussed in Section 6.2.6 in the rejection process in case the Gaussian fitting flag is not available. Table 6-2 shows the comparison of the performances of the SNR, fit width, fit standard deviation and PPR for the Radon transform method using Gaussian fit.

Table 6-2 Performance of the other quality measures for RT method

Quality Criteria	Number of blocks with Good estimate	Number of blocks with Bad estimate
SNR > - 4.3 dB	201	5
SNR < - 4.3 dB	10	12
Fit width < 0.52	196	5
Fit width > 0.52	15	12
Fit_std < 14.72	206	5
Fit_std > 14.72	5	12
PPR_RT > 1.35	202	5
PPR_RT < 1.35	9	12

Although the fit standard deviation shows the best performance among the quality criteria in the rejection process, the SNR and the PPR are the usually used in the implementation. These two ratios are convenient to calculate, and their performances are close to the optimal one. Moreover, they are applicable in the RCMC/Integration method. Table 6 -3 shows the performances of quality criteria SNR and PPR in the RCMC/ Integration method.

Table 6-3 Performance of the quality measures for RCMC/Integration method

Quality Criteria	Number of blocks with Good estimate	Number of blocks with Bad estimate
SNR > - 4.3 dB	202	4
SNR < - 4.3 dB	10	12
PPR_RCin > 1.25	203	4
PPR_RCin < 1.25	9	12

6.4.3 Comparison of the experiment results

In this section, we examine and compare the performance of the Radon and RCMC/integration estimators over a consistent set of blocks of the Vancouver scene. Results of the standard MLCC and MLBF algorithms are included as well for comparison. Each estimator has different quality measures, but in order to compare the estimators fairly, we only use only one quality criterion in this comparison so that the same blocks are rejected for each estimator. The quality criterion of "SNR > -1 dB" is used, and 28 out of the 228 blocks are rejected. These are mainly the blocks that are dominated by water areas.

Table 6-4 shows the comparison results of the performance of different estimators. The second and the third column give the mean value and standard deviation of the estimates before the rounding operation in the non-rejected blocks, while the final column gives the percentage of the blocks with the correct estimates after rounding operation of the non-rejected blocks. The first two rows assess the standard version of the MLCC and MLBF algorithms described in Chapter 3. The next two rows give the results of the iterative RCMC method and improved beat frequency estimation method described in Chapter 4 and Chapter 5. The last three rows assess the Radon transform method using

the center of gravity measurement, the Radon transform method with Gaussian fit, and finally the RCMC/integration method.

Table 6-4 Comparison of Doppler ambiguity resolvers for the Vancouver data

Doppler Ambiguity Resolvers	Mean (PRFs)	St. Dev. (PRFs)	Success rate (%)
Standard MLCC	-5.83	1.36	41
Standard MLBF	-5.72	1.09	62
MLBF using iterative RCMC	-5.92	0.73	92
MLBF using ILP	-5.89	0.43	85
Radon with Center of Gravity	-5.99	0.16	99
Radon with Gaussian fit	-5.98	0.14	99
RCMC with integration	-6.01	0.10	99

The mean values of results are all close enough to the correct number for all methods. However, the standard deviation is a more valuable assessment as it reveals the degree of randomness directly. It can be seen that the estimates based on the Radon transform and the RCMC/integration method are clearly giving estimates with less variability. The Gaussian fit method of estimating the slope gives better results than the center of gravity method, likely because it uses a more appropriate function in the fitting procedure. Finally, the RCMC/integration method give equal or better results than the Radon transform method, and may be the best one of all (note that the standard deviation value for the RCMC/integration method is somewhat affected by the integer-quantized solutions).

The histograms of the estimates of the different Doppler ambiguity resolvers reveal the same comparison results as described above, as shown in Figure 6-13.

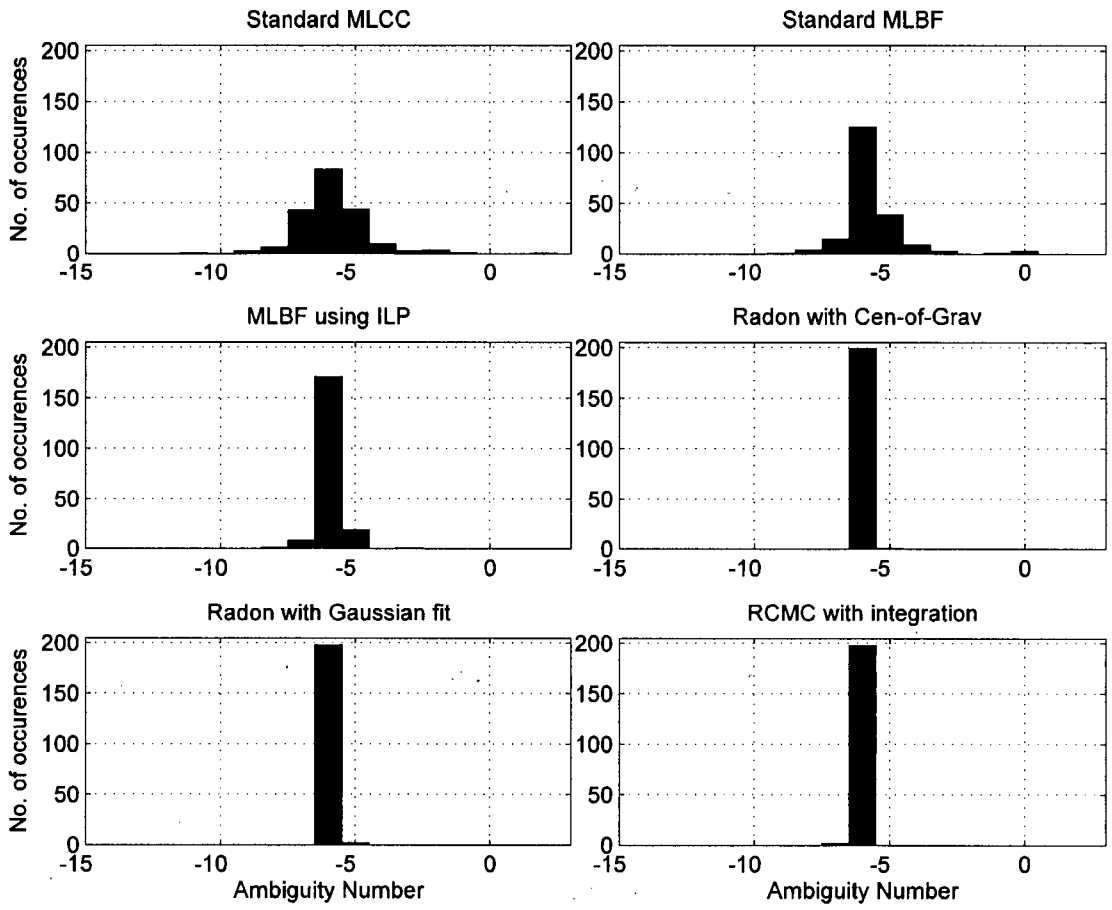

Figure 6-13 Histogram of Doppler ambiguity resolvers based on slope measurement

6.5 Summary

As the slope of target trajectories is proportional to the Doppler centroid, the estimate of the slope of linear features in a SAR image has proven to be an effective approach of resolving the Doppler ambiguity number. In this chapter, the Radon transform method proposed by Kong was evaluated with satellite SAR data, and some improvements are made. In addition, a new, simpler method based on RCMC and azimuth integration was presented.

Both the simulations and real data experiments show that the Doppler centroid estimators based on slope measurement are effective in resolving the Doppler ambiguity number. In the experiment using RADARSAT-1 data, the estimates can obtain an unbiased Doppler Ambiguity number and have a much smaller standard deviation than the current Doppler Ambiguity Estimators. It is shown that the slope estimation method work well in medium to high contrast scenes, even when no prominent targets are visible. The estimators gave correct result in almost all areas of the tested scene, except in calm water.

Chapter 7
Conclusions

7.1 Summary

This thesis has focused on Doppler centroid estimation problems and improvements to existing Doppler Ambiguity estimators for high-quality SAR processing. We have presented several improvements to the existing MLBF and slope-based estimation algorithms. In addition, experiments were conducted with the real satellite dataset, RADARSAT-1 Vancouver scene, in order to test the performances of the proposed methods.

Background to study

First, the Doppler centroid frequency and existing Doppler centroid estimation algorithms were introduced. The "spectral fit" and ACCC algorithms were chosen as reliable baseband Doppler estimators. The three phase-based Doppler ambiguity resolvers (the WDA algorithm, MLCC algorithm, and MLBF algorithm) were discussed. The WDA algorithm measures the slope of the centroid versus the transmission frequency directly in the range frequency domain. The MLCC algorithm uses two range looks to emulate two radars working in different transmission frequencies. The difference of the central frequencies of the two looks is measured by using the ACCC calculation, and the estimate of the absolute Doppler centroid is obtained. Like the MLCC algorithm, the MLBF algorithm takes advantage of the two range looks to estimate the Doppler centroid. These estimates can be obtained by beating the signals of the two looks and measuring the beat frequency from the generated beat signal. Because of their different measurement methods, the WDA and MLCC algorithm work well in low contrast scenes and can be biased by partially exposed strong targets. On the other hand, the MLBF algorithm

performs well in high contrast scenes and does not suffer as much from partially exposed bright targets as the other algorithms. In addition, the "spatial diversity" approach is used to provide a single ambiguity number over the whole frame of data. Areas of the scene that bias the estimates can be recognized using quality measures, and rejected from the estimation process. Then, a polynomial or geometry model can be used to fit a Doppler surface over the whole frame.

Principle of the MLBF algorithm

Since the MLBF algorithm proves to be one of the most reliable ways of estimating the Doppler centroid frequency of SAR signals, we mainly concentrated on this popular algorithm. We discussed a number of ways of improving its estimation sensitivity. First, we examined the principle of the MLBF algorithm in more detail, and gave a more thorough, frequency domain explanation of how it works. We showed how the phase of each range look depends on the range migration and how the phase varies in the range frequency domain. Based on this analysis, we highlighted the importance of extracting symmetrical range looks and shifting the range looks to baseband.

The benefits of applying RCMC

We also found that the RCMC has the effect of narrowing the bandwidth of the beat signal, and reducing the effect of cross beating when more than one significant target is present in one range cell. The noise in the beat signal due to cross beating is thereby reduced, allowing the FFT to obtain finer resolution because of the longer target exposure time in each range cell. Therefore, we considered using the RCMC to straighten the target trajectories before the beat frequency estimator is applied. We also demonstrated that the RCMC must be applied *after* the look extraction to preserve the phase variation, a point that was not obvious when the problem was first considered. If the RCMC is applied *before* the look extraction, the beat signal would have constant phase and the Doppler centroid could not be obtained from the measurement of the beat frequency. Based on the above analysis, we proposed an iterative scheme of applying the RCMC, since the ambiguity number is needed to be updated for correct RCMC.

Improved frequency estimator

The existing MLBF algorithm uses FFT operations to estimate the beat frequency by finding the maximum coefficient. This method has limitations of resolution and quantization, especially when the signal is discontinuous in one range cell due to range cell migration or burst mode operation. We thereby considered using more accurate frequency estimation methods based on phase increments and noise rejection filters to improve the beat frequency estimation. In this thesis, we examined five established frequency estimators, including Kay's estimator, the ACCC estimator, the FCFB estimator, the HLC estimator, and the ILP estimator. We discussed the processing procedures of all the estimators and the quality measurements of the phase coherence, which especially for the estimator using phase increments. Since the ILP estimator is the most accurate frequency estimator in the literature, we replaced the conventional FFT estimator with the ILP estimator to improve the beat frequency estimation. Although this method and the iterative RCMC algorithm can be combined, the majority of the estimation improvement can be obtained by using one of the modifications alone, as each method approaches the same sensitivity problem in a different fashion.

Improved slope estimation algorithm

We also examined and improved the methods that estimate the Doppler centroid by measuring the alignment of linear features in SAR data. These methods are based on the same principle as the "look misregistration" algorithm. The slope estimation methods take advantage of the fact that Range Migration is caused by the beam squint angle and its slope is proportional to the Doppler centroid. Kong has proposed a method that uses the Radon transform to measure the slope of the target energy and obtain the absolute Doppler centroid for the airborne SAR data. In our study, we discussed the properties and application of the Radon transform in more detail, and examined Kong's method in the Doppler ambiguity resolution for satellite SAR data. We developed an alternative and computationally simpler method that uses RCMC with azimuth integration in Doppler ambiguity resolution. This method employs the RCMC to change the slope of targets trajectories, and uses azimuth integration to find which Doppler ambiguity number makes the trajectories vertical. Several quality measurements of the "spatial diversity" approach

derived from the data and from each particular estimator were used to increase the robustness of the algorithm.

Experiments with RADARSAT data

The experiments with RADARSAT-1 data showed that the improved method yields more consistent estimates than does the existing algorithms. The proposed iterative RCMC method can increase the percentage of blocks yielding the correct ambiguity number from 62 to 92%. The method using the ILP estimator can obtain a standard deviation less than half that obtained by the existing method, and a much higher percentage of blocks that yield the correct ambiguity number. In addition, the slope estimation methods work well in medium to high contrast scenes, even when no prominent targets are visible. They can significantly increase the percentage of blocks yielding the correct ambiguity number. The improved estimators work best with the high contrast scenes, but work surprisingly well in medium to low contrast scenes.

7.2 Contributions

This thesis has presented several improved techniques for estimating the Doppler centroid in satellite SAR data. Particularly, we have:

- proposed a method that applies the RCMC after look extraction to reduce cross-beating and narrow the bandwidth of the beat signal, thereby improving the estimate results of the MLBF algorithm;
- proposed a method that uses more accurate frequency estimators based on phase increments to improve estimation of the beat frequency, which thereby improves the performance of the existing MLBF algorithm;
- applied the method using the Radon transform in the Doppler ambiguity resolution for satellite SAR data, and proposed some minor improvements to this method;

- proposed a simpler slope measurement method for Doppler ambiguity resolution using RCMC and azimuth integration, which has the same or even better performance than Kong's method; and
- developed several quality measurements for the proposed methods and implemented them in the "spatial selected" approach.

7.3 Future Work

The results of our research suggest the following topics for future investigation:

- The improved MLBF algorithms and the improved slope estimation algorithms can be combined together to further increase the sensitivity of estimate results.
- Better quality measurements need to be developed to remove more bad estimates and increase the robustness of the Doppler ambiguity resolvers.
- More real datasets with different contents should be used to test the performance of the proposed algorithms, such as ENVISAT data.
- The proposed algorithms should be applied to ScanSAR data to test their performance with burst mode datasets.

Bibliography

[1] J. J. Kovaly, "Synthetic Aperture Radar," *Artech House*, Dedham, MA, 1976.

[2] I. G. Cumming and J. R. Bennett, "Digital Processing of SEASAR SAR Data," in *Rec. IEEE International Conference on Acoustics, Speech and Signal Processing*, pp. 710-718, Aprirl 1979.

[3] C. Wu, K. Y. Liu, and M. J. Jin, "A Modeling and Correlation Algorithm for Spaceborne SAR Signals," *IEEE Trans. on Aerospace and Electronic Systems*, Vol. 18, Issue 5, pp. 563-574, September 1982.

[4] R. K. Raney, H. Runge, R. Bamler, I. G. Cumming, and F. H. Wong, "Precision SAR Processing Using Chirp Scaling," *IEEE Trans. Geoscience and Remote Sensing*, Vol. 32, Issue 4, pp. 786-799, July 1994.

[5] A. A. Thompson, J. C. Curlander, N. S. Mclagan, T. E. Feather, M. D'Iorio, and J. Lam, "ScanSAR Processing Using the Fast Scan System," in *Proceedings of the International Geoscience and Remote Sensing Symp., IGARSS'94*, Vol. 2, pp. 1187-1189, August 1994.

[6] H. Hellsten and L. E. Anderson, "An Inverse Method for the Processing of Synthetic Aperture Radar Data," *Inverse Problems*, Vol. 3, Issue 1, pp. 111-124, February 1987.

[7] F. K. Li, D. H. Held, J. C. Curlander, and C. Wu, "Doppler Parameter Estimation for Spaceborne Synthetic Aperture Radars," *IEEE Trans. Geoscience and Remote Sensing*, Vol. 23, Issue 1, pp. 47-56, January 1985.

[8] S. N. Madsen, "Estimating the Doppler Centroid of SAR Data," *IEEE Trans. Aerospace Electronic system,* Vol. 25, Issue 2, pp. 134-140, March 1989.

[9] R. Bamler, "Doppler Fequency Estimation and Cramer-Rao Bound," *IEEE Trans. Geoscience and Remote Sensing*, Vol. 29, Issue 3, pp. 385-390, May 1991.

[10] I. G. Cumming, P. F. Kavanagh, and M. R. Ito, "Resolving the Doppler Ambiguity for Spaceborne Synthetic Aperture Radar," in *Proceedings of the*

International Geoscience and Remote Sensing Symposium, IGARSS'86, pp. 1639-1643, September 1986.

[11] C. Y. Chang and J. C. Curlander, "Application of the Multiple PRF Technique to Resolve Doppler Centroid Estimation Ambiguity for Spaceborne SAR," *IEEE Trans. Geoscience and Remote Sensing*, Vol. 30, pp. 941-949, September 1992.

[12] R. Bamler and H. Runge, "PRF-ambiguity Resolving by Wavelength Diversity," *IEEE Trans. Geoscience and Remote Sensing*, Vol. 29, pp. 997-1003, November 1991.

[13] F. H. Wong and I. G. Cumming, "A Combined SAR Doppler Centroid Estimation Scheme Based upon Signal Phase," *IEEE Trans. on Geoscience and Remote Sensing*, Vol. 34, pp. 696-707, May 1996.

[14] J. Curlander and R. McDonough, "Synthetic Aperture Radar: Systems and Signal Processing," *John Wiley & Sons, New York*, November 1991.

[15] I. G. Cumming and F. H. Wong, "Digital Processing of Synthetic Aperture Radar Data Algorithms and Implementation," *Artech House, Norwood, MA*, January 2005.

[16] Tonghua Zhang, "Investigation of Biases in Doppler Centroid Estimation Algorithms," *Master's thesis, Dept. of Electrical and Computer Engineering, The University of British Columbia*, August 1999.

[17] R. K. Hawkins, T. I. Lukowski, K. P. Murnaghan, and S. K. Srivastava, "The Effects of Doppler Processing Errors in SAR Data," in *Proceedings of the CEOS SAR Calibration Workshop*, pp. 201-208, February 1998.

[18] I. G. Cumming, "Model-Based Doppler Estimation for Frame-Based SAR Processing," in *Proceedings of International Geoscience and Remote Sensing Symp., IGARSS'01*, Vol. 6, pp. 2645-2647, July 2001.

[19] I. G. Cumming. "A Spatially Selective Approach to Doppler Estimation for Frame-Based Satellite SAR Processing," *IEEE Trans. on Geoscience and Remote Sensing*, Vol. 42, Issue 6, pp. 1135-1148, June 2004.

[20] Stability and Controllability, Flight Training Handbook, AvStop Magazine online from: http://avstop.com/AC/FlightTraingHandbook/Stability.html

[21] M. Y. Jin, "Optimal Doppler Centroid Estimation for SAR Data From A Quasi-homogeneous Source," *IEEE Trans. Geoscience and Remote Sensing*, Vol. GE-24, pp. 1022-1025, March 1986.

[22] C. Cafforio, P. Guccione, and A. Monti Guarnieri, "Doppler Centroid Estimation for ScanSAR Data," *IEEE Trans. on Geoscience and Remote Sensing*, Vol. 42, Issue 1, pp. 14-23, January 2004.

[23] M. V. Dragosevic and B. Plache, "Doppler Tracker for A Spaceborne ScanSAR System," *IEEE Trans. Aerospace Electroic. Syst*em, Vol. 36, pp. 907–924, July 2000.

[24] E. O. Brigham, "The Fast Fourier Transform: An Introduction to Its Theory and Application," *Prentice Hall, Upper Saddle River, NJ*, November 1973.

[25] Discussions with Dr. Ian Cumming, March 2005.

[26] Personal communication with Dr. Frank Wong and Dr. Ian Cumming, May 2005.

[27] D. Rife and R. Boorstyn, "Single-tone Parameter Estimation from Discrete-time Observations," *IEEE Trans. Inform. Theory*, Vol. IT-20, pp.591–598, September 1974.

[28] S. Kay, "Modern Spectral Estimation: Theory and Application," *Englewood Cliffs. NJ: Prentice-Hall*, 1988.

[29] A. Herment, G. Demoment. P. Dumee, J. P. Guglielmi, and A. Delouche, "A New Adaptive Mean Frequency Estiamtor: Application to Constant Variance Color Flow Mapping," *IEEE Trans. on Ultrasonics, Ferroeletrics, and Frequency Control*, Vol. 40, Issue 6, pp. 796-804 , November 1993.

[30] S. Kay, "A Fast and Accurate Single Frequency Estimator," *IEEE Trans. Acoustic., Speech, Signal Processing*, Vol. 37, pp. 1987–1990. December 1989.

[31] M. Fowler and J. Johnson, "Extending the Threshold and Frequency Range for Phase-based Frequency Estimation," *IEEE Trans. Signal Processing*, Vol. 47, pp. 2857–2863, October 1999.

[32] M. P. Fitz, "Further Results in the Fast Estimation of A Single Frequency," *IEEE Trans. on Communication*, Vol. 42, Part 2. pp. 862-864, February-April 1994.

[33] T. Brown and M. M. Wang, "An Iterative Algorithm for Single-frequency Estimation," *IEEE Trans. Signal Processing*, Vol. 50, No. 11, pp. 2671–2682, November 2002.

[34] S. Li and I. G. Cumming, "Improved Beat Frequency Estimation in the MLBF Doppler Ambiguity Resolver," in *IEEE Proceedings of International Geoscience and Remote Sensing Symp., IGARSS'05*, Vol. 5, pp. 3348-3351, July 2005.

[35] Y.-K. Kong, B.-L. Cho, and Y.-S. Kim, "Ambiguity-Free Doppler Centroid Estimation Technique for Airborne SAR Using the Radon Transform," *IEEE Trans. Geoscience and Remote Sensing*, Vol. 43, Issue 4, pp. 715-721, April 2005.

[36] P. Toft, "The Radon Transform - Theory and Implementation," *PhD Thesis, Informatics and Mathematical Modeling, Technical University of Demark*, 1996

[37] A. L. Warrick and P. A. Delaney, "Detection of Linear Features Using a Localized Radon Transform," in *Conference Record of the Thirtieth Asilomar Conference on Signals, Systems and Computers*, Vol. 2, pp. 1245 - 1249, November 1996.

[38] A. C. Copeland, G. Ravichandran, and M. M. Trivedi, "Localized Radon Transform-based Detection of Ship Wakes in SAR Images," *IEEE Trans. on Geoscience and Remote Sensing*, Vol. 33, pp. 35-45, January 1995.

[39] J. A. Nelder and R. Mead, "A Simplex Method for Function Minimization," *Computer Journal*, Vol. 7, pp. 308-313, 1965. *Available in MATLAB as the function FMINSEARCH.*